MINISTÉRIO DA CIÊNCIA, TECNOLOGIA, INOVAÇÕES E COMUNICAÇÕES
INSTITUTO NACIONAL DE PESQUISAS ESPACIAIS

sid.inpe.br/mtc-m21b/2017/07.07.18.24-TDI

EVOLUTION OF ACTIVE REGIONS BASED ON SOLAR-SURFACE MAGNETIC FLUX OBSERVATIONS AND CORONAL MAGNETIC FIELDS EXTRAPOLATIONS: A CASE-STUDY OF NOAA 12443

André Chicrala Amaral Silva

Master's Dissertation of the Graduate Course in Space Geophysics, guided by Drs. Renato Sergio Dallaqua, and Judit Palacios Hernández, approved in August 07, 2017.

URL of the original document:
<http://urlib.net/8JMKD3MGP3W34P/3P8G8MB>

INPE
São José dos Campos
2017

PUBLISHED BY:

Instituto Nacional de Pesquisas Espaciais - INPE
Gabinete do Diretor (GB)
Serviço de Informação e Documentação (SID)
Caixa Postal 515 - CEP 12.245-970
São José dos Campos - SP - Brasil
Tel.:(012) 3208-6923/6921
E-mail: pubtc@inpe.br

MINISTÉRIO DA CIÊNCIA, TECNOLOGIA, INOVAÇÕES E COMUNICAÇÕES
INSTITUTO NACIONAL DE PESQUISAS ESPACIAIS

sid.inpe.br/mtc-m21b/2017/07.07.18.24-TDI

EVOLUTION OF ACTIVE REGIONS BASED ON SOLAR-SURFACE MAGNETIC FLUX OBSERVATIONS AND CORONAL MAGNETIC FIELDS EXTRAPOLATIONS: A CASE-STUDY OF NOAA 12443

André Chicrala Amaral Silva

Master's Dissertation of the Graduate Course in Space Geophysics, guided by Drs. Renato Sergio Dallaqua, and Judit Palacios Hernández, approved in August 07, 2017.

URL of the original document:
<http://urlib.net/8JMKD3MGP3W34P/3P8G8MB>

INPE
São José dos Campos
2017

Cataloging in Publication Data

Silva, André Chicrala Amaral.

Si38e Evolution of active regions based on solar-surface magnetic flux observations and coronal magnetic fields extrapolations: A case-study of NOAA 12443 / André Chicrala Amaral Silva. – São José dos Campos : INPE, 2017.

xx + 92 p. ; (sid.inpe.br/mtc-m21b/2017/07.07.18.24-TDI)

Dissertation (Master in Space Geophysics) – Instituto Nacional de Pesquisas Espaciais, São José dos Campos, 2017.

Guiding : Drs. Renato Sergio Dallaqua, and Judit Palacios Hernández.

1. Solar atmosphere. 2. Active regions. 3. Solar magnetism. 4. Spectropolarimetry. 5. Solar physics. I.Title.

CDU 523.9

Aluno (a): *André Chicrala Amaral Silva*

Título: "EVOLUTION OF ACTIVE REGIONS BASED ON SOLAR-SURFACE MAGNETIC FLUX OBSERVATIONS AND CORONAL MAGNETIC FIELDS EXTRAPOLATIONS: A CASE-STUDY OF NOAA 12443"

Aprovado (a) pela Banca Examinadora em cumprimento ao requisito exigido para obtenção do Título de ***Mestre*** em

Geofísica Espacial/Ciências do Ambiente Solar-Terrestre

Dr. Cristiano Max Wrasse

Presidente / INPE / São José dos Campos - SP

Dr. Renato Sergio Dallaqua

Orientador(a) / INPE / São José dos Campos - SP

Dra. Judit Palacios Hernández

Orientador(a) / UAH / Espanha - ES

Dr. Joaquim Eduardo Rezende Costa

Membro da Banca / INPE / São José dos Campos - SP

Dr. Jean-Pierre Raulin

Convidado(a) / CRAAM/Mackenzie / São Paulo - SP

Este trabalho foi aprovado por:

( ) maioria simples

( ) unanimidade

São José dos Campos, 07 de agosto de 2017

ACKNOWLEDGEMENTS

I would like to express my sincere gratitude to Dr. Luis Vieira, Dr. Renato Dalaqua, Dr. Judit Palacios, Dr. Jenny Marcela, Rodriguez Gomez, Dr. Barbara Thompson and Tardelli Stekel for all the time and patience that they are investing in my studies. Also, I would like to thank CAPES which sponsor my scholarship.

ABSTRACT

The solar surface is often populated by Active Regions (ARs) that are known for their intense magnetic field when compared to the solar quiet regions. During their evolution the ARs may give rise to energetic events such as flares or Coronal Mass Ejections (CMEs). In this work, data collected from the instruments Helioseismic and Magnetic Imager (HMI) and Hinode were used to measure the magnetic field in the Photosphere, using Stokes profiles, and to extrapolate those magnetic field vectors to the layers above: Chromosphere and Corona whose magnetic field cannot be directly measured with the available equipment and techniques. Since the behaviour of a plasma is strongly dependent on the magnetic field the results were applied to study the behaviour of the active region NOAA 12443. The results include maps of the Stokes parameters measured over NOAA 12443, the velocity fields along the Line Of Sight, a study of the behaviour of the currents and helicity of the region, the energy evolution of NOAA 12443 using a linear force free approach and a scenario studying some of the possible causes of the flaring activity and if this flare was an sympathetic event.

Palavras-chave: Solar Atmosphere. Active Regions. Solar magnetism. Spectropolarimetry. Solar physics.

EVOLUÇÃO DE REGIÕES ATIVAS BASEADO EM OBSERVAÇÕES DE FLUXO MAGNÉTICO NA SUPERFÍCIE SOLAR E EXTRAPOLAÇÕES DO CAMPO MAGNÉTICO CORONAL: UM ESTUDO DE CASO DA NOAA 12443

RESUMO

A superfície solar é comumente populada por Regiões Ativas (ARs) que são conhecidas por seu intenso campo magnético quando comparadas com as regiões de Sol quieto. Durente sua evolução, as ARs podem dar origem a eventos energéticos como flares ou ejeções coronais de massa (CMEs).Nesse trabalho, dados coletados dos instrumentos Helioseismic and Magnetic Imager (HMI) e Hinode forão usados para medir o campo magnético na fotosfera, usando os perfis de Stokes, e para extrapolar essas medidas de vetor campo magnético para as camadas acima: a Chromosfera e a Coroa onde esses campos magnéticos não podem ser diretamente medidos com as técnicas e aparatos disponíveis para este estudo. Como o comportamento de um plasma é fortemente dependente do campo magnético esses resultados forão aplicados para estudar o comportamento da região ativa NOAA 12443. Os resultados incluem mapas dos parâmetros de Stokes da região NOAA 12443, os campos de velocidade ao longo da linha de visada, um estudo do comportamento de correntes e helicidade da região, um estudo da evolução energética da NOAA 12443 usando uma abordagem linear livre de forças e um cenário que estuda algumas das possíveis causas da atividade de flare e se o flare em questão foi um evento simpático.

Palavras-chave: Atmosfera solar. Regiões ativas. Magnetismo solar. Espectropolarimetria. Física solar.

LIST OF FIGURES

LIST OF TABLES

Page

LIST OF ABBREVIATIONS

AR	–	Active Region
NOAA	–	National Oceanic and Atmospheric Administration
INPE	–	National Institute for Space Research
HMI	–	Helioseismic and Magnetic Imager
ESO	–	European Southern Observatory
GOES	–	Geostationary Operational Environmental Satellite
LOS	–	Line of sight
RTE	–	Radiative Transfer Equation
IDL	–	Interactive Data Language
WFA	–	Weak Field Approximation
LILIA	–	Lorien Iterative Algorithm
HAO	–	High Altitude Observatory
LTE	–	Local Thermodynamic Equilibrium
F90	–	FORTRAN 90
AIA	–	Atmospheric Imaging Assembly
SDO	–	Solar Dynamics Observatory
SSW/IDL	–	Solarsft instalation on Interactive Data Language
SHARP	–	Spaceweather HMI Active Region Patch
CH	–	Coronal Hole
LTE	–	Local Thermodynamic Equilibrium
PFSS	–	Potential Field Source Surface
NLFFF	–	Non-Linear Force Free Field
LASCO	–	The Large Angle Spectroscopic Coronagraph

LIST OF SYMBOLS

E	–	Electric field
B	–	Magnetic field
ϵ	–	Dieletric permitivity
μ	–	Magnetic permeability
c	–	Speed of light
a_j	–	Component of the electric field amplitude
ω	–	Wave frequency
t	–	Time
δ	–	Phase angle
$\vec{k}$	–	Wave vector
$\vec{r}$	–	Position vector
A_j	–	Component of the Wave amplitude
$\vec{J}$	–	Electron total angular momentum
$\vec{L}$	–	Electron orbital angular momentum
$\vec{S_p}$	–	Electron Spin
N_{comp}	–	Number of components due the Zeeman effect
σ	–	Displaced components of the line
λ	–	Wavelength
g_{eff}	–	Effective Landé factor
λ_B	–	Magnetic field contribution
g	–	Landé factor
κ_σ	–	σ component of light intensity
κ_π	–	π component of light intensity
γ	–	Inclination angle
ϕ	–	Azimuth angle
$C_{i,j}$	–	Polarization matrix element
κ	–	Dimensional constant
τ_c	–	continuum optical depth
$\mathbf{K}$	–	Propagation matrix
$\vec{S}$	–	Source function
$\vec{I}$	–	Stokes intensity vector
$\mu_{I,Q,U,V}$ and $\rho_{U,Q,V}$	–	Absorption and dispersion profiles of the medium
η	–	(Chapter 2) Absorption coefficient
ψ	–	Dispersion coefficient
$B_\nu(T)$	–	Planck function
T	–	Temperature
h	–	Planck constant
ν	–	Frequency
k	–	Boltzmann constant
χ_{cont}	–	frequency-independent absorption coefficient

v – Speed
$\vec{v}$ – Velocity
ρ – Density
$\vec{J}$ – Current density
P – Plasma pressure
$\vec{g}$ – Gravitational force
α – Force free parameter
$\vec{A}$ – Magnetic field potential vector
β – Plasma beta
Φ – Gravitational potential
γ – Torsion angle
σ – Plasma conductivity
η – (Chapter 3) Magnetic diffusivity
L – Typical length scale
R_m – Magnetic Reynolds number
H – Height scale
L_m – Magnetic field relativistic change
u_m – Magnetic energy density
V – Volume
H – Helicity of a field line
U_{free} – Energy budget
U_{nlff} – Energy associated with a non-linear force free magnetic field extrapolation
U_{pot} – Energy associated with a force free magnetic field extrapolation
L_{pol} – Linear polarization

CONTENTS

Page

1 Introduction

The Hertzsprung–Russell, Figure 1.1, is a scatter diagram that classifies stars according to their luminosity and spectral classification. The Sun is located at the main sequence of this diagram, which is where the majority of the stars can also be found, being then considered an ordinary star.

Figure 1.1 - The Hertzsprung–Russell diagram.

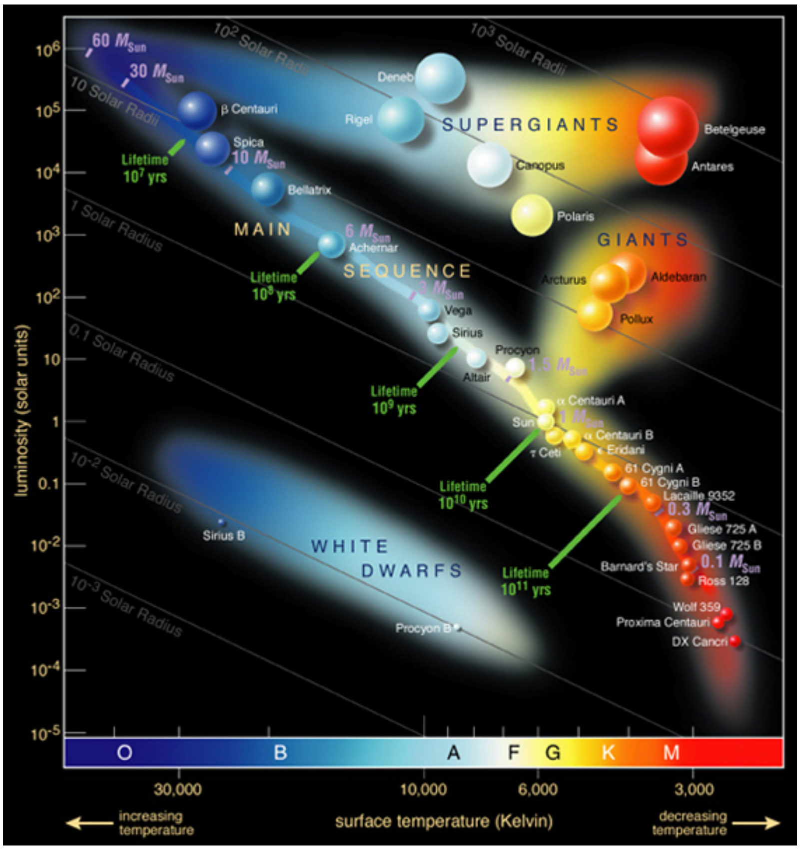

The Hertzsprung–Russell diagram is a very efficient tool for classifying stars. There can be seen how some stars are classified according to the relationship between their luminosity and surface temperature. Note that the majority of the catalogued stars are located within the diagonal of this diagram that is known as ”main sequence”.

SOURCE: European Southern Observatory (2017).

In numbers, some of the Sun basic physical properties can be summarized as: age $\approx$ 4.5 billion years, lifetime: $\approx$ 10 billion years, mass $\approx 1.988 \times 10^{30}\ kg$, radius $\approx 695.700\ km \approx 696\ Mm$ where $1Mm = 10^6\ m$.

Regarding how the physical dimensions and other physical properties of the Sun can be difficult to conceive when compared to the everyday numbers in human life, it is nothing extraordinary in terms of known universe.

The Sun is composed mainly of atoms of Hydrogen that are fused within the core into Helium atoms releasing energy during the process. Traces of heavier elements can also be found as the result of further nuclear fusion processes. These elements are ionized at a high temperature, characteristic of a plasma state, that can reach millions of Kelvin in some regions and are bound together by the gravitational force (SCHRIJVER; ZWAAN, 2000).

Looking through a solar telescope one would notice that the solar surface is dynamic. The motion of the solar plasma is governed by the gravitational and electromagnetic forces. It is worth to take note that depending on the region the gravitational or magnetic field may overcome the influence of each other and be the dominant factor to determine the plasma motion. This is particularly useful when one needs to choose which parameters to consider for a given study.

Based on the observable properties of the Sun, it can be divided in two primary regions being those: the solar interior and the solar exterior. The solar interior can be considered everything below the last visible layer while the solar exterior is everything above it including the visible surface up to the Corona. The photosphere is often referred as being the solar surface marking the beginning of what can be directly seen. Figure 1.2 presents an artistic representation of the solar structure.

Similarly to the layer-divisions that geologists employ to describe the Earth structure, the Sun can also be divided in layers according to the features and properties of each region.

The inner layers of the Sun are: the Core, the Radiation Zone and the Convection Zone while the outer structure of the Sun is composed by the Photosphere, the Chromosphere, the Transition Region and the Corona.

The magnitude of the temperature along the layers can vary from around 15 millions Kelvin at the Core, decreasing to values close to 6000 Kelvin at the Photosphere and rising up to a few millions Kelvin at the Corona as illustrated in Figures 1.3 and 1.4. It is not fully understood the particularity imposed by the sharp gradient of the temperature in the transition region.

The work which will be done following this proposal shall focus in the outer layers of

Figure 1.2 - The structure of the Sun.

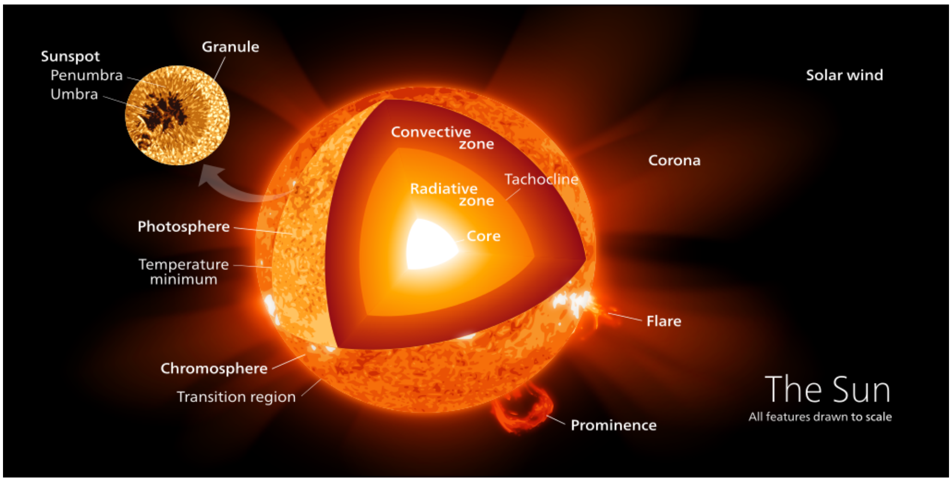

The solar structure and major events that take place within its surface.
SOURCE: By Kelvinsong (Own work) via Wikimedia Commons (2017).

the Sun with a special attention to the Photosphere. Therefore for a more complete description of the Sun and its features can be found at Schrijver e Zwaan (2000).

1.1 The Photosphere

Within the solar outer structure, the photosphere is the lowest layer of the solar atmosphere underneath the chromosphere and the corona marking the top of the convection zone and it is often referred as the solar surface. Since energy is transported by convection in the layer directly below the photosphere, the material in this region is continuously moving.

It can be noticed by observing the Sun through a telescope with an angular resolution close to one second of arc, which covers approximately 725 km at the Sun, that the Photosphere displays a granular pattern. The photosphere is also occasionally populated by Active Regions (ARs) that have a strong magnetic field, which can reach a few thousand Gauss, compared to its surroundings that reach values of a few Gauss. The strong magnetic fields of the ARs locally inhibit the energy transport creating a zone in which the temperature is lower and it may appear darker than its surroundings. Those darker zones called sunspots are maybe the most remarkable structures that populates the solar disk.

An active region is formed by the emergence of strong magnetic flux and may em-

Figure 1.3 - Inner layers temperature.

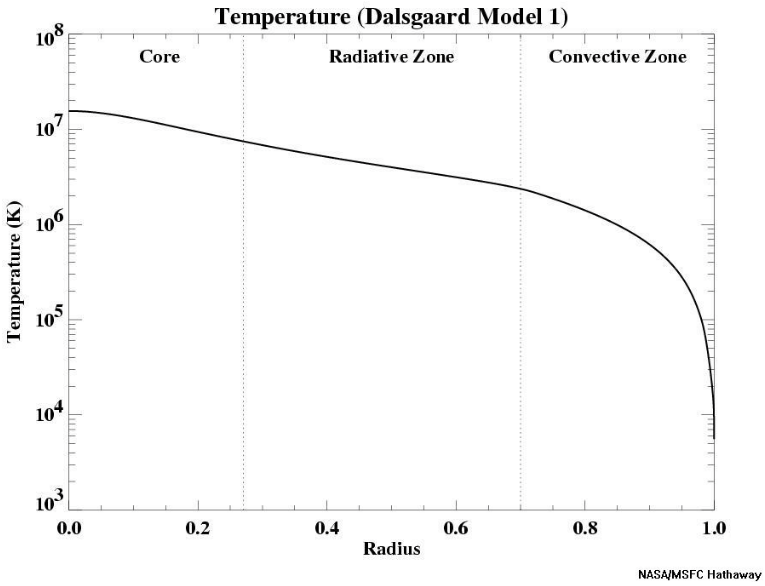

This figure shows a plot of the temperature of the Sun, represented in log-scale in the y-axis, versus the fraction of the radius, x-axis.

SOURCE: NASA - solarscience (2017).

brace sunspots, pores and faculae within its area as represented in Figure 1.5. The sunspot can be considered the heart of an AR and the formation of sunspots is also entwined with the formation process of an active region. Through the measurements of sound-speed perturbations and plasma flow in the layers below sunspots, Zhao et al. (2001) and Kosovichev (2002) found relatively low values for the temperature when compared to its surroundings.

The lifetime of an AR can last from hours to months and will depend on its magnetic flux. Driel-Gesztelyi e Green (2015) published a review regarding the evolution of active regions in which there is a table, reproduced in table 1.1, that summarizes the relation between the magnetic flux and the lifetime of an AR.

The rise of ARs in the solar disk is connected to the solar cycle is characterized by the number of sunspots on the solar disk. In periods of maximum activity a large number of sunspots can be counted. In periods of minimum the number of sunspots can even reach zero.

In the beginning of the solar cycle, sunspots in the solar disk start appearing at

Figure 1.4 - Outer layers temperature.

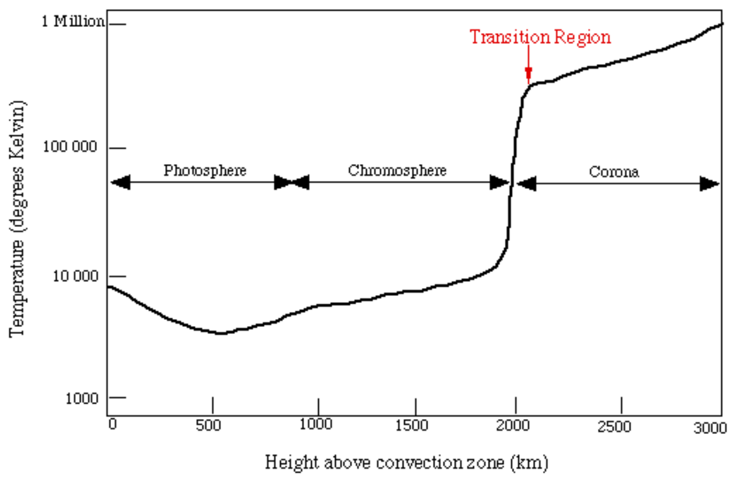

This figure shows how the temperature varies through the external layers.
SOURCE: Solar Physics division - Montana University (2017).

Table 1.1 - Lifetime of active regions according to their magnetic flux and size.

Region	**Magnetic Flux (Mx)**	**Lifetime**	**Rise/Lifetime**
Large (with Sunspots)	5×10^{21} - 3×10^{22}	weeks - months	15-3%
Small (Pores, no spots)	1×10^{20} - 5×10^{21}	days - weeks	15 - 27%
Ephemeral	3×10^{18} - 1×10^{20}	hours-$\approx$ 1 day	$\sim$ 30%

SOURCE: Driel-Gesztelyi e Green (2015).

higher latitudes and, as the cycle passes, those regions appear closer to the equator as the solar cycle unfolds as predicted by Spörer's law. Plotting a historical series of the sunspots location give rise to what is known as the butterfly diagram which is represented in Figure 1.6.

Sunspots and sunspots groups, as represented in Figure 1.7, are classified according to their morphology. A sunspot is said to be regular if it has a single umbra and its structure is reasonably circular. Sunspots can have umbral diameters that vary from 3500 to 60000 kilometers or more. Also there is no apparent dependency between the sizes of the umbra and the penumbra.

Figure 1.5 - Small scale structures.

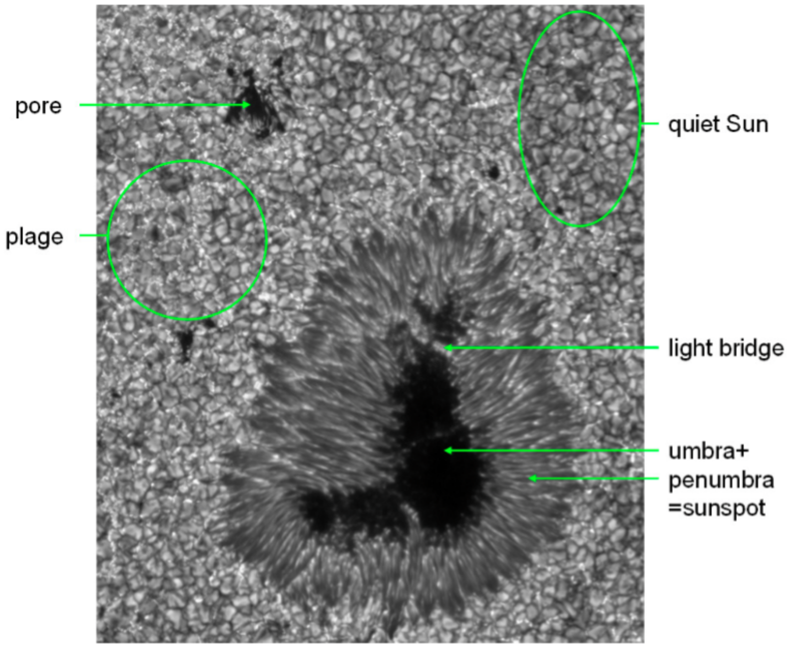

Here it can be seen highlighted some small scale structures of the solar surface.
SOURCE: Rietmuller (2013).

A solar pore can be mistaken as a small sunspot since it can reach 7 Mm in diameter however, differently from sunspots, solar pores lack of a penumbral region.

The magnetic field of a sunspot is more intense at its center and drops monotonically outwards being then the outer penumbral edge the region where it is less intense. The magnetic field is a central quantity for determining the properties of the sunspot and can be measured through the Zeeman effect in photospheric layers. In a similar fashion the magnetic field drops with height, being the gradient more intense when close to the surface of the photosphere. The magnetic field reaches values up to 3000 Gauss at the center of the penumbra.

The magnetic vector is nearly vertical at the umbral region of a sunspot while the penumbral field have, in contrast, an orientation tending to the horizontal. In fact the magnetic field intensity is almost linearly dependent with the angle that measures the inclination of the magnetic vector in relation to the surface normal. At the boundary between the umbra and the penumbra, the average value for the inclination angle is between 70 and 80 degrees.

Figure 1.6 - The Butterfly Diagram.

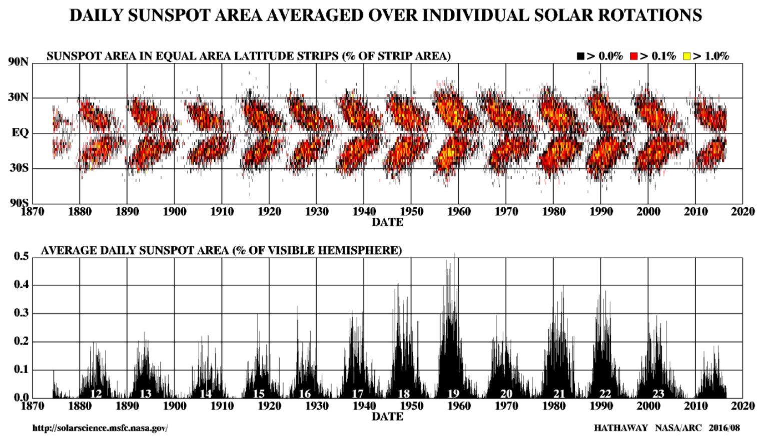

Representations of the sunspots appearance and the solar cycle. This diagram is called butterfly diagram since the pattern created by the rise of sunspots in the solar disk remind that of a butterfly wing.

SOURCE: NASA, Marshal Space Flight Center, Solar Physics (2017).

The magnetic field of a sunspot continues beyond the observable surface taking, in most cases, the shape of an horizontal canopy, as a result of the expansion with height of the magnetic flux tube over the sunspot, with a base in the middle or upper photosphere (SOLANKI, 2002). A representation of the solar canopy made by Wiegelmann et al. (2014) is reproduced in Figure 1.8.

The brightness, unlike the magnetic field intensity, increases together with the distance from the center of the sunspot but not monotonically. However the magnetic flux of the penumbra is from 1 to 1.5 times as intense as in the umbra.

Similarly, the temperature also depends on the spatial position within the spot. However the temperature grows outward the center of the umbra. In the umbra the temperature is 1000-1900 K cooler than the other regions of the quiet Sun while this difference is less pronounced at the umbra region decaying between 240-400 K. The major discussion regarding how the temperature is lower within active regions points that the magnetic field is the responsible for diminishing the temperature by inhibiting the heat flux.

As pointed by Solanki (2003) sunspots are magnetic structures and, as such, one might expect the solar magnetic fields to play a key role on the rise and evolution

Figure 1.7 - Sunspot group.

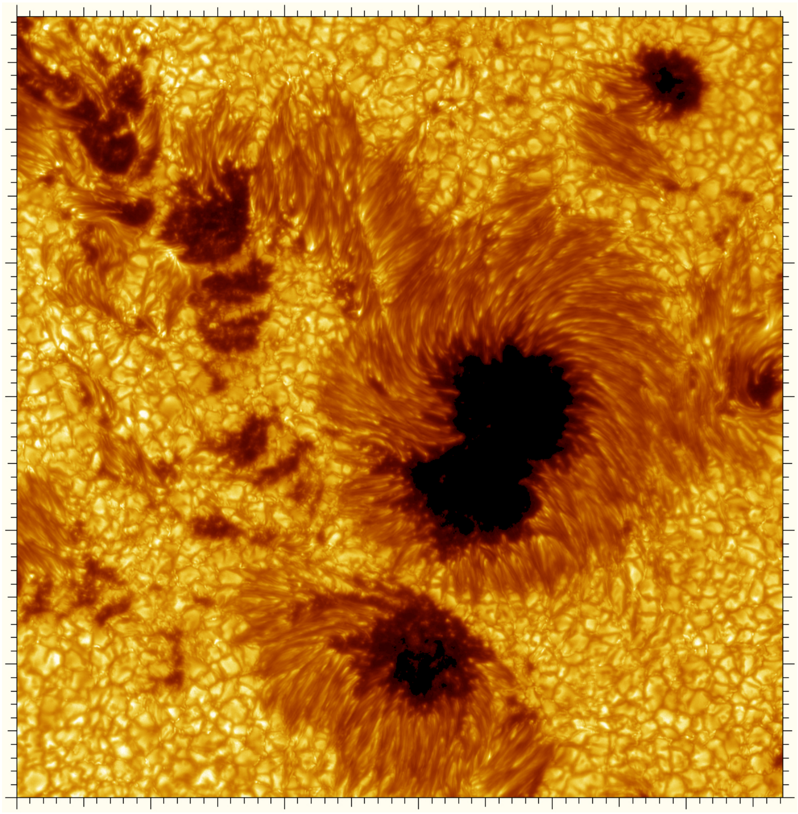

Image of a sunspot group (AR10030) provided by the Swedish Solar Telescope. The distance between two ticks is 1000 km. The penumbra structure, made of filaments, can be clearly noticed enveloping the umbra region.

SOURCE: Institute for Solar Physics of the Royal Swedish Academy of Sciences (2017).

of any active region. For example an increasing in the magnetic flux can be seen in a given region prior to the appearance of pores that later may turn into larger ARs with sunspots. Another point to consider when emphasizing the importance of the magnetic fields to study the behaviour of any solar related phenomena is to recall that the Sun is in a plasma state where the large amount of ionized particles that compose the medium will react to the presence of magnetic fields and magnetic structures defined by it.

1.2 Motivations

Even considering that the life on Earth depends on the Sun much yet has to be done to deeply understand its behaviour or to establish laws that are capable of predict

Figure 1.8 - Sketch of the solar magnetic field structure.

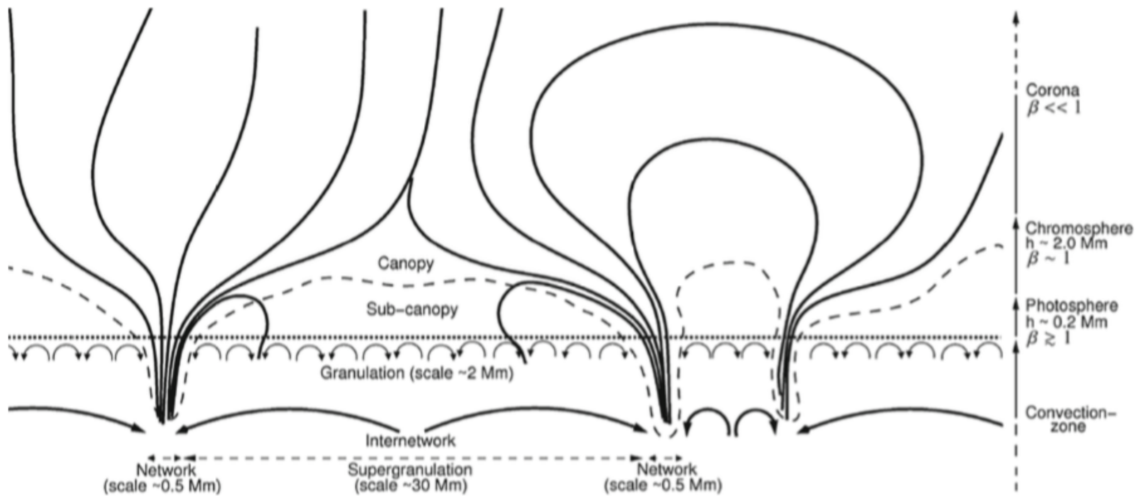

This sketch represents the magnetic field topology over the quiet sun magnetic field structure.

SOURCE: Wiegelmann et al. (2014)

the occurrence of solar phenomena such as flares or CMEs that may result in effects on Earth that range from a small disturbance in the magnetosphere to a collapse of the electrical network. Such extreme effects are more likely to happen in countries at in high latitudes, however, disturbances can also reach mid-latitude regions.

Sunspots are regions that display a strong magnetic field and thus energy. Therefore, most of the energetic phenomena are related to the evolution of those regions where the energy buildup will define the amount of free energy that is available to be released.

Also, there is a wide collection of challenges to understand the behaviour of active regions, for example: processing and working with solar data, improve theories that try to describe the dynamics of the plasma that form the active region and implement routines able to perform better extrapolations of the photospheric magnetic field to the Corona.

1.3 Objectives

1.3.1 Main objective

The main objective of this work is to study the evolution of active regions. The study is focused on the AR NOAA 12443 which was on the solar disk between October 28th and November 10th of 2015. During this period the GOES X-ray sensor registered activity peaks that are characteristic of M-class flares and Coronal Mass Ejections (CMEs) could also be noticed through LASCO making this AR an interesting case-study for being connected with such energetic events.

1.3.2 Specific objectives

The specific objectives are to employ the Stokes profiles and magnetic field extrapolations in order to obtain substantial information regarding the observed region such as:

- Produce solar surface maps to study NOAA 12443 structure;
- Estimate the velocity fields;
- Obtain the magnetic field structure and energy associated to it.

Using the obtained parameters, describe the AR behaviour.

1.4 The structure of this work

The remaining chapters of this work are structured as follows:

- Chapter 2 outlines the knowledge on spectropolarimetry that were pondered upon during the course of this work to study the AR evolution and recover physical properties of the photosphere from the available measurements.
- Chapter 3 presents how magnetic field extrapolations can be used to draw the magnetic structure of a given region and also how the energy budget of the AR can be estimated.
- Chapter 4 shows the results obtained with the Stokes profiles.
- Chapter 5 shows the results obtained with the magnetic field extrapolations.

- Chapter 6 focuses on studying the possible causes of NOAA 12443 flaring activity.

- Chapter 7 presents the compilation of the results concluding the study.

2 Spectropolarimetry

2.1 Introduction

When a telescope is observing some object it is, in fact, measuring the energy of the electromagnetic radiation that the object is producing or reflecting. However for many purposes, including the study the Sun, the energy output for itself does not directly present enough information. Fortunately, more information can be obtained and inferred from a beam of light. More precisely, what a telescope measure is the Poynting Vector of a beam of light.

The formalism discussed in this chapter can be used to study the "entirety" of the electromagnetic spectrum. However, since this study focus on the visible part of the electromagnetic spectrum with a special attention to the neutral iron line (FeI), the word light will be used to describe the object of study. The neutral iron line is particularly interesting since it is a photospheric line, in the visible region, with a moderately large Landé factor. These properties shall be described along the chapter

Light can behave as a particle and also as a wave being commonly referred as wave packets. As a wave, while the electromagnetic wave propagates itself, the electric and magnetic fields associated with it oscillates both perpendicular to the direction of propagation of the wave.

Treating a monochromatic beam of light as a set of harmonic plane waves, it can be described using the homogeneous wave equation[1]:

$$\nabla^2 \vec{E} - \frac{\epsilon\mu}{c^2}\ddot{\vec{E}} = 0 \tag{2.1}$$

Where ϵ and μ are, respectively, the dielectric permittivity and magnetic permeability, c is the speed of light and $\vec{E}$ is the electric field vector. As it can be seen, Equation 2.1 involves a second derivative in space of a function that return the second derivative in time of the same function which is characteristic of an harmonic oscillator. Therefore, as one might expect, the solution of such equation is a harmonic function of the type:

[1]As stated above, both electric and magnetic fields are oscillating and would follow an homogeneous wave equation. However the electric field is usually used to describe the electromagnetic radiation.

$$E_j = a_j e^{-i(\omega t - \delta_j)} \tag{2.2}$$

Where ω is the angular frequency, t stands for time, δ is the phase angle and a_j is given by:

$$a_j = A_j e^{i\vec{k}\cdot\vec{r}} \tag{2.3}$$

Being $\vec{k}$ the wave vector, $\vec{r}$ is the position and A_j is the wave amplitude. Therefore, a wave which is propagating along the z-axis could be described as:

$$\begin{aligned} E_x &= a_x e^{-i(\omega t - \delta_x)} \\ E_y &= a_y e^{-i(\omega t - \delta_y)} \\ E_z &= 0 \end{aligned} \tag{2.4}$$

Where E_x, E_y and E_z are the components of the electric field. The polarization tensor of this wave can then be defined as:

$$C = \begin{pmatrix} E_x E_x^* & E_x E_y^* \\ E_y E_x^* & E_y E_y^* \end{pmatrix} \tag{2.5}$$

Being E_x^* and E_y^* the complex conjugate of, respectively, E_x and E_y. Therefore, the polarization tensor can be written as:

$$C = \begin{pmatrix} a_x^2 & a_x a_y \cdot e^{i\delta} \\ a_x a_y \cdot e^{-i\delta} & a_y^2 \end{pmatrix} \tag{2.6}$$

Where the phase difference δ is the constant phase difference δ between the different components of the electric field vector:

$$\delta = \delta_x - \delta_y \tag{2.7}$$

The polarization specifies the geometrical orientation of the electric field vector oscillation with respect to the wave vector ($\vec{k}$) and unveil some properties of the wave that are represented in Figure 2.1. Those geometries are explored by the Stokes

Figure 2.1 - Polarization and phase difference.

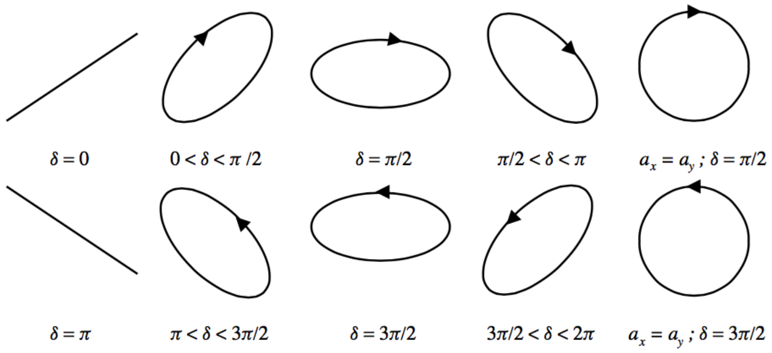

This figure pictures the different geometries described by light polarization depending on the phase difference δ.

SOURCE: Iniesta (2003).

parameters to fully describe the electromagnetic radiation and are going to be addressed over the next sections of this work.

In the solar physics context, spectropolarimetry is the set of techniques that allow someone to establish the connection between the properties of polarized light and other quantities that are key for a better understanding such as the magnetic field, whose importance was already discussed on previous sections.

Spectropolarimetry is mainly based in three formalisms:

- The Zeeman Effect: that explains how the spectral lines emitted by an atom change in the presence of a magnetic field;
- The Stokes Parameters: that are used to fully characterizes the degree of polarization of a beam of light;
- The Radiative Transfer Equation (RTE): which describes the interaction between radiation and matter.

Those subjects will be discussed taking as a reference for notation and the order in which the topics are presented the text written by González (2006).

2.2 The Zeeman Effect

It is known that the protons and neutrons are bound together forming a nucleus by the action of a strong force and that the electrons have a very particular movement around this nucleus.

Such movement defines the orbital angular momentum of the electrons ($\vec{L}$). Furthermore electrons have Spin ($\vec{S_p}$), that is a form of angular momentum inherent of elementary particles.

Therefore the total angular momentum ($\vec{J}$) of the electron is given by the sum of orbital angular momentum and spin:

$$\vec{J} = \vec{L} + \vec{S_p} \tag{2.8}$$

The essence of the Zeeman Effect resides in the consequences that the broken degeneracy of the J states due to the presence of a magnetic field brings to the observed emission line. If the magnetic field is sufficiently strong and the line sensitive to it, the emission line will split into components.

There are however more possibilities then what is represented by the "normal" Zeeman effect, which is the degeneracy of a state resulting in the classic triplet, which may result in more lines appearing where the number of components (N_{comp}) can be calculated as a function of the energy level J by a fairly simple expression:

$$N_{comp} = 2J + 1 \tag{2.9}$$

This phenomenon is called "anomalous" Zeeman effect that, in fact, is the most general case of the Zeeman effect. However, an effective triplet can be used for substituting an anomalous one for the sake of simplicity as illustrated in Figure 2.2.

The displacement of the σ components illustrated in Figure 2.2 of the light emitted by the atom may be calculated as:

$$\Delta\lambda_{\pm\sigma} = \mp g_{eff} \frac{e\lambda_0^2}{4\pi m_e c} B \tag{2.10}$$

Where e and m_e are the electron charge and mass and λ_0 is the original wavelength of

Figure 2.2 - Zeeman splitting diagram.

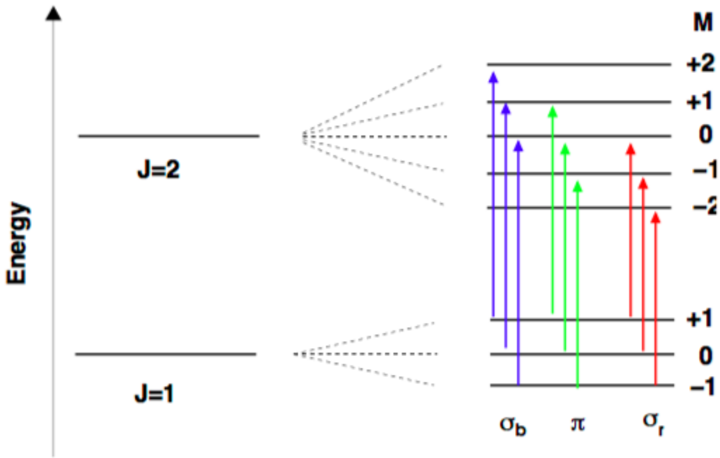

The single-line emission breaks into a multiplet when exposed to a magnetic field as a consequence of the Zeeman effect.

SOURCE: Santiago (2004).

the observed line. The sub-index σ refers to the displaced components of the triplet being those commonly denoted as σ_r and σ_b. The sub-index π refers to the principal component of the triplet. Equation 2.10 states which is the proportionality constant between the line separation and the magnetic field being this constant called the effective Landé factor (g_{eff}).

The Landé factor is a multiplicative term associated with a small perturbation in the electron energy state and it can be calculated as a function of the energy states of the electron:

$$g_{eff} \equiv \frac{3}{2} + \frac{S_p(S_p+1) - L(L+1)}{2J(J+1)} \tag{2.11}$$

The Landé factor accounts for the sensitivity of a line to be separated when exposed to a magnetic field. Therefore, as predicted by Equation 2.10, both the Landé factor of a line and the magnetic field will define the distance between two lines after the separation.

2.3 Stokes Parameters

In 1852 George Gabriel Stokes defined a set of four parameters capable of fully describe the electromagnetic radiation intensity and polarization degree. Those parameters are commonly symbolized by the letters I, Q, U and V and will be presented bellow following the description made by (DEGL'INNOCENTI, 1992).

⇒ I denotes the total intensity of the light in a given spectral range and can be approximated by the following expression :

$$I \approx \frac{\kappa_\sigma}{4}(1 + cos^2\gamma) + \frac{\kappa_\pi}{2}sin^2\gamma \tag{2.12}$$

Being the terms κ_σ and κ_π represent the σ and π components of the spectral line and γ is the inclination angle between the magnetic field present in the observed region and the direction of propagation of the light (see Figure 2.3).

⇒ Q and U express the fraction of the intensity which light is linearly polarized and can be approximated as:

$$Q \approx B^2 sin^2\gamma cos2\phi \tag{2.13}$$

$$U \approx B^2 sin^2\gamma sin2\phi \tag{2.14}$$

Where B is the intensity of the magnetic field ϕ is the azimuth angle of the magnetic field vector.

⇒ V accounts for the fraction of the intensity which light is circularly polarized and can be approximated as:

$$V \approx Bcos\gamma \tag{2.15}$$

In a more precise way, the Stokes parameters can be defined as a function of the polarization matrix C that is represented in Equation (2.6):

Figure 2.3 - Line of sight geometry.

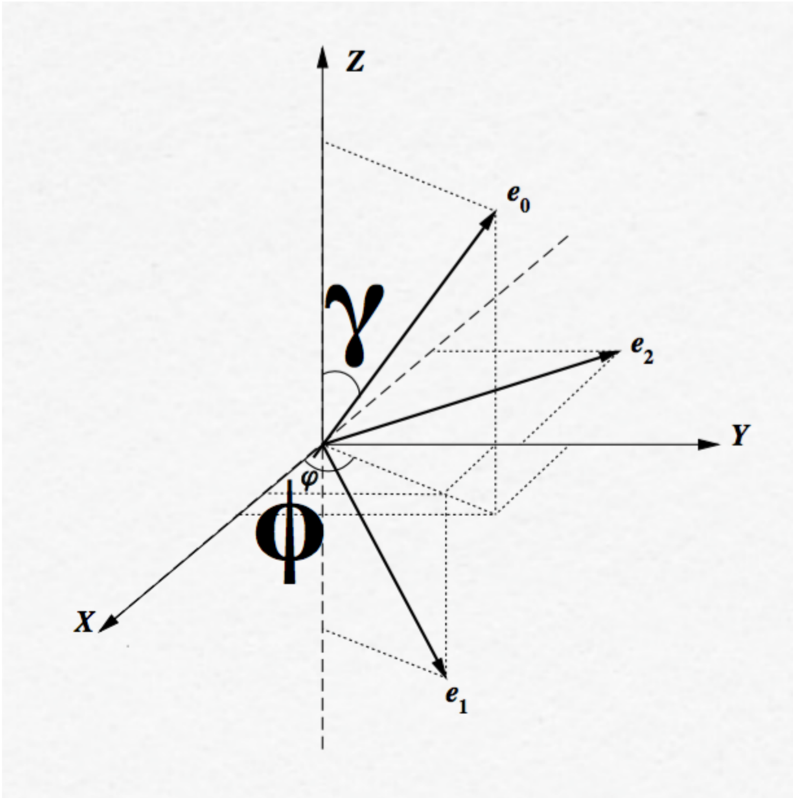

Considering that the Line Of Sight (LOS) is parallel to the z-axis, γ represents how much the magnetic field vector is inclined in the direction of the observer while ϕ will define the direction in respect to the x-y plane.

SOURCE: Original source: Iniesta (2003) Figure 7.1, adapted by J. Palacios.

$$\begin{aligned}
I &\equiv \kappa(C_{11} + C_{22}) &=& \kappa(a_x^2 + a_y^2) \\
Q &\equiv \kappa(C_{11} - C_{22}) &=& \kappa(a_x^2 - a_y^2) \\
U &\equiv \kappa(C_{12} + C_{21}) &=& 2\kappa a_x a_y cos\delta \\
V &\equiv i\kappa(C_{21} - C_{12}) &=& 2\kappa a_x a_y sin\delta
\end{aligned} \tag{2.16}$$

Experiments can be performed in order to measure the degree of polarization of the light and, consequently, the parameters of Stokes. The four parameters and its dependence on a spectral line are called the Stokes Profiles. The degree of polarization of the electromagnetic wave and, consequently, the parameters of Stokes can be directly measured.

Figure 2.4 shows the measurements of the Stokes parameters of a region on the solar disk. The horizontal blue arrow points the direction where the wavelength increase. The wavelength at the origin is equal to 6300.8900 Å, the measurements are made with an interval of 21.5 mÅ and have a spectral resolution of 112 pixels so they comprise up to 6303.298 Å. The vertical blue arrow is a reference in pixels for the spatial resolution. The green arrows indicates the neutral iron lines (FeI) 6301.5107 Å and 6302.5000 Å where most of the radiation is absorbed as can be clearly seen by a Stokes I profile. The usual topology of the Stokes profiles when measured over regions similar to the ones highlighted by the red arrows 1 and 2 are represented in Figures 2.5 and 2.6.

Figure 2.5 brings an example of how the Stokes profiles looks like when measured over a region without a considerable magnetic field such as an AR. Figure 2.5 brings an example of how the Stokes profiles looks like when measured over a region without a considerable magnetic field such as the quiet Sun.

Figure 2.4 - Stokes parameters measurements.

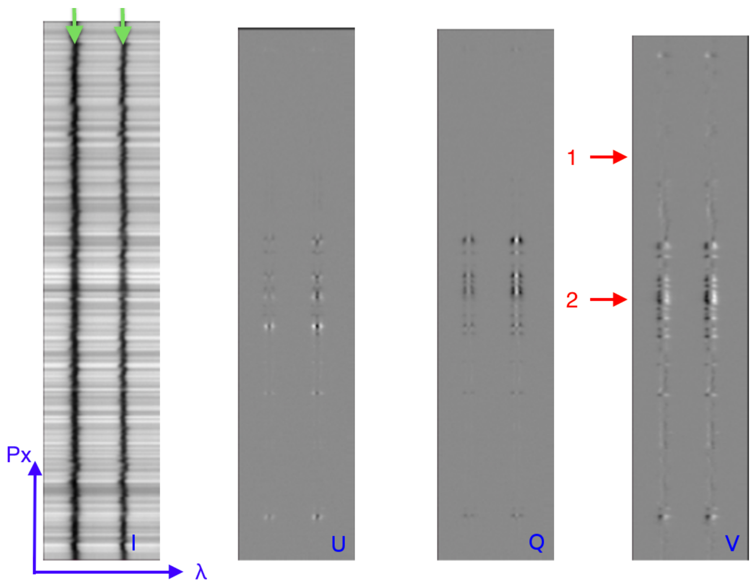

Starting from the top left-hand side there are the measurements of Stokes I, Q, U and V of AR NOAA 12443 obtained through Hinode Telescope at 2015/11/03 - 14:15:49.

SOURCE: Author's own work.

Figure 2.5 - Stokes profiles of a region with a negligible magnetic field.

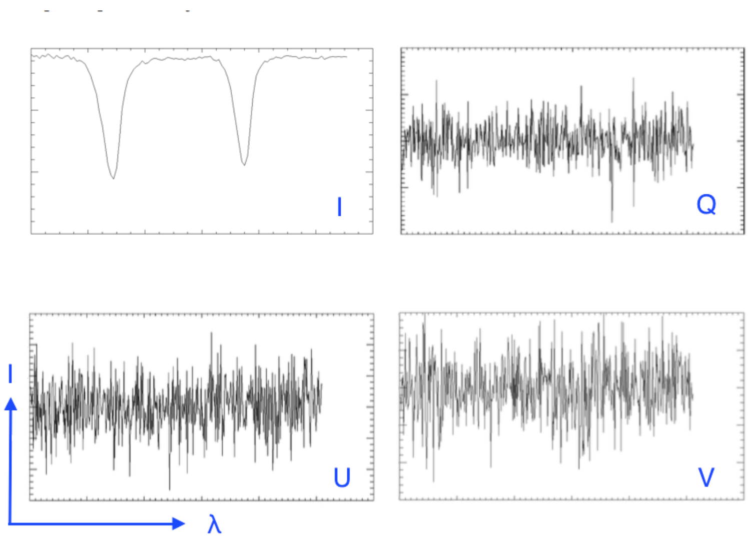

Starting at the top left-hand side and going clockwise it is presented the topology of the normalized line profile of Stokes I, Q, V and U obtained of AR NOAA 12443 obtained through Hinode Telescope at 2015/11/03 - 14:15:49. When not covering a region where the magnetic field is strong the Stokes profiles have a shape that resemble a noise signal.

SOURCE: Author's own work.

2.4 Radiative Transfer Equation

The light captured by a device, being it based on Earth or in space, interacted with matter along its path resulting in changes. On its way from the photosphere to a telescope a photon would have to pass through the solar atmosphere and, if the telescope is ground based, through the Earth's atmosphere as well.

The Radiative Transfer Equation (RTE) plays a role that is, in some aspects, similar to the use of the Zeeman effect since it is a formalism that can be used to reconstruct the original condition in which the photon detected by the device was emitted.

The assumption that the Sun is in local thermodynamic equilibrium (LTE), which is equivalent to say that only radiation is allowed to deviate from the equilibrium state. Also it is assumed that the atmosphere is magnetised. The RTE for a polarized light in a plane-parallel atmosphere can be written as the rate of change of the Stokes vector $\vec{I}$ along a path with continuum optical depth (τ_c) (INIESTA, 2003):

Figure 2.6 - Stokes profiles of a region with an intense magnetic field.

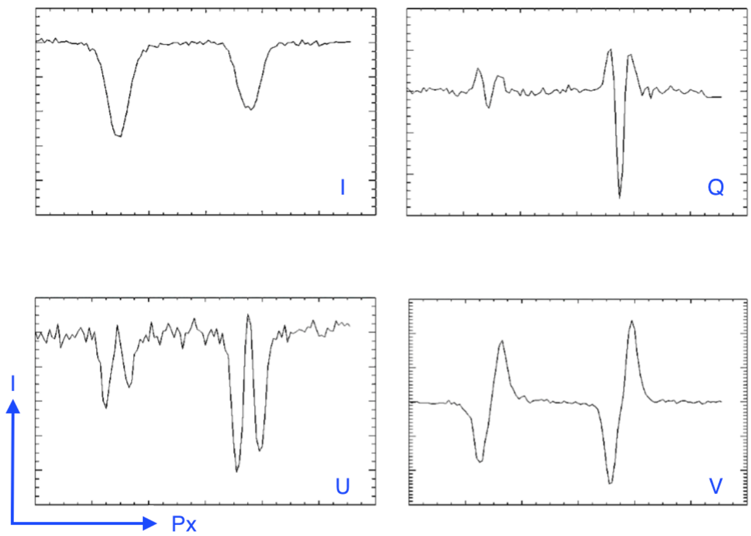

Starting at the top left-hand side and going clockwise it is presented the topology of the normalized line profile of Stokes I, Q, V and U of AR NOAA 12443 obtained through Hinode Telescope at 2015/11/03 - 14:15:49UT. Unlike from figure 2.5, this plot covers a region where the magnetic field is significant, covering an AR, and the characteristic topology of each Stokes profile can be promptly spotted.

SOURCE: Author's own work.

$$\frac{d\vec{I}}{d\tau_c} = -\mathbf{K}(\vec{I} - \vec{S}) \tag{2.17}$$

Where $\vec{S}$ is the source function vector responsible to consider the emissivity and $\mathbf{K}$ is the propagation matrix that can be written as (INIESTA, 2003):

$$\mathbf{K} = \begin{pmatrix} \eta_I & \eta_Q & \eta_U & \eta_V \\ \eta_Q & \eta_I & \rho_V & -\rho_U \\ \eta_U & -\rho_V & \eta_I & \rho_Q \\ \eta_V & \rho_U & -\rho_Q & \eta_I \end{pmatrix} \tag{2.18}$$

The matrix elements (η) and (ρ) are given by:

$$\eta_I = 1 + \frac{\eta_0}{2}\left[\chi_p sin^2\gamma + \frac{\chi_b + \chi_r}{2}(1 + cos^2\gamma)\right]$$

$$\eta_Q = \frac{\eta_0}{2}\left[\chi_p + \frac{\chi_b + \chi_r}{2}\right] sin^2\gamma cos2\phi$$
$$\eta_U = \frac{\eta_0}{2}\left[\chi_p + \frac{\chi_b + \chi_r}{2}\right] sin^2\gamma sin2\phi$$
$$\eta_V = \frac{\eta_0}{2}\left[\chi_r - \chi_b\right] cos\gamma$$
$$\rho_Q = \frac{\eta_0}{2}\left[\chi_p - \frac{\psi_b + \psi_r}{2}\right] sin^2\gamma cos2\phi$$
$$\rho_U = \frac{\eta_0}{2}\left[\psi_p - \frac{\psi_b + \psi_r}{2}\right] sin^2\gamma sin2\phi$$
$$\rho_V = \frac{\eta_0}{2}\left[\psi_r - \psi_b\right] cos\gamma$$

Where ($\chi_{p,r,b}$) and ($\psi_{p,r,b}$) are, respectively, the absorption and the dispersion coefficients and (γ) and (ϕ) are the inclination and azimuth angles between the magnetic field and the direction of propagation of the light. The index p stands for the principal (π) component while the indexes b (blue) and r (red) accounts for the σ components of a Zeeman multiplet.

Therefore, the elements $\eta_{I,Q,U,V}$ and $\rho_{Q,U,V}$ take into consideration not only the absorption and dispersion profiles of the medium but also the geometry that is being used to describe the radiation path. A deduction and further discussion of those elements can be found at Chapter 7.3 of (INIESTA, 2003).

The stokes vector ($\vec{I}$) is given by an array containing the four Stokes parameters:

$$\vec{I} = \begin{pmatrix} I \\ Q \\ U \\ V \end{pmatrix} \tag{2.19}$$

The emissivity properties of the medium, accounted in $\vec{S}$, are defined as:

$$\vec{S} \equiv (B_\nu(T), 0, 0, 0)^T \tag{2.20}$$

Where $B_\nu(T)$, under LTE, is the Planck function given by:

$$B_\nu(T) = \frac{2h\nu^3}{c^2(e^{\frac{h\nu}{kT}} - 1)} \tag{2.21}$$

Both source and Planck's functions are local quantities. The evolution of the light's intensity as it passes through the medium can only be known if the physical properties of the medium are given. An atmosphere model can then be employed to emulate such properties based in a set of assumptions regarding the properties.

The continuum optical depth (τ_c) is defined as:

$$\tau_c = \int_z^{z_0} \chi_{cont} dz \tag{2.22}$$

Being χ_{cont} the frequency-independent absorption coefficient for the continuum radiation, that will account for the material properties of the medium, and the limits represent the path that is oriented in the direction $(-\hat{z})$ from the starting point of integration z toward the observer that is considered to be at z_0.

3 Magnetic field extrapolations

3.1 Introduction

In the previous section we mentioned that the magnetic field can be measured using the Zeeman effect. However this is only possible within the limits of the photosphere. Below the photosphere it is not acessible for telescopes while above it only the shape of the magnetic field lines can be inferred by polarimetry. There are, however, methods that allow the magnetic field of the corona to be extrapolated from what is measured in the photosphere as proposed by Nakagawa e Raadu (1972). For more specific information regarding this subject, Wiegelmann e Sakurai (2012) recently provided an updated review.

3.2 Force free magnetic field extrapolations

For this work purposes the Sun is treated using the ideal MHD equations. There are three general assumptions (SCHRIJVER et al., 2011): the validity of the continuum approximation and non-relativistic dynamics, the quasi-neutrality of the plasma and that the collisional coupling between different ions constituting the plasma is sufficiently strong to treat the plasma as a single fluid.

In order to extrapolate the field one assumes the validity of the ideal magnetohydrodynamics (MHD) equations:

- Mass conservation (continuity equation):

$$\frac{\partial \rho}{\partial t} + \nabla \cdot (\rho \vec{v}) = 0 \tag{3.1}$$

- Second Newton's law for fluids:

$$\rho \frac{d\vec{v}}{dt} = -\nabla P + \vec{J} \times \vec{B} + \rho \vec{g} \tag{3.2}$$

  Where:

$$\frac{d}{dt} = \frac{\partial}{\partial t} + \vec{v} \cdot \nabla \tag{3.3}$$

- Adiabatic equation for fluids:

$$\frac{d}{dt}\left(\frac{P}{\rho^{\gamma}}\right) = 0 \tag{3.4}$$

- Ideal Ohm's Law for fluids:

$$\vec{E} + \vec{v} \times \vec{B} = \vec{0} \tag{3.5}$$

- Gauss's law for magnetism:

$$\nabla \cdot \vec{B} = 0 \tag{3.6}$$

- Faraday's law:

$$\frac{\partial \vec{B}}{\partial t} = -\nabla \times \vec{E} \tag{3.7}$$

- Low frequency Maxwell-Ampère law:

$$\nabla \times \vec{B} = \mu_0 \vec{J} \tag{3.8}$$

Where $\vec{v}$ is the fluid velocity, $\vec{J}$ is the current density, ρ is the mass density, P is the plasma pressure and t is time.

From equations 3.5 and 3.7 the temporal evolution of the magnetic field can be written as:

$$\frac{\partial \vec{B}}{\partial t} = \nabla \times (\vec{v} \times \vec{B}) \tag{3.9}$$

To verify the limits where the ideal MHD descriptions stand true it is necessary to regard the Ohm's law, that can be written in it more simplistic form as:

$$\vec{J} = \sigma(\vec{E} + \vec{v} \times \vec{B}) \tag{3.10}$$

Being the plasma conductivity (σ) represented by:

$$\sigma = \frac{\tau_{ei} n_e e^2}{m_e} \tag{3.11}$$

Where τ_{ei} is the collision time between electrons and ions, n_e is the electron density, e is the electron charge, and m_e the electron mass. The temporal evolution of the magnetic field, combining equations (3.7) and (3.10), is:

$$\frac{\partial \vec{B}}{\partial t} = \nabla \times (\vec{v} \times \vec{B}) + \eta \nabla^2 \vec{B} \tag{3.12}$$

Where the magnetic diffusivity η is given by:

$$\eta = \frac{1}{\mu_0 \sigma} \tag{3.13}$$

An adimensional analysis of the terms on the right hand side of equation 3.12, leads to a characteristic distance (L) to describe the evolution of the parameters:

$$\nabla \rightarrow \frac{1}{L}$$

Dividing the terms on the right hand side of equation 3.12 lead to the following:

$$\frac{\mid \nabla \times (\vec{v} \times \vec{B}) \mid}{\eta \mid \nabla^2 \vec{B} \mid} = \frac{vL}{\eta} \tag{3.14}$$

Where L is the typical length scale, v is the characteristic velocity of the studied region. The magnetic Reynolds number R_m is given by:

$$R_m = \frac{vL}{\eta} \tag{3.15}$$

The validity of the ideal MHD approach can be verified using the magnetic Reynolds number which will state whether the regime is dominated by diffusion or advection. The coronal loop typical length scale is around 10^8 m while the characteristic velocity is around (100 $\mathrm{ms^{-1}}$) and the magnetic diffusivity is usually (1 $\mathrm{m^2 s^{-1}}$), which would lead to a magnetic Reynolds number of the order 10^{10}, but the magnetic diffusivity can reach up to (10^8 $\mathrm{m^2 s^{-1}}$) in turbulent regions reducing the values of the magnetic Reynolds number to the order of 10^2 (SCHRIJVER et al., 2011). Therefore, there are two distinct types of regime based on the magnetic Reynolds number:

- $R_m >> 1$: the advection dominated regime. The induction equation reduces to the ideal MHD equation. Thus, the MHD approach is valid. Then:

$$\frac{\partial \vec{B}}{\partial t} = \nabla \times (\vec{v} \times \vec{B}) \tag{3.16}$$

Which is consistent with equations 3.5 and 3.7.

- $R_m << 1$: the diffusion dominated regime. In turbulent regions the induction equation take the form:

$$\frac{\partial \vec{B}}{\partial t} = \eta \nabla^2 \vec{B} \tag{3.17}$$

A diffusion dominated regime would go against the general assumptions since the heat diffusion would prevent the ions from being in the same temperature and, thus, the LTE conditions would not be validy.

The magnetic Reynolds number of ARs is indeed large (HOOD; HUGHES, 2011) ensuring then that the heating exchange is negligible and, thus, the ideal MHD approach can be used to study such regions.

In static equilibrium ($\vec{v} = \vec{0}$), equation 3.2 holds that:

$$-\nabla P + \vec{J} \times \vec{B} + \rho \vec{g} = \vec{0} \tag{3.18}$$

Comparing the magnitude of each force represented in the left hand side of equation 3.18 against the cross product between the electric current and the magnetic field, for the pressure gradient:

$$\frac{\nabla P}{\mid \vec{J} \times \vec{B} \mid} = \frac{\nabla P}{\mid \frac{\nabla \times \vec{B}}{\mu_0} \times \vec{B} \mid} \approx \frac{P}{\frac{B^2}{2\mu_0}} \tag{3.19}$$

The ratio (β) between the plasma pressure (P) and the magnetic pressure, known as plasma-β, is:

$$\beta = 2\mu_0 \frac{P}{B^2} \tag{3.20}$$

Therefore, if $\beta << 1$ the force related to the pressure gradient can be disregarded when compared to the magnetic pressure. Figure 3.1 shows the predicted changes of the plasma β values with height.

Figure 3.1 - Plasma beta model.

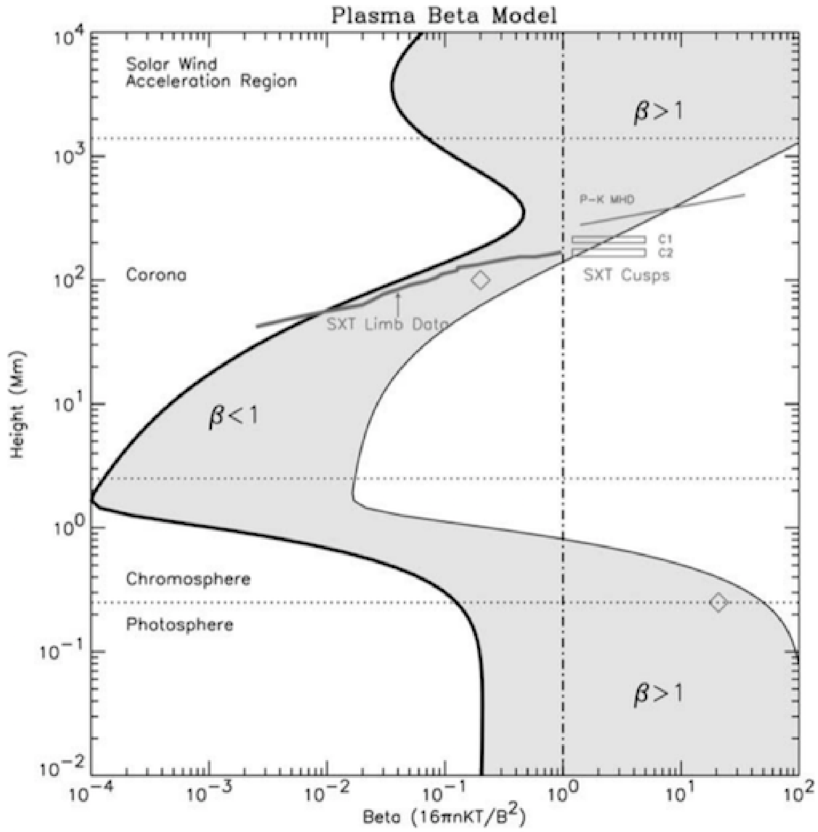

The values of β starts decaying from the photosphere until the Corona.
SOURCE: Gary (2001).

Typical values for pressure and magnetic field will vary accordingly to the region, some examples are exhibited in Table 3.1 which is adapted from Aschwanden (2005). It can be seen that the cool and hot corona indeed have low values of plasma-β, which is not true however for the photosphere and outer corona. Thus, the hot and cool corona can be said to be approximately free of forces.

Taking the coronal density ($n_0 \approx 10^{15}$ m^{-3}, $\rho \approx 1.67 \times 10^{-12}$ kg m^{-3}) at a distance $r \approx 8 \times 10^8$ m which is 100 Mm above the photosphere and using the results obtained for NOAA 12443 for $\vec{J}$ and $\vec{B}$ results in:

$$| \rho\vec{g} | << | \vec{J} \times \vec{B} | \tag{3.21}$$

Table 3.1 - Values for magnetic field and pressure at the solar atmosphere.

Parameter	**Photosphere**	**Cool corona**	**Hot corona**	**Outer corona**
Pressure (dyn/cm^2)	1.4×10^5	0.3	0.9	0.02
Magnetic field (G)	500	10	10	0.1
Plasma-β	14	0.07	0.2	7

SOURCE: Adapted from: Aschwanden (2005)

Then the gravitational force can also be disregarded thus, under those conditions, the field is said to be free of forces.

From Equations 3.19 and 3.21 the force free condition arises, where:

$$\vec{J} \times \vec{B} = \vec{0} \tag{3.22}$$

3.2.1 The force free parameter

Equation 3.22 states that $\vec{J} \parallel \vec{B}$, or, introducing a parameter $\alpha(\vec{r})$:

$$\vec{J} = \alpha(\vec{r})\vec{B} \tag{3.23}$$

From Ampere's law (Equation 3.8):

$$\nabla \times \vec{B} = \mu_0 \alpha(\vec{r})\vec{B} \tag{3.24}$$

Taking the divergence of Equation 3.24:

$$\nabla \cdot \left[\alpha(\vec{r})\vec{B}\right] = \vec{B} \cdot \nabla\alpha(\vec{r}) + \alpha(\vec{r})\nabla \cdot \vec{B} \tag{3.25}$$

Therefore:

$$\vec{B} \cdot \nabla\alpha(\vec{r}) = 0 \tag{3.26}$$

It is possible to state from Equation 3.26 that:

- $\vec{B}$ is over the surface of constant alpha.
- $\alpha(\vec{r})$ is constant along each field line but it can vary according to each line.

From Ampere's law the component of the electric current along the z-axis is:

$$\mu_0 J_z = \left(\frac{\partial B_y}{\partial x} - \frac{\partial B_x}{\partial y}\right) \tag{3.27}$$

Also, from Equation 3.24, the component of the electric current along the z-axis is:

$$\left(\frac{\partial B_y}{\partial x} - \frac{\partial B_x}{\partial y}\right) = \mu_0 \alpha(\vec{r}) B_z \tag{3.28}$$

Since $\alpha(\vec{r})$ is constant along a field line, if the magnetic field vector is known for $z = 0$, the mapping of $\alpha(\vec{r})$ for the photosphere can be written using Equations 3.27 and 3.28 as:

$$\alpha(x, y, z = 0) = \mu_0 \frac{J_z}{B_z}\bigg|_{z=0} = \frac{\left(\frac{\partial B_y}{\partial x} - \frac{\partial B_x}{\partial y}\right)}{B_z}\Bigg|_{z=0} \tag{3.29}$$

The force free parameter then is propagated for $z > 0$ in the volume along the field lines. The typical values of $\mid \alpha \mid$ in ARs would be between 0 and 0.05 Mm^{-1}.

From the definition it can be noted that the force free parameter is a function of the position henceforth it is worthwhile to enforce that α is constant along a field line.

The force free parameter is associated with the magnitude and direction of the electric current density. Topologically, α induces a torsion in the magnetic field lines. The direction of this torsion depends on the sign of α.

Essentially, there are three different types of magnetic fields extrapolations that differ from one another according to the assumption made on the force free parameter ($\alpha(\vec{r})$):

- Consider that alpha is zero:

$$\alpha(\vec{r}) = 0$$

Therefore, from Equation (3.24):

$$\nabla \times \vec{B} = \vec{0} \tag{3.30}$$

The magnetic field can then be obtained from a potential ($\phi(\vec{r})$):

$$\vec{B} = \nabla\phi(\vec{r}) \tag{3.31}$$

Taking the divergence of Equation 3.31 it can be seen that the potential ($\phi(\vec{r})$) can be described by Laplace's equation:

$$\nabla^2\phi(\vec{r}) = 0 \tag{3.32}$$

Therefore, this configuration represents the minimum energy state of the system which is a potential field in the absence of electric currents.

- Consider that alpha is a constant over the entire space:

$$\alpha(\vec{r}) = \alpha_0$$

Under this assumption the orientation of the magnetic field will be the same over the surface of the force free distribution. The magnetic field can be described by the Helmholtz's equation:

$$\nabla^2\vec{B}(\vec{r}) + \alpha_0^2\vec{B}(\vec{r}) = \vec{0} \tag{3.33}$$

This kind of assumption characterizes a linear force free approach.

- Consider that alpha varies along space:

$$\alpha = \alpha(\vec{r})$$

In a non-linear force free approach, the equations:

$$\nabla \times \vec{B} = \alpha(\vec{r})\vec{B}$$

(3.34)

$$\vec{B} \cdot \nabla\alpha = 0 \tag{3.35}$$

Must be satisfied.

Regardless of the assumption for the force free parameter, however, the appropriate boundary conditions must be used.

For a review of techniques for magnetic field extrapolations Wiegelmann e Sakurai (2012) covers the most used methods such as: Grad & Rubin, Optimization, Vertical Integration, Evolutionary,etc. Each method is based on different assumptions and boundary conditions offering a diversity of tools to study the magnetic field under different situations. For this study an algorithm using the optimization approach was used and it shall be discussed in the following chapters.

3.3 Energy budget

The magnetic energy density (u_m) is given by:

$$u_m = \frac{B^2}{2\mu_0} \tag{3.36}$$

Therefore, for a given area of the Sun disk, the magnetic energy of a given volume of the sun disk can be calculated by integrating the magnetic field contribution over the studied volume:

$$U_m = \int_V \frac{B^2}{2\mu_0} dV \tag{3.37}$$

Since the energy associated with a region is dependent on the magnetic field it is expected that different values for the energy will be found according to the method used to extrapolate the field.

The potential field methods ($\alpha = 0$), for instance, can retrieve the value of free magnetic energy necessary to create eruptive process, such as flares, even representing the simplest possible configuration for the system however the approach is unrealistic since it does not consider the presence of electric currents. In other hand, the non linear force free extrapolation ($\alpha = \alpha(x, y)$) will return a configuration with more complexity for the magnetic field energy and, consequently, also a greater value of the magnetic energy.

Those concepts are more clearly seen using the helicity (H_{el}) of a field line, that can be mathematically described as:

$$H_{el} = \int_V \vec{A} \cdot \vec{B} dV \tag{3.38}$$

Being $\vec{A}$ the vector potential of the magnetic field. The helicity can be injected in a field line by means of the horizontal shear and vertical motions of the plasma.

The concept of helicity can also be used to further describe the force free parameter (α). Equation 3.24 implies that the magnetic field is directly proportional to its own helicity and the proportionality between them is the force free parameter.

The difference between the magnetic energy density calculated using the values of the magnetic field obtained through the potential and non linear force free methods can then be defined as the energy budget (U_{free}) of a given region.

$$U_{free} = U_{nlff} - U_{pot} \tag{3.39}$$

The ratio between U_{nlff} and U_{pot} is always positive.

The energy budget is the available energy to be released in flares or eruptive events. The works of Régnier et al. (2005), Schrijver et al. (2008) and Thalmann e Wiegelmann (2008) point that it is reasonable to assume that the energy budget necessary in order to occur flare releases is around $10^{25}J$ while in Régnier et al. (2002) it was found that an energy proportional to $10^{24}J$ was insufficient to trigger such events. For intense events, like a X-class flare, Metcalf et al. (2008) found that the necessary energy is around to $10^{26}J$.

Therefore, by continuously observing an active region, its energy dynamics can then be studied and the energy build up can be measured. The energy build up is then an important feature in the study of an active region evolution since it will estimate the amount of free energy that an AR can release eruptive processes. Monitoring the AR NOAA 10540 Thalmann e Wiegelmann (2008) found that the magnetic energy density not necessarily decreases after a flare however this result may be found due to the lack of temporal resolution available to study the AR energy budget.

The energy can be released by converting magnetic energy in other energy forms by means of the magnetic reconnection. The build up of the energy is also influenced by the helicity (H) injection within the AR.

3.4 Comparing the extrapolation results to the actual data

Whether or not a result can be considered reasonable depends on two things: the data must be consistent with the laws of physics and, more importantly, must match the observations.

For extrapolations this is also true although the observations can be used to perform tests and find an optimum value for the force free parameter. Since the latter can not be measured, like the magnetic field vector, initially setting a value for α relies on the experience of the user being no more than a guess. This process can be improved by comparing the shape of the extrapolation with the topology of the plasma loops that rise from the photosphere. Since their movement is bounded with the magnetic field lines, it can be considered an indirect form of seeing such lines. Then the force free parameter can be adjusted until a good match between the extrapolation and the data is found. The changes in the energy density can then be monitored once the magnetic field is obtained.

Also, the GOES(XRS-EUV) (BORNMANN et al., 1996) Ultra-Violet and X-ray fluxes can be used to compare the amount of energy that was released during a flare with the results obtained through calculations.

The problem regarding such methodology is that one shall trust that the non-linear force free is capable to properly extrapolate the magnetic field and, thus, retrieve the “correct” energy within the specified volume.

A discussion covering the validity of magnetic field extrapolations to study ARs can be found in Rosa et al. (2009) and a review of the magnetic field in the solar atmosphere is given by Wiegelmann et al. (2014).

4 Usage of Stokes profiles

4.1 Introduction

This section will present the results that were obtained through the usage of spectropolarimetric observations made by the Hinode SOT/SP mission in order to describe the major features associated with NOAA 12443 during the time in which the instrument was observing the region. Part of the results were presented at IAU 328 meeting in Maresias-SP (Brazil) and published as proceedings.

As discussed in chapter 2 the Stokes profiles can be used to infer some of the properties of the solar atmosphere. This chapter comprises the results obtained by mapping the solar surface with full Stokes data. A brief description of the computational tools used as a base for this study is presented at the appendix A.

4.2 Data processing

In order to study the solar surface it is often convenient to plot maps of the relevant physical parameters, e.g. magnetic field strength or flow velocity. Some of those maps can be extracted directly from the Stokes profiles without the need to use an Stokes inversion algorithm.

Taking for example HMI (SCHERRER et al., 2012) (PESNELL et al., 2012) and Hinode/SP instruments (KOSUGI et al., 2007) (TSUNETA et al., 2008), where the first is a full Stokes imager while the latter is a spectropolarimeter. HMI can take a full picture of the Sun every two seconds and Hinode need several minutes to cover a single region, the latter has a better spectral resolution.

One example of working using surface maps of the solar surface to study the behaviour of active regions is presented in González (2006).

Below we will give an introduction of the maps that were used on this work to study the solar surface produced with data from Hinode solar telescope. The codes, written in IDL, used to plot the maps can be requested to the author of this dissertation.

4.2.1 Continuum maps

Continuum maps are basically a map of the values of Stokes I over the observed region. They are particularly useful to identify structures such as ARs and bright points. An example of such map is represented in Figure 4.1.

Since the spectral line formation is proportional to the height in the photosphere, it is also possible to study the shape of the structures on different layers of the photosphere. Taking data from Hinode as an example, the first spectral pixel would correspond to the continuum, which is emitted mainly from the photosphere, while the line wings and core usually sample higher layers.

Figure 4.1 - Mapping the solar surface - continuum.

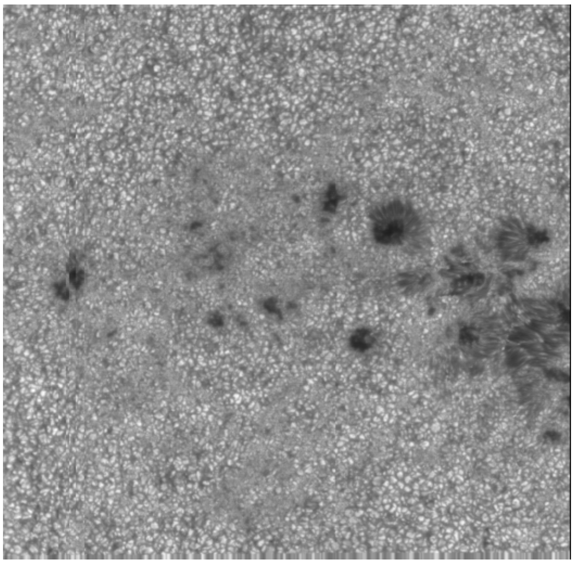

Continuum map of AR NOAA 12443 at the neutral iron lines (FeI) 6301.5107 Å.
SOURCE: Author's own work.

4.2.2 Linear polarization maps

The maps of linear polarization will highlight regions where the magnetic field is perpendicular to the LOS and, therefore, the linear polarization emission is more pronounced. Those maps are particularly useful to see the structure of the penumbra surrounding the AR, as can be seen on Figure 4.2.

The value of the degree of linear polarization for each pixel was calculated by:

$$L_{pol} = \sqrt{\left(\frac{U}{I_{cont}}\right)^2 + \left(\frac{Q}{I_{cont}}\right)^2} \tag{4.1}$$

Which is a sum of the Stokes parameters Q and U normalized by the continuum

Figure 4.2 - Mapping the solar surface - linear polarization.

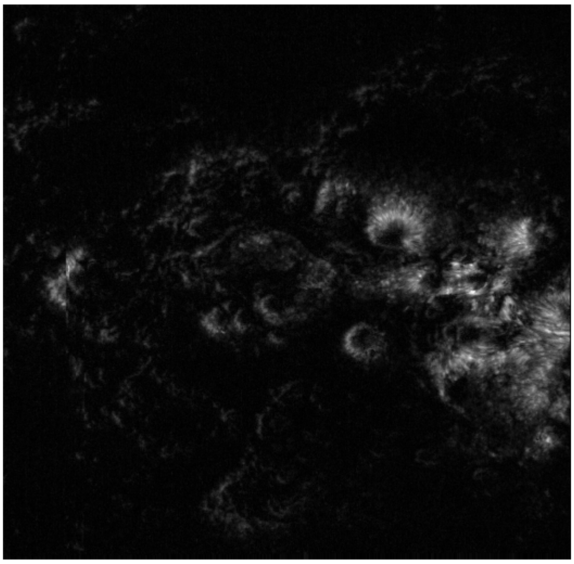

Linear polarization map of AR NOAA 12443 at the neutral iron lines (FeI) 6301.5107 Å.

SOURCE: Author's own work.

values of Stokes I for that pixel on the spectral line.

4.2.3 Weak Field Approximation

The Weak Field Approximation (WFA) can approximate the values of the magnetic field considering that the broadening on the wavelength caused by it ($\Delta\lambda_B$) is much smaller than the Doppler broadening ($\Delta\lambda_D$) as discussed by González (2006). WFA is valid if a line has a small or moderate effective Landé factor and the field is not strong enough to saturate the line separation. For the FeI 6301.5 Å the magnetic field should be less than 1000 Gauss.

The weak field approximation as presented, for example by Milić et al. (2017), can be calculated using the following expression:

$$V(\lambda) = -4.39 \times 10^{-13} \lambda^2 g B_{\parallel} \frac{dI}{d\lambda} \tag{4.2}$$

Since Stokes V is a characterization of the circularly polarized component of light, it will map the component of the magnetic field that is along the Line of Sight (LOS) which is a consequence of the Longitudinal Zeeman effect.

While it does not retrieve the magnetic field vector, the weak field approximation is useful to study the magnitude of the magnetic field along the LOS and also unveil magnetic structures that might be difficult to spot at the continuum map as shown in Figure 4.3.

Figure 4.3 - Mapping the solar surface - weak field approximation.

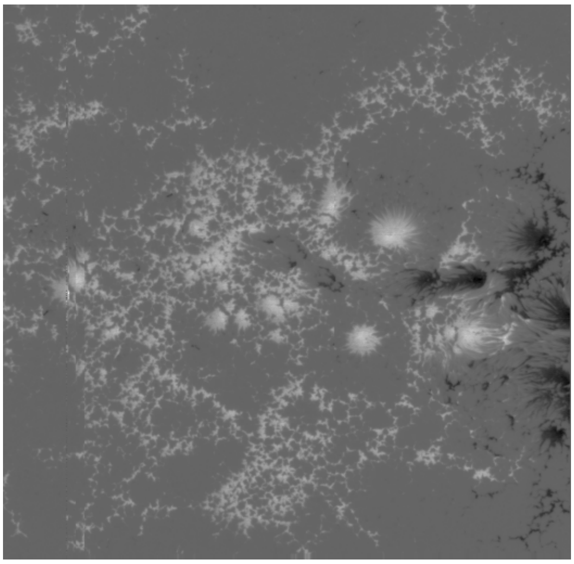

Weak field approximation map of AR NOAA 12443 at 6301.5107 Å.
SOURCE: Author's own work.

4.2.4 Dopplergrams

Since the solar plasma is not static, it is expected that the wavelengths measured by Hinode will be somehow shifted because of the plasma's motion which will result in a dopplershift:

$$v_{los} = \frac{c\Delta\lambda_D}{\lambda_0} \tag{4.3}$$

Where λ_0 is the reference wavelength. The zigzag pattern in Figure 2.4 representation of Stokes I is a clear example of Doppler effect on the measurements. Therefore, taking the line shifts allows to map the velocities parallel to the LOS as presented in Figure 4.4. The difference arises from the slight asymmetries on Stokes I profiles on the minimum points of intensity of the Stokes I profile, in this case for neutral iron lines (FeI). Typical values found reach up to 2 km s^{-1} for both downflows and upflows.

Figure 4.4 - Mapping the solar surface - dopplergrams.

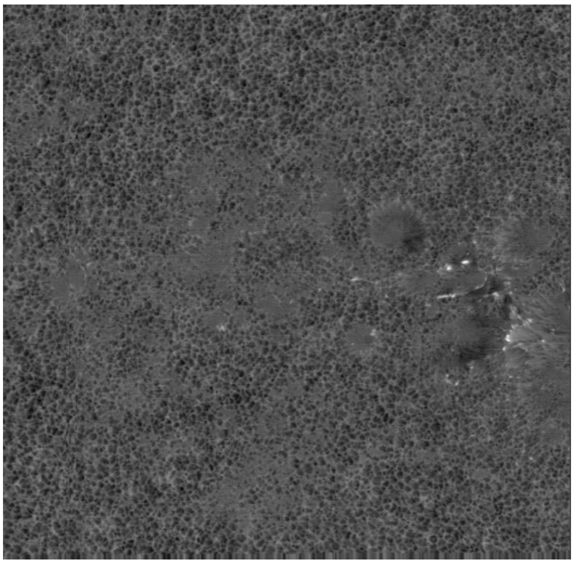

Dopplergram of AR NOAA 12443 at 6301.5107 Å. Downflows are in white color and upflows are in black color.

SOURCE: Author's own work.

There are two methods to estimate the dopplershift; computing the spectral line minimum; computing the center-of-gravity (COG) of the line. The COG wavelength of a profile I is defined as the centroid of its residual intensity profile (UITENBROEK, 2003):

$$\lambda_{COG} = \frac{\int \lambda(I_{cont} - I)d\lambda}{\int (I_{cont} - I)d\lambda} \tag{4.4}$$

Where the subtraction $I_{cont} - I$ is the residual of the Stokes I profile. Therefore, the velocity along the line of sight can be calculated using the following expression:

$$v_{los} = -\frac{c(\lambda_{COG} - \lambda_0)}{\lambda_0} \tag{4.5}$$

The overlap of some of those maps is also interesting to observe since it is possible to see, for example, in what type of structure is located a strong flow, as shown in Figure 4.5.

Figure 4.5 - Superposing maps.

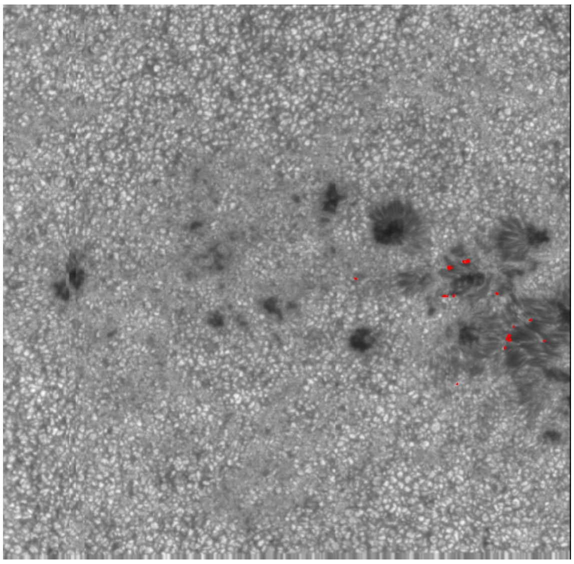

Here the most intense flows found in Figure 4.4 are superposed in Figure 4.1. Where considered, for this mask, that a velocity must be greater than 4km s^{-1} to be marked.

SOURCE: Author's own work.

4.2.5 Stokes V asymmetries

Each pixel on a map has its own set of Stokes profiles associated to it, therefore, the parameters for each pixel can be individually assessed. Asymmetries on a Stokes V profile are an indicative of velocity and field gradients (SOLANKI, 2013). Those asymmetries can be calculated by integrating a pair of lobes of a Stokes V profile, which are called red and blue lobes, e.g Morinaga et al. (2007). The difference between the area of the lobes is the asymmetry:

$$A_{sy} = \int V d\lambda = \int V_{red} d\lambda - \int V_{blue} d\lambda \tag{4.6}$$

Therefore, the asymmetries of the map exhibited in Figure 4.3 can be studied with an histogram of the values obtained by integrating the normalized Stokes V profile, degree of circular polarization, of each pixel providing then an insight on the presence of velocity and magnetic field gradient on NOAA 12443.

4.3 Results

The continuum map, displayed in Figure 4.6, shows that the AR NOAA 12443 has quite a complex structure with a diversity of polarities being most of those almost fully surrounded by a penumbral structure that can be seen in Figure 4.7. Along the observed time it is possible to notice that the overall structure is far from being static, indicating that new magnetic flux was emerging on NOAA 12443.

Figure 4.6 - Continuum mapping.

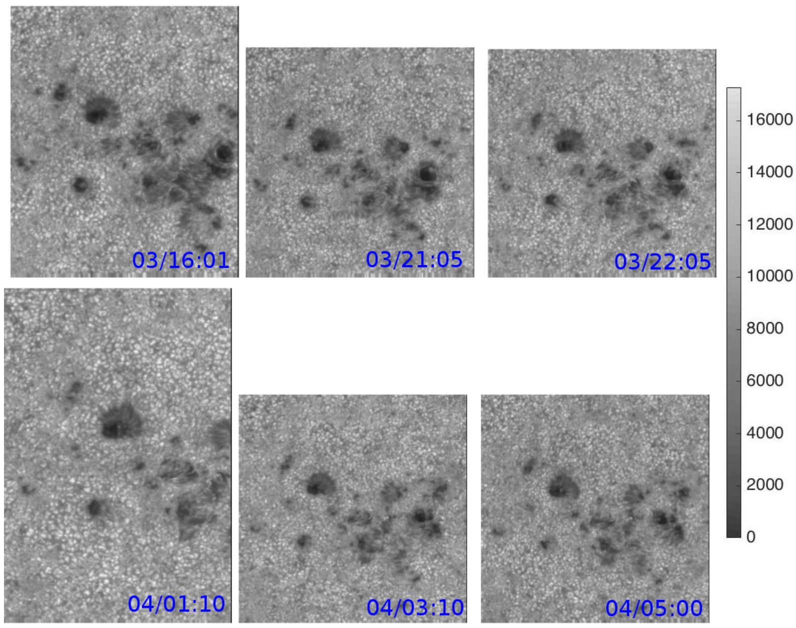

This set of images show the continuum maps of NOAA 12443 at 6301.5107 Å.
SOURCE: Author's own work.

The weak field approximation mapping of the AR NOAA 12443 reveals that the region has several spots whose polarities can be considered to be separated, as shown in Figure 4.8. However, it is important to bear in mind that the fine structure of NOAA 12443 shown on Figure 4.8 is on the limits of what the weak field approximation can reveal. It is, however, possible to see that the spots are moving in relation to one another and changing in shape which can be considering evidence that the

Figure 4.7 - Linear polarization mapping.

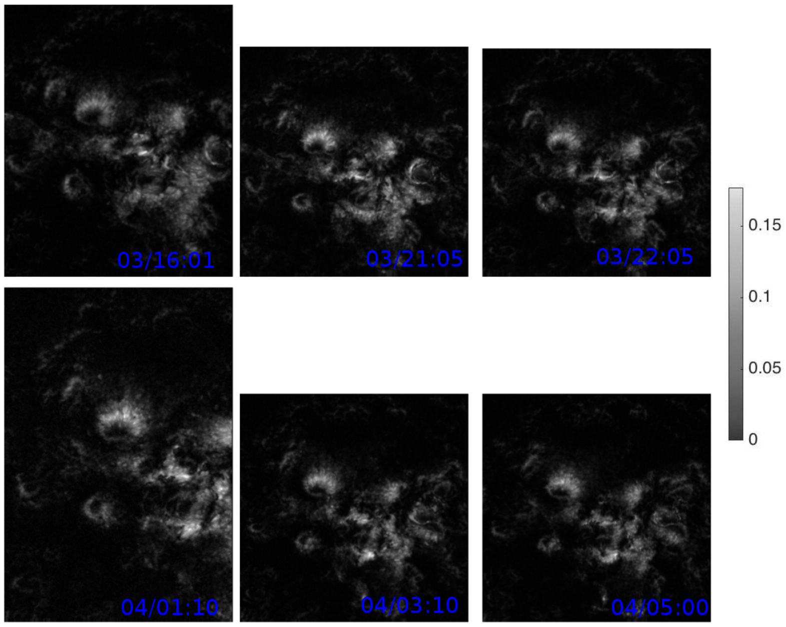

This set of images show the linear polarization maps of NOAA 12443 at 6301.5107 Å.

SOURCE: Author's own work.

topology of the overlying field is changing and the AR is getting prone to give rise to energetic events (LONGCOPE, 2005).

Furthermore, Figure 4.8 shows an extensive facular region surrounding the spots, which is not so evident on the continuum maps displayed in Figure 4.6.

The dopplergrams, displayed in figure 4.9, shows the patterns of the plasma convection movement over the maps. It is more useful, however, to identify the points where the velocity is more intense and overplot those results in another map, such as the continuum map, that will allow the identification of the structure upon where those flows are located.

A superposition of the LOS velocity most intense values, considering any flow above 4 kms^{-1}, in the continuum map led to the results displayed in figure 4.10. It is interesting to note that the entirety of the red dots, that mark the location of the regions with an intense flux, are located within the penumbral structure of the AR. Furthermore, all the points corresponds to downflows which means that in none of the dopplergrams any upflows speed reached 4 kms^{-1}.

Figure 4.8 - Weak Field Approximation mapping.

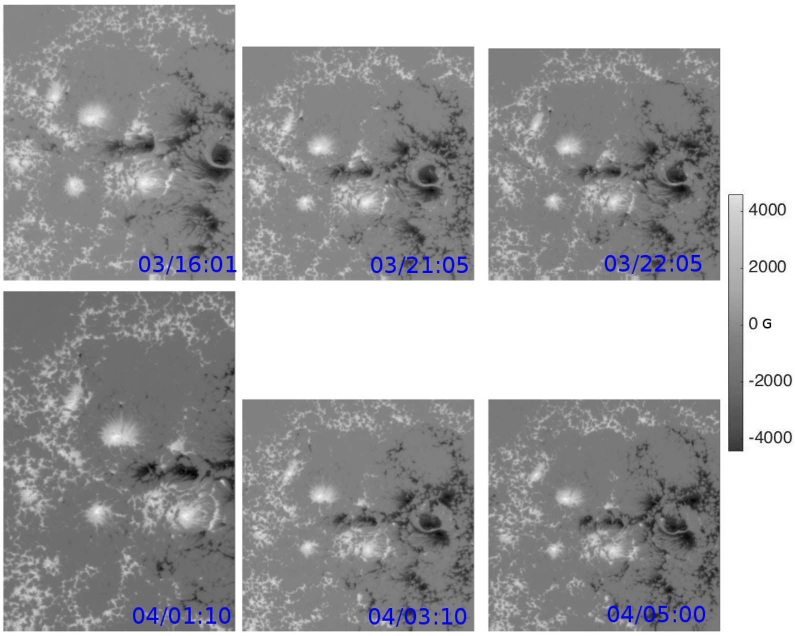

This set of images show the weak field approximation mapping of NOAA 12443 at 6301.5107 Å.

SOURCE: Author's own work.

The fact that the entirety of the points marking the regions whose speed flow is more intense may be linked to the Evershed effect, as discussed for example by Franz (2011), which accounts for the plasma motion on the photosphere and is studied using the Doppler displacement of the wavelengths and studies the radial outflow of the plasma from a sunspot. Since the field direction in the umbral region is close to being vertical and the plasma movement will follow the field lines the presence of intense downflows on the surroundings of the umbra would compensate the matter outcome of the plasma following the umbral field lines. The measured flows are along the LOS and, therefore, we are not accounting for radial flows.

The Stokes V asymmetries histogram, Figure 4.11, indicates that there are different levels of velocity and field gradients within NOAA 12443 area. The fact that the histogram peaks close to zero indicates that the presence of velocity and field gradients are localized phenomena within the AR and not a general property of the whole structure.

Figure 4.9 - Dopplergrams.

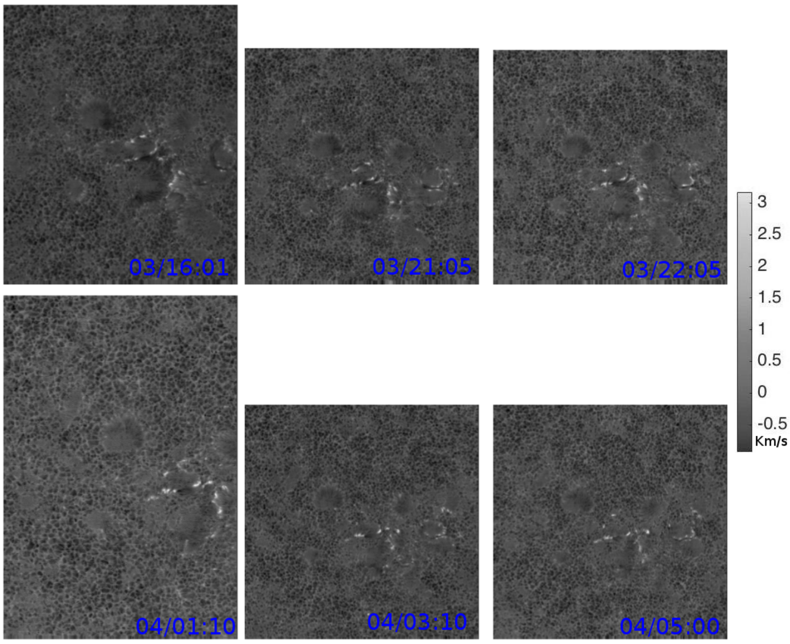

This set of images show the dopplergrams of NOAA 12443 calculated using the Center of Gravity method at 6301.5107 Å.

SOURCE: Author's own work.

4.4 Discussion

The production of solar surface maps was set as the first objective of this work since it represented an opportunity to study the AR structure and define how to reach the other objectives. In this sense the results where particularly meaningful since they allowed an overview of the complex structure related to NOAA 12443.

It is possible to see that NOAA 12443 has some umbral dots and a complex penumbral structure that is far more complex than a simple region which comprises of a unique umbra region fully surrounded by a penumbra. Therefore, the study of NOAA 12443 proved to be quite challenging not only in terms of achieving a physical description of its evolution but also in terms of computation.

The positions where the intense downflows were identified are probably regions of penumbral development. It can be seen in Figure 4.10 and all the other maps that were produced that the downflows appeared within or at the border of the penumbra region probably due to the penumbra development and the boundary of the Evershed effect. Checking the values of the LOS magnetic field on those points gave values

Figure 4.10 - Continuum superpositions.

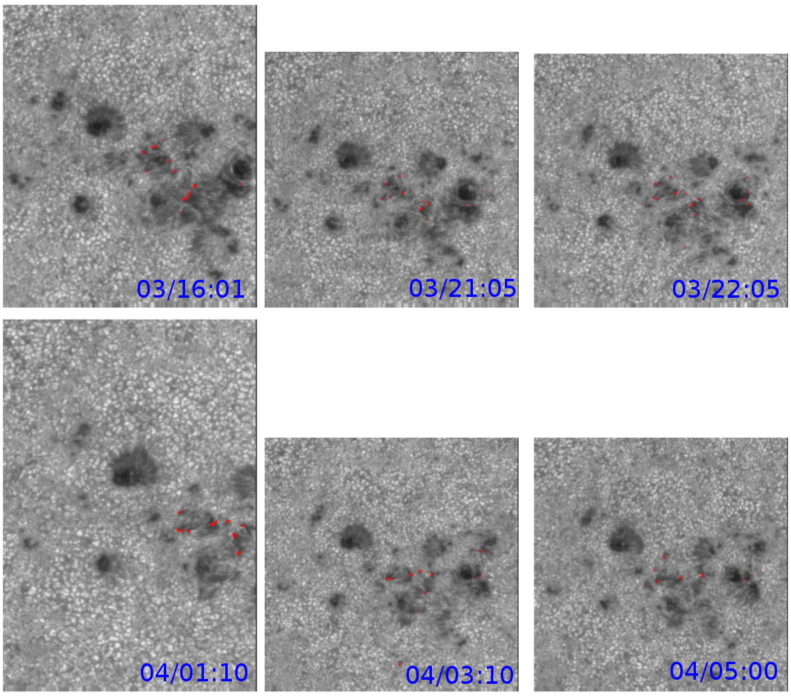

This set of images show the continuum mapping of NOAA 12443 at 6301.5107 Å marked with red points that indicates regions with downflows above 4 kms^{-1}.

SOURCE: Author's own work.

usually between +1 kG and -1 kG.

The histogram has a peak at zero, where Stokes V can be considered symmetric, however, there are plenty of values for different levels of asymmetry which is consistent with the broad range of activities displayed by NOAA 12443 over the course of its passage through the disk.

Also, the asymmetry results can later be used to identify regions according to their asymmetry level, similarly to what have been done to identify the intense fluxes over the continuum map. This is, however, out of the scope of this work.

In order to advance the results obtained with polarimetry it is necessary to employ refined Stokes Inversion algorithms which will also accounts for the effects of the atmosphere. This was, however, beyond the hardware and time budgets of available.

Figure 4.11 - Stokes V asymmetries.

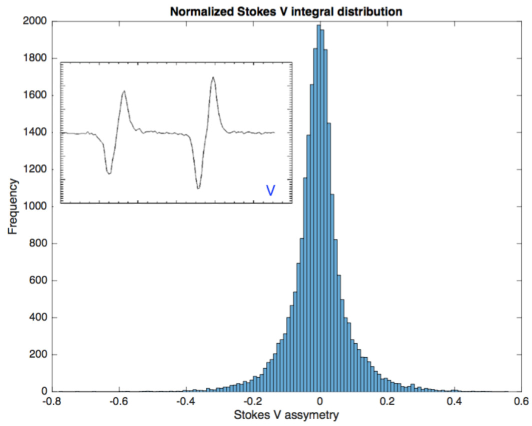

Histogram of the asymmetries of each pixel on the map exhibited on Figure 4.3 computed by integrating the first Stokes lobes area difference of the normalized Stokes V curve.

SOURCE: Author's own work.

4.5 Conclusion

The objective of this chapter was to use measurements of the Stokes parameters to draw maps of the the AR NOAA 12443 at photospheric level.

Each map presented has a different set of properties and utilities to study the AR's structure. Therefore the results allowed us to have an overview of the changes that were happening within the AR at photospheric level.

It is remarkable to see the variety of features displayed by NOAA 12443 such as: the numerous magnetic poles, a full penumbral structure, some facula regions around the AR, and a light bridge. This set of features is only seen in complex ARs.

In this chapter the results of the first and second specific objectives, being those to produce solar surface maps and velocity fields of NOAA 12443, were presented and thus successfully accomplished.

5 Energetic evolution results

5.1 Introduction

This section will present the results that were obtained through the usage of magnetic field extrapolations and also other complementary analysis using data from HMI, AIA and GOES in order to describe the events related to NOAA 12443 on November 4th of 2015. A brief description of the computational tools used as a base for this study is also presented at the appendix A.

5.2 Methodology

As discussed in chapter 3, an extrapolation procedure tries to reconstruct the field topology in three dimensions based on the measurements that are taken over the solar surface using a combination of spectropolarimetry techniques and Zeeman effect.

Using a combination of potential and linear force free extrapolations, in this chapter we present how the magnetic field of the AR NOAA 12443 evolved in time close to the major flares associated with this region as shown in Figure 5.1. The SWPC scaling factors were removed, as indicated in the instrument guide, so that those plots already corresponds to the corrected values.

Considering that a linear force free extrapolation is less capable of retrieving most of the field complexity when compared to a non-linear force free extrapolation the results obtained by this approach are to be seen as the gross picture of the field evolution. However, even being a more simplistic approach, it is still possible to estimate the energy budget associated with the AR since the linear force free extrapolation still take into account the presence of electric currents. LFF extrapolations are somehow unrealistic since the force free parameter (α) is considered a constant for all points in the space. Therefore, recalling that the energy is also influenced by the field helicity, one might expect that the magnetic field extrapolated will present more energy associated to the extrapolated field when compared to the potential extrapolation where the force free parameter is zero for all points in space Wiegelmann et al. (2014).

The field lines of the solar Corona can be indirectly seen using instruments such as the Atmospheric Imaging Assembly (AIA) (LEMEN et al., 2012) aboard of the Solar Dynamics Observatory (SDO) (PESNELL et al., 2012) as shown in figure 5.2. It is, nonetheless, important to remember that field lines are nothing more than a

Figure 5.1 - GOES X-ray flux.

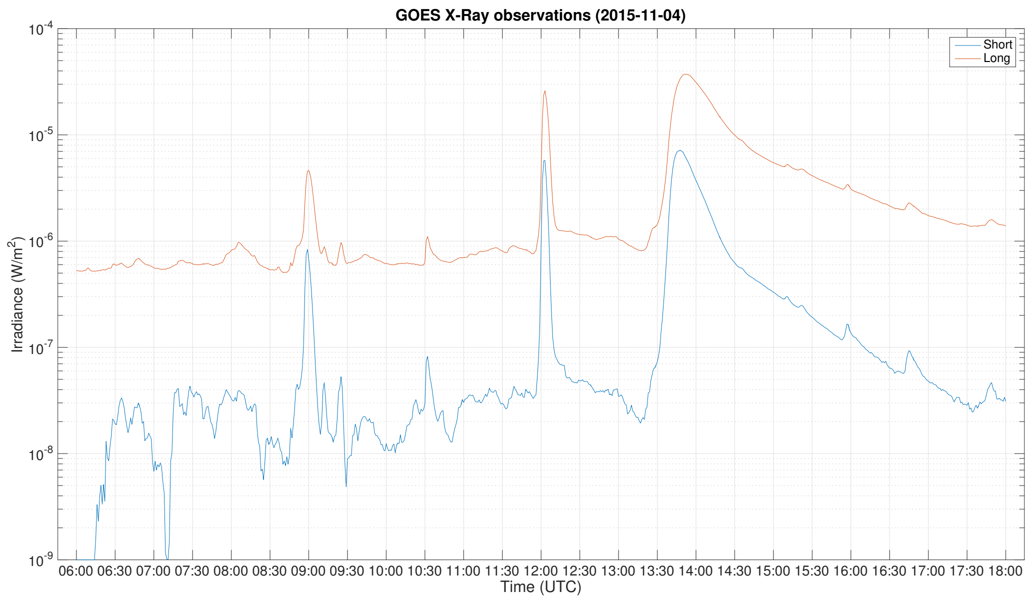

Irradiance measured by GOES from 06:00 to 18:00h (UTC) of 2015-11-04. Both long ($1 - 8$Å) and short ($0.5 - 4$Å) channels of the instrument are displayed. Each point corresponds to the average of the detected flux during one minute.

SOURCE: Author own work.

mathematical tool to represent the hypothetical action of the forces that "spawn" such fields.

Some studies, such as Gary et al. (2014), use images from AIA to find an optimum value for the force free parameter and also check how good the algorithms could reproduce the field lines. Rosa et al. (2009) points that there is evidence among the various scientific works using the NLFF model that the reproduced field lines are in good alignment with the observed features however the algorithms does not necessarily reproduce the observations. In this study the HMI values for the force free parameter were used as entries for the algorithm along with the data from the active region.

The algorithm used to extrapolate the magnetic field was the "optimization_fff" which is a routine of the NLFFF package of Solarsoft. There were used two of the options for potential and linear force free extrapolations using the vector magnetic

Figure 5.2 - AIA NOAA 12443 flare.

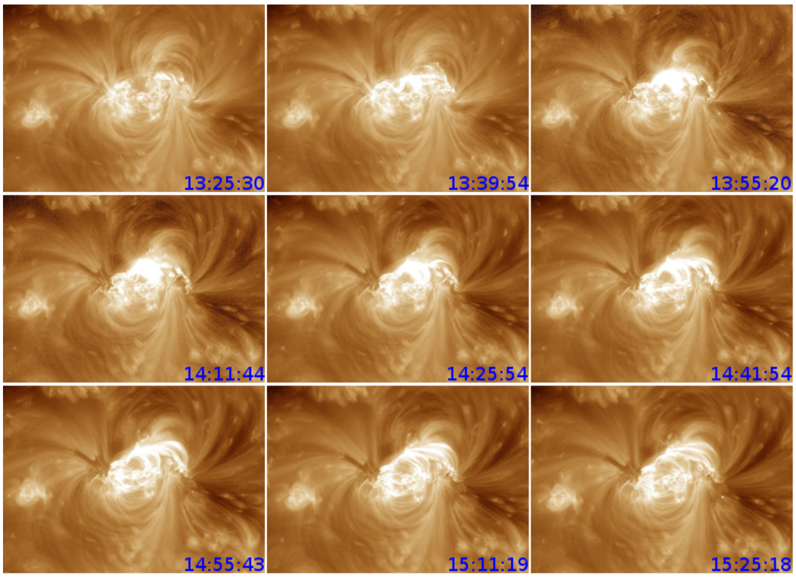

AIA images of AR NOAA 12443 from 13:25:30 to 15:25:18UT (2015-11-04) covering the time where the last X-ray flux peak was registered by GOES. The sudden brightening of the region which is a remarkable visible characteristic of a solar flare can clearly be noticed on those images.

SOURCE: Author own work.

field data from HMI as a boundary condition. The optimization method used by this algorithm was developed by Wheatland et al. (2000) and consists in minimizing an functional L using a evolutionary procedure:

$$L = \int_V B^{-2} \mid (\nabla \times \vec{B}) \times \vec{B} \mid^2 + \mid \nabla \cdot \vec{B} \mid^2 dV \tag{5.1}$$

Where $B(\vec{r})$ is a vector field defined in a volume V. In order for the left hand side of Equation 5.1 reaches zero, the divergence of the magnetic field must be zero, which is expected from the Gauss's law for magnetism, and the field must be force free that is equivalent to say that:

$$\mid (\nabla \times \vec{B}) \times \vec{B} \mid^2 = 0 \tag{5.2}$$

The only other possible solution would be the trivial solution, where the magnetic field itself is zero.

The following sections will present the study of the AR NOAA 12443 evolution using the magnetic field extrapolations results along with analysis made using some HMI data products and data from GOES and AIA.

5.3 Data processing

In order to provide the boundary conditions for the optimization routine the HMI vector magnetic field data was downloaded and organized according to their date of observation. Therefore each file that would be used for a magnetic field extrapolation have the measurements of the Spaceweather HMI Active Region Patch (SHARP) for the AR NOAA 12443.

Complementary, data from GOES X-ray flux, both on long (1 - 8Å) and short (0.5 - 4Å) channels, and AIA on wavelengths 131Å, 171Å, 193Å, 211Å and 335Å were used to plot the emission curves. While data from GOES need only to be corrected by a numerical factor, AIA data needs to undergo through its standard reduction routines available as a package of SSW/IDL. Furthermore, the AIA data was processed to display the individual emission curves of both ARs NOAA 12443 and 12445 so the behaviour of each AR can be compared to the GOES X-ray flux.

In order to cover the three times in which the X-ray emission peaked it was used the available data from 06:00 UT to 18:00 UT with a twelve minutes interval from each file using then all the instrument temporal cadence.

The spatial sampling of the image was defined by the AR SHARP window which varies in size as the active region moves on the solar disk however, for a time interval of a few hours, those changes does not introduce an error that would compromise the results. For the used data sets the maximum variation on both sides of the window was close to 3% of its own size while the AR was passing throughout the disk. The data was also reduced to the double of its spatial sampling to suit the available hardware capabilities.

The data was then processed using the optimization routine and the extrapolated field was obtained using the potential and linear force free configurations allowing the study of the AR NOAA 12443 energy evolution by integrating the field over the volume.

The HMI SHARPs also hold significant information of an AR other than the necessary to perform a field extrapolation. Therefore, readings of such the electric current and field helicity calculated by the HMI pipeline were also used in order to explore how those parameters evolved. Those quantities can be accessed at the headers of the SHARPs and are products of the HMI pipeline.

5.4 Results

In order to discuss the results it is important first to state how the relevant structures for this study were distributed on the solar atmosphere. Figure 5.3 highlights the structures that take part on the discussion which are: 1 - NOAA 12443, 2 - NOAA 12446 and 12441, 3 - NOAA 12445 and 4 - a coronal hole.

Figure 5.3 - Major structures in the solar disk during the studied time.

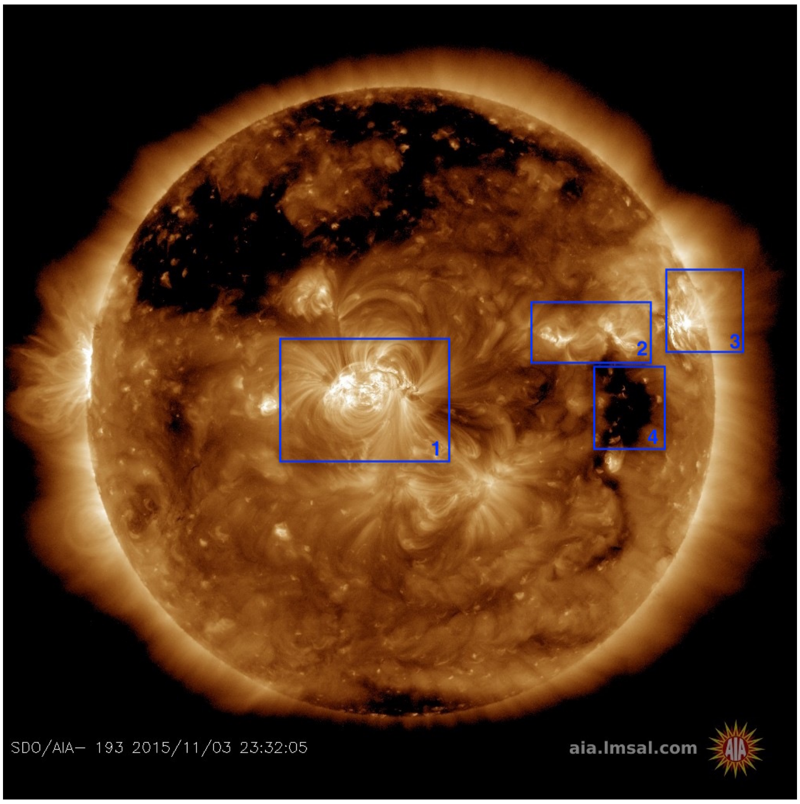

Image of AIA 193 AÅ channel taken at 2015/11/03 23:32 UT. The windows embrace the structures: 1 - NOAA 12443, 2 - NOAA 12446 and 12441, 3 - NOAA 12445 and 4 - a coronal hole.

SOURCE: AIA LMSAL aia.lmsal.com - adapted by the author.

The X-ray flux measured by GOES on 2015-11-04 from 06:00 to 18:00 UT displays three peaks which characterize a C-class flare and two M-class flares. The AIA AR temporal intensity sequence was integrated and repositioned on every step so that the same region could be consistently integrated. Also, each pixel was normalized by the exposure time that the instrument took to capture the image. Using AIA intensity sequences of the ARs it can be seen that the two first flares came from NOAA 12445 and the last one from NOAA 12443. Those results are displayed in Figure 5.4.

Figure 5.4 - Results from AIA and GOES.

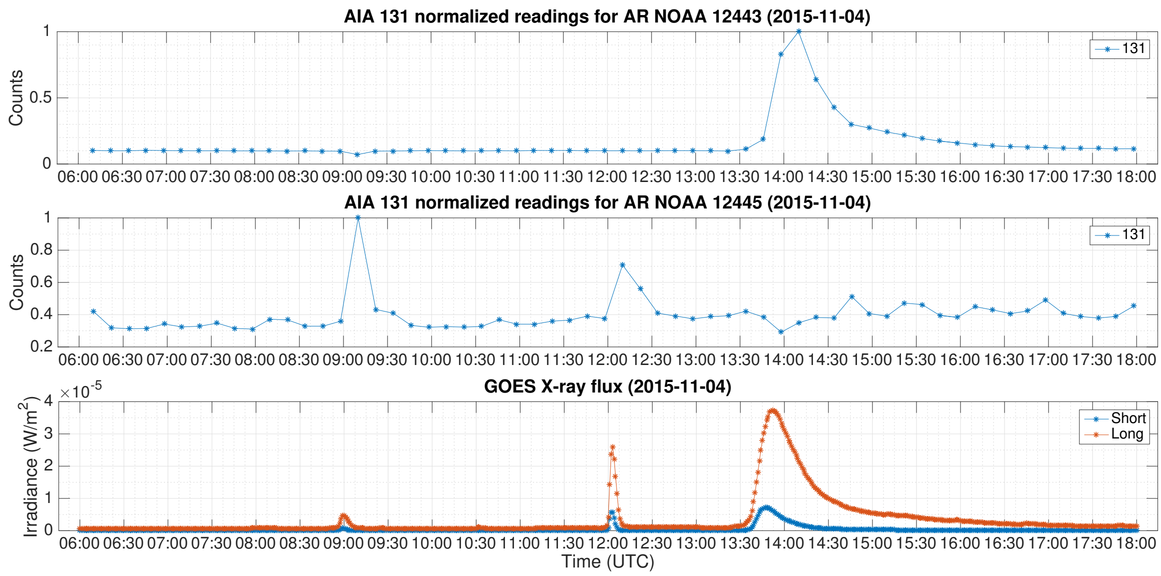

Top: AIA counts on the wavelengths 131Å for the AR NOAA 12443. Mid: AIA counts on the wavelengths 131Å for the AR NOAA 12445. Bottom: X-ray flux measured by GOES. All the data are displayed from 06:00 to 18:00h (UT) of 2015-11-04.

SOURCE: Author's own work.

As said before, there is some useful information on the HMI products headers whose behaviours are displayed, for NOAA 12443 along the studied time, on Figures 5.5 and 5.6. Only the events that are definitively associated with NOAA 12443 are highlighted by the dashed lines being the red line representing the M-class flare that started 13:30 UT, according to the GOES X-ray flux measurements, and the black line representing a Halo type CME at 14:48 UT, according to the CDAW catalog, that arose from NOAA 12443.

On Figure 5.5 the values of the mean twist of the field lines of NOAA 12443 shows a continuing decrease from 12h up to NOAA 12443 flare time however, the values increase after the event and display a rather small correspondence with the CME. The absolute current helicity presents a significant decrease after flare and almost no change after the CME. On the other hand, the values for the mean gradient of the horizontal field displayed shy changes for both flare and CME.

Figure 5.5 - Parameters measured by HMI.

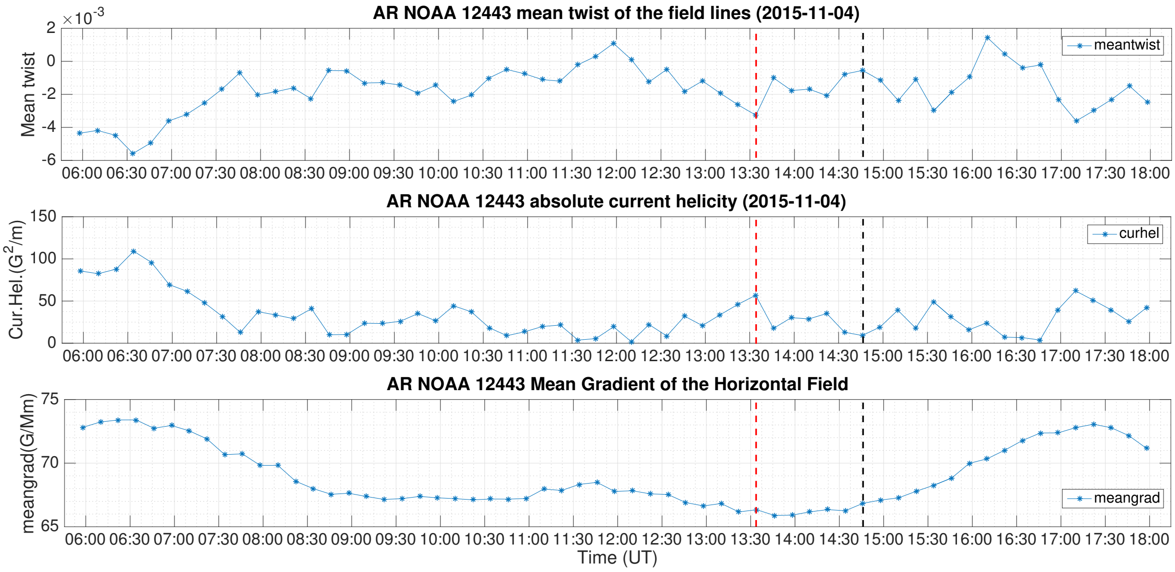

Top: mean twist of the magnetic field lines. Mid: absolute Value of the Net Vertical Current Helicity. Bottom: mean horizontal gradient of the horizontal field calculated by the HMI pipeline. The red dashed line represent the approximated time in which the GOES flux started to increase for the third flare while the black dashed line corresponds to the approximated time of the halo CME records of the CDAW catalog (`https://cdaw.gsfc.nasa.gov/CME_list/`).

SOURCE: Author's own work.

On Figure 5.6 the top panel shows that the total unsigned vertical current presents a small increase followed by sharp drop just after the beginning of NOAA 12443 flare. During the CME there is also a small drop on the total unsigned vertical current values. The relationship of the AR NOAA 12443 evolution and its flare and

CME is more clear if the behaviour of the vertical current is observed, which can be observed in the middle panel of Figure 5.6. Similarly, the total unsigned vertical current helicity, bottom panel of Figure 5.6, presents a small increase followed by a sharp fall.

Figure 5.6 - Parameters measured by HMI 2.

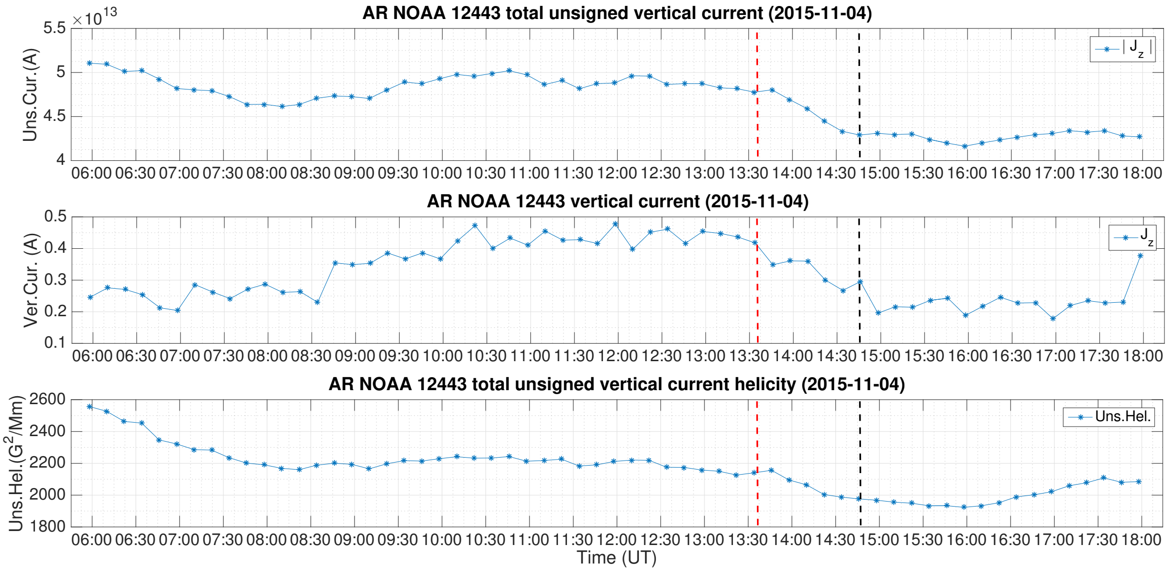

Top: Total unsigned vertical current. Mid: vertical current. Bottom: total unsigned vertical current helicity. Those values were calculated by the HMI pipeline. The red dashed line represent the approximated time in which the GOES readings started to climb for the third flare while the black dashed line corresponds to the approximated time of the halo CME records of the CDAW catalog.

SOURCE: Author own work.

Since the vertical currents displayed a strong relationship to the flare activity their measurements were studied over a larger period of time. In order to study the measurements of the total unsigned vertical current over the time in which NOAA 12443 was on the disk, those values were averaged per each 1200 minutes (20 hours), which corresponds to a hundred measurements from HMI. The results in Figure 5.7, shows that NOAA 12443 presents a sharp decrease of its vertical currents prior to the beginning of the flare and some hours later the fall ceased until November 7th where again a sharp decrease was noticed.

Figure 5.7 - NOAA 12443 Total Unsigned Vertical Current.

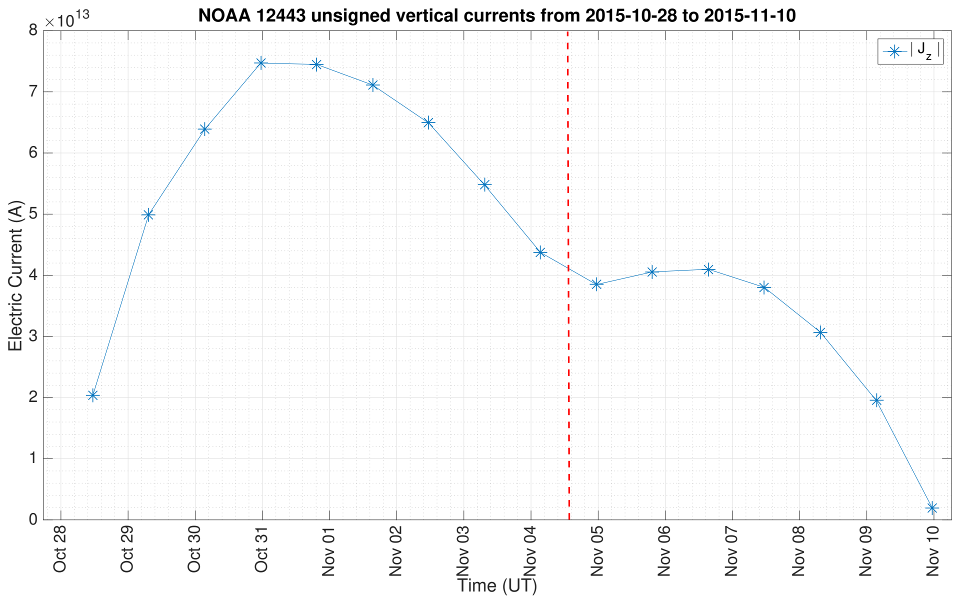

Averaged total unsigned vertical current. The values were averaged for each 1200 minutes which corresponds to 100 measurements from HMI. The red bar represents the approximate time in which NOAA 12443 flare started.

SOURCE: Author own work.

In order to check the functioning of the NLFFF package some tests were carried out before the extrapolations were calculated. First, the relationship between the energy recovered and the value of the force free parameter used by the algorithm were tested. These results are displayed on the top panel of Figure 5.8 and, as it can be noticed, the values of energy recovered are satisfactory ranging between 10^{25} to 10^{27} Joules. The NLFF/SSW routine was then tested for a single value of the force-free parameter (α) for all the studied time interval in order to check whether the assumption that the initial conditions of the algorithm would retrieve reasonable results for the energy associated with the magnetic field that would later be used to calculate the energy. As expected, the energy was directly proportional to the values of the force free parameter with the energy curves displaying essentially the same behaviour but dislocated over the y-axis as it can be seen in the bottom panel of Figure 5.8. The energy obtained with α set to 0.002 is already close to the results obtained with a potential field which is why the curves are overlapping themselves.Those results provide a good indicative that the algorithm is working properly.

Figure 5.8 - The force free parameter as an entry for optimization.

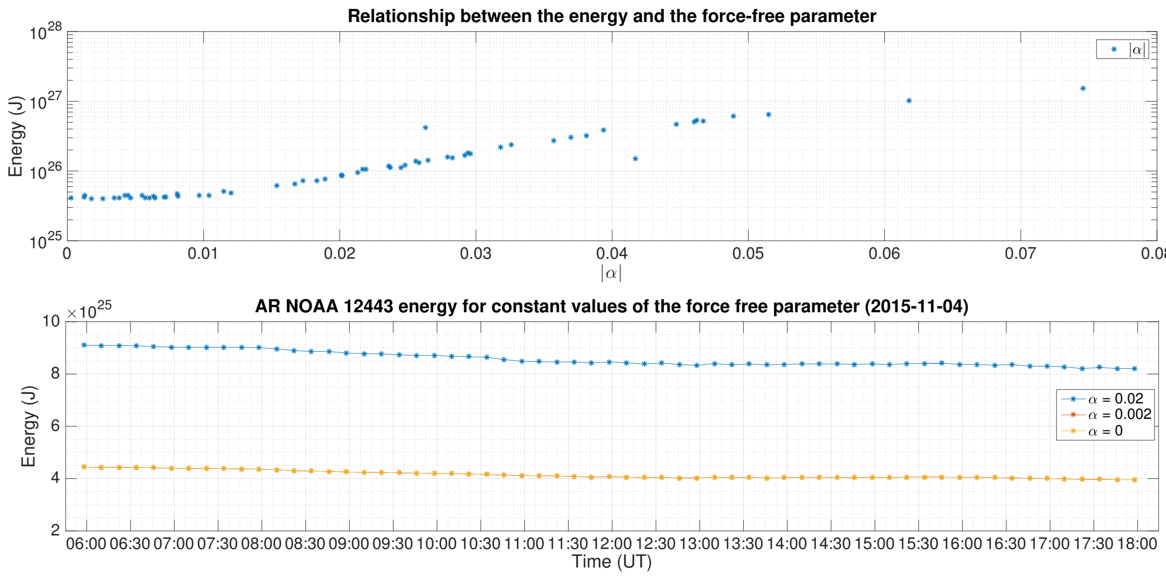

Top: comparison between the value of alpha used as entry and the energy obtained using the optimization routine. Bottom: energy obtained for all the data series using the same entry for every fit. It can be noticed that the energy values obtained with the entries $\alpha = 0$ and $\alpha = 0.002$ are already too close to be distinguished in this plot.

SOURCE: Author own work.

Since complementary data from HMI products is being used on this study, the force-free parameter was manually inserted following the headers of the fits files. The values used, the absolute values of α calculated by HMI, are displayed in Figure 5.9. The estimated potential energy from HMI SHARPS are displayed in Figure 5.10. The energy recovered with the linear force free magnetic field extrapolation ise displayed in Figure 5.11. The difference between those values $(E_{lff} - E_{pfss})$ is displayed in Figure 5.12 the bottom panel.

The values of the linear force free extrapolation remained, for the entirety of the studied time, significantly bigger than the values estimated by HMI for the AR's potential energy. Therefore a difference between the the values encountered by those two approaches will essentially be close to the values obtained using the linear ex-

Figure 5.9 - HMI estimatimative of the force free parameter.

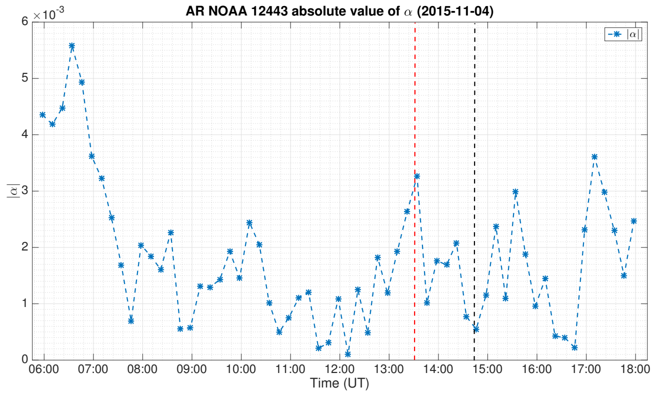

Absolute value of the force free parameter measured by HMI. The red dashed line represent the approximated time in which the GOES readings started to climb for the third flare while the black dashed lines corresponds to the approximated time of the halo CME entries of the CDAW catalog.

SOURCE: Author's own work.

trapolation. Yet, the energy build up and release around the flare time was rather shy.

There was, however, a significant change in the behaviour shown by the linear force free extrapolation if compared to the potential extrapolation. Prior to the flare the values obtained by both approaches were falling but the results of the linear approach got stable while the potential values kept dropping. Then, a couple of hours after the flare, the values represented by both curves once again started to fall.

In order to reduce the oscillation of the energy values to study the trend of the energy budget an average per hour was calculated (Figure 5.13). It can be notice that the energy curve shows three distinct behaviours before, during and after the flare. Those results are evidenced using linear adjusts as displayed in Figure 5.14.

5.5 Discussion

The changes in energy recovered through the data extrapolations where capable of matching the data provided by GOES showing that the results are successfully recovering part of the physics of the problem. However, the amount of these changes is highly uncertain using a linear-force free approach.

Figure 5.10 - Energetic evolution results using the potential approach.

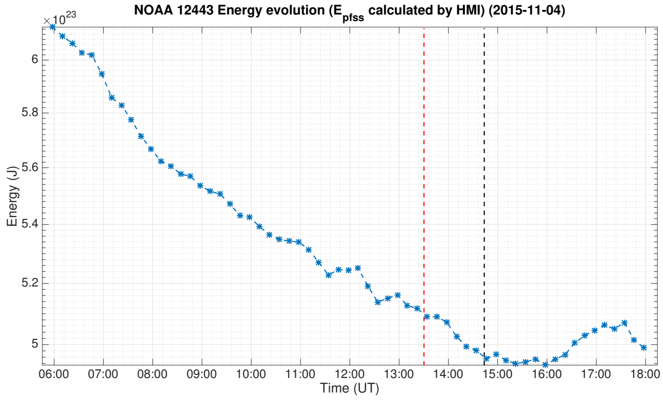

Energy values obtained by integrating the results of the magnetic field obtained using the potential field approach. The red dashed line represent the approximated time in which the GOES readings started to climb for the third flare while the black dashed lines corresponds to the approximated time of the halo CME entries of the CDAW catalog.

SOURCE: Author's own work.

Comparing the extrapolation results with AIA videos covering the studied time[1] it can be seen that before the flare starts diferent levels of activities could be seen within NOAA 12443, e.g. nanoflares and reconnections, which is consistent with the energy drop. The flare brought changes on the magnetic field topology that started a high level of activity around the area where the reconnection took place and then close to 17:00 UT the energy once again started to drop.

The information stored at the HMI SHARPS also provided to reach some agreement with the flare and CME related to NOAA 12443.

Even considering that the results obtained can not deeply account for the change in the physical parameters of the Active Region, the results can still construct the gross picture by estimating the behaviour of significant parameters, such as the helicity and energy. In the other hand, this work can be reproduced using a small computational budget, a relatively short time, the routines are available through solarsoft that can be download for free at any time, and also the data can be downloaded using JSOC data center.

It is important to bear in mind, as pointed by Wiegelmann et al. (2014), that even

[1]Some of those videos are annexed as suplementary materials.

Figure 5.11 - Energetic evolution results using the linear force free approach.

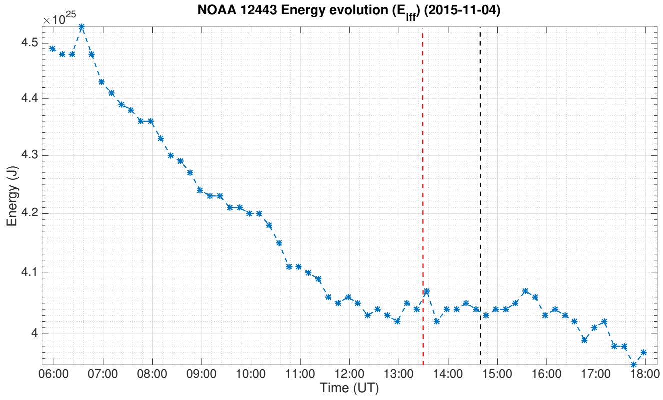

Energy values obtained by integrating the results of the magnetic field obtained using the linear force free field approach. The red dashed line represent the approximated time in which the GOES readings started to climb for the third flare while the black dashed lines corresponds to the approximated time of the halo CME entries of the CDAW catalog.

SOURCE: Author's own work.

using robust NLFF algorithms the correspondence between energetic events and the drop in the AR free energy can be tricky. In some of the examples mentioned by the author, for instance He et al. (2014) and Jing et al. (2009), it can be noticed that the free energy does not necessarily drops immediately after the flare starting showing that this sort of analysis has yet to improve.

5.6 Conclusion

The objective of this chapter was to obtain, using the the potential and linear magnetic field extrapolations, the magnetic field vector associated to the active region and then use those values to estimate the energy changes of NOAA 12443 around the time that the solar flare associated with this region took place which is approximately 13:30 UT according to GOES X-ray flux readings.

The HMI SHARPs carry a series of measurements and estimates which are calculated over the cutout of the solar disk in which comprises the AR. The contribution of those measurements, that can be directly accessed through the headers of a fit file, were particularly meaningful to compare the role of different quantities during NOAA 12443 evolution. Among the quantities studied, the vertical currents had the largest

Figure 5.12 - NOAA 12443 energy budget.

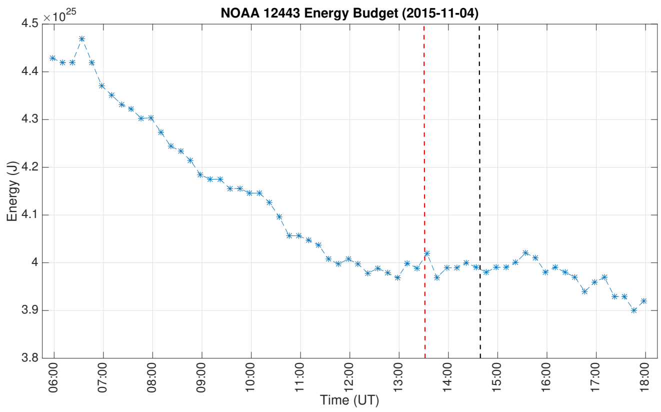

Energy budget ($E_{lff} - E_{pfss}$). The red dashed line represent the approximated time in which the GOES readings started to climb for the third flare while the black dashed lines corresponds to the approximated time of the halo CME entries of the CDAW catalog.

SOURCE: Author's own work.

response to the flare while, in comparison, the mean gradient of the horizontal field did not suffered a significant change around the flare time.

The algorithm used for this work offered a result which is consistent with the observations. The energy changes calculated with the extrapolated field seems to be aligned with what can be observed with movies from different channels of AIA where a high level of activity can be noticed before the flare: nanoflares and magnetic field reconnections on the inner loops, and that the loop which reconnection gave rise to the M-class flare remained active for several hours after the flare beginning which is also supported by the GOES x-ray flux readings.

In this chapter the results of the third specific objective, being this to obtain NOAA 12443 magnetic field structure and energy associated to it, were presented and thus successfully accomplished.

Figure 5.13 - NOAA 12443 energy budget.

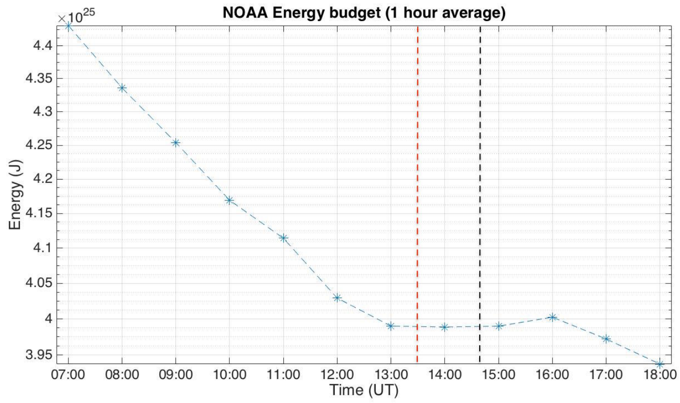

Energy budget ($E_{lff} - E_{pfss}$) averaged values over 1 hour. The red dashed line represent the approximated time in which the GOES readings started to climb for the third flare while the black dashed lines corresponds to the approximated time of the halo CME entries of the CDAW catalog.

SOURCE: Author's own work.

Figure 5.14 - NOAA 12443 energy budget.

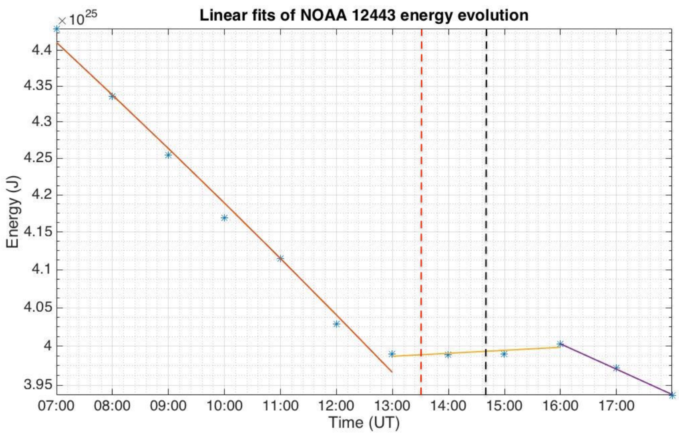

Energy budget hour average values linear fit for three time intervals. The red dashed line represent the approximated time in which the GOES readings started to climb for the third flare while the black dashed lines corresponds to the approximated time of the halo CME entries of the CDAW catalog.

SOURCE: Author's own work.

6 Triggering a solar flare

This chapter has the objective to investigate the possible triggers of NOAA 12443 M-class flare. However, it is necessary to bear in mind that in order to draw a conclusive scenario is complicated since a satisfactory description of the physical processes involved in a solar flare are yet to be seen (MURRAY et al., 2012). Therefore, a set of possibilities is going to be considered over the next sections in order to attempt to draw a scenario that is supported by the observations of NOAA 12443 structure made throughout this work and presented in the previous chapters.

The measurements presented so far indeed point that the flare and CME brought changes on NOAA 12443 magnetic field. However, they do not indicate what could have disturbed the AR in order to produce the observed events.

Both spatial and temporal distances of the NOAA 12443 and 12445 M-class flares, shown in Figures 5.4 and 5.3, suggests that NOAA 12445 flare could have influenced the evolution of NOAA 12443. Thus, some analysis were taken into account in order to evaluate this influence.

6.1 Magnetic energy evolution

The magnetic energy evolution was estimated using a linear force free and potential magnetic field extrapolations approach as discussed in the previous section. While a LFF extrapolation is insufficient to retrieve much of the field complexity, the results obtained in Figure 5.12 show a good match for the flaring time. However, the extrapolation results does not point what could have driven an instability in the system. Therefore, only by itself, the energy change does not represent a suitable candidate to trigger the flare but it is seen as a consequence of this activity.

6.2 Magnetic flux

The magnetic flux of an AR is directly proportional to the lifetime of a region (DRIEL-GESZTELYI; GREEN, 2015). Also, the emergence of magnetic flux from the convective zone into the solar atmosphere is responsible for a diversity of phenomena (CHEUNG; ISOBE, 2014). In order to observe the magnetic flux behaviour data from the HMI SHARPs magnetogram was integrated over the AR area to calculate the magnetic flux unveiling how the magnetic flux evolved around the time where the AR NOAA 12443 was close to the disk center.

As can be seen in Figure 6.1, the flux started to decrease from day 2015/11/03 after passing the disk center. The flux decreasing becomes more evident if the effects of the heliocentric angle is taken into consideration while calculating the element of area as featured Figure 6.1. Figure 6.2 shows the 20-hour average (1200 min) displayed in Figure 6.1 which unveils the drop trend in the graphic after November 3rd.

Figure 6.1 - AR NOAA 12443 magnetic flux.

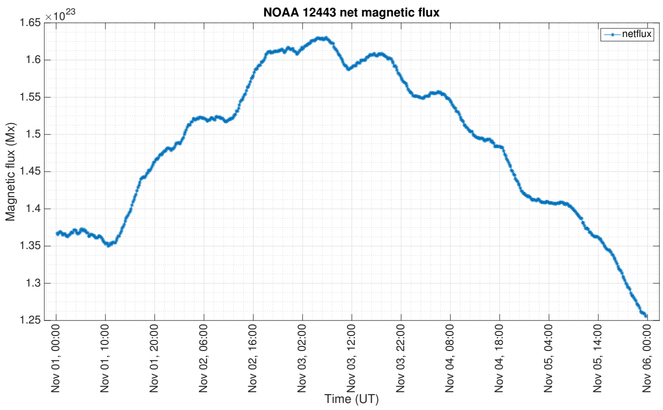

AR NOAA 12443 magnetic flux divided by the heliocentric angle.

SOURCE: Author's own work.

The results from the average transverse and LOS magnetic flux, displayed in Figures 6.3 and 6.4, show that there was a drop on the vertical flux at the same time that the horizontal flux suffered an increase. However, if the absolute values of the horizontal flux are considered, both plots will display the same trend as shown in Figure 6.5. Nevertheless, if the drops of the vertical flux and absolute horizontal flux are compared it is possible to see that the drop on the horizontal flux was more pronounced than the vertical counterpart. Therefore, the magnetic field orientation could be changing during that time.

It can be suggested that magnetic reconnection was taking place in the inner loops of AR NOAA 12443 as shown in Figure 6.6.

6.3 Filament eruption

Observations of prominence and filaments are quite common in the solar atmosphere and observations suggests these structures are made of dense cool chromospheric material embedded into the Corona (PARENTI, 2014). Prominences and filaments can

Figure 6.2 - AR NOAA 12443 averaged magnetic flux.

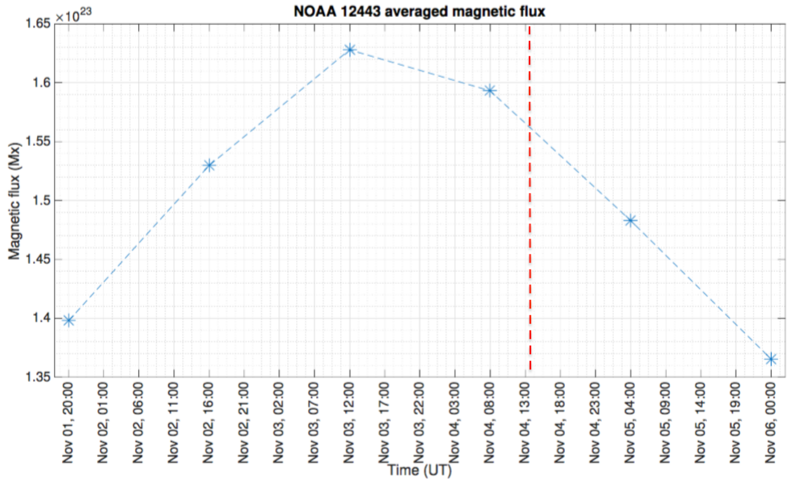

AR NOAA 12443 averaged magnetic flux divided by the heliocentric angle. Each point represents the average taken over 1200 minutes (20 hours).

SOURCE: Author's own work.

slowly decay or disappear suddenly as a result of thermal or dynamical instabilities. Filament eruptions in two different flaring ARs is also considered an evidence for sympathetic flares (HIGGINS et al., 2014).

Using AIA cutouts it was noticed that filament erupts from the AR NOAA 12445 close to 12:12 UT which is a few minutes after the flare starts to trigger. This filament could have touched the nested magnetic structure on the solar atmosphere of NOAA 12443 triggering the flare. However, the images suggest that the filament went towards the West limb and also, comparing the observations of AIA with observations of LASCO C2 and C3, the filament eruption offer a good match with a limb CME detected around 12:30 UT. Examples of the images used are displayed in Figure 6.7.

A similar activity was also observed around the flare time on NOAA 12443. The filament eruption that started just after the flare, represented by the dimming on Figure 6.8, that result on the CME that was first seen in The Large Angle Spectroscopic Coronagraph (LASCO) (BRUECKNER et al., 1995) C2 at 14:48 UT.

Using images from AIA at the 304 Å wavelength it is possible to observe that some hours before the flare onset, the main filament which reconnection started the flare

Figure 6.3 - AR NOAA 12443 vertical magnetic flux.

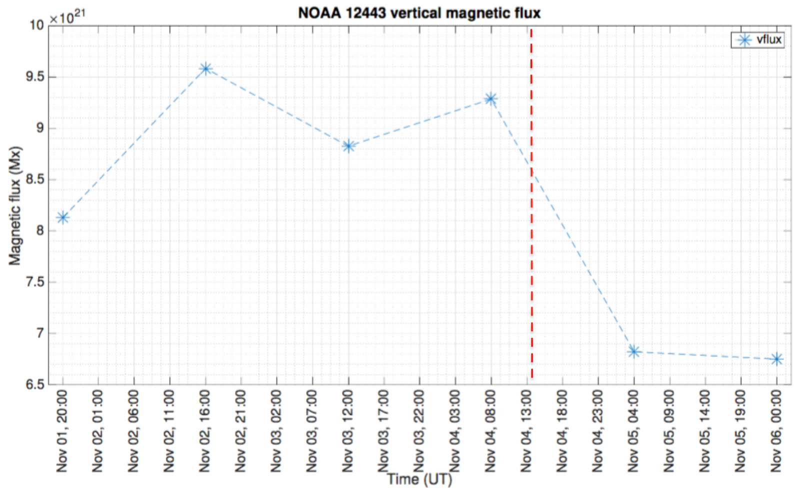

NOAA 12443 averaged vertical magnetic flux. The averages were taken every 1200 minutes (20 hours) which corresponds to 100 measurements of HMI. It can be noticed that the AR suffered a significant drop on the vertical flux close to the flare time.

SOURCE: Author's own work.

was already twisted and bending itself reaching a sigmoid shape. The sigmoid shape of a loop is considered one of the most important signatures of a flare due to its non-potential shape as shown, for example, in Gibson et al. (2002), Jiang et al. (2014) and Joshi et al. (2017). The filament evolution of AR 12433 is displayed in Figure 6.9 around the time of the flare onset.

6.4 Interactions with coronal holes

The magnetic field of the AR NOAA 12443 does not exclusively interact with nearby ARs but with any sort of solar magnetic structure that has a field of enough magnitude to disturb or bring any changes to it. In this context it is importante to notice the presence of some Coronal Holes (CHs) in the proximity of NOAA 12443.

An active region while close to a coronal hole is exposed to the electric currents associated to it that may contribute to the triggering of flares, filament eruptions and CMEs as studied, for example, by Gonzalez et al. (1996) and Harra (2012).

Part of the flux drop observed on NOAA 12443 might be related to interactions with the nearby CHs. However, with the methods used to evaluate the magnetic flux, it is not possible to determine which fraction of it was lost due to the interaction between

Figure 6.4 - AR NOAA 12443 horizontal magnetic flux.

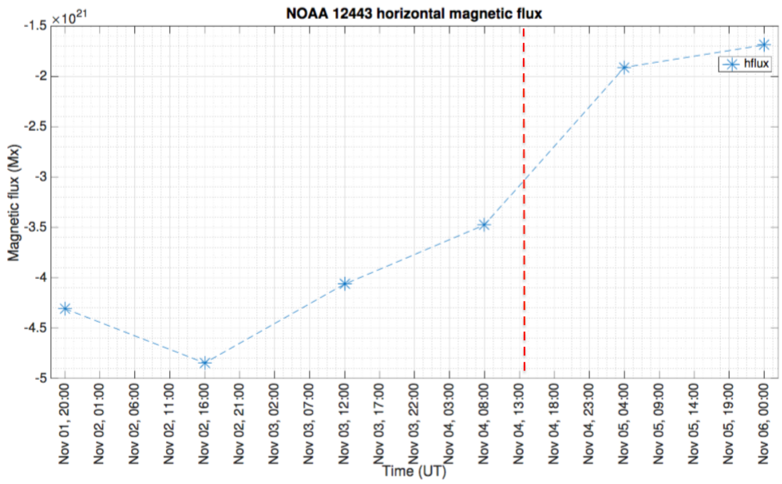

AR NOAA 12443 averaged horizontal magnetic flux. The averages were taken every 1200 minutes (20 hours) which corresponds to 100 measurements of HMI. It can be noticed that the AR suffered a significant increase on the horizontal flux close to the flare time.

SOURCE: Author's own work.

NOAA 12443 and the CHs.

Therefore, the CHs does not represent a mechanism that would suddenly trigger NOAA 12443 flare but the it could have helped NOAA 12443 on being prone to trigger flare by slowly eroding the AR magnetic field eventually forcing it on undergoing a process of magnetic reconnection.

6.5 Pressure balance

The wave created by the flaring activity of NOAA 12445 and the CMEs could have created pressure gradients capable to disturb NOAA 12443. Considering a PFSS approach, the magnetic field can be described by equation 6.1 where B_r^2, B_ϕ^2 and B_θ^2 are the magnetic field components in spherical coordinates.

$$B = \sqrt{B_r^2 + B_\phi^2 + B_\theta^2} \tag{6.1}$$

The magnetic pressure can be estimated as a function of the magnetic field using the equation below:

Figure 6.5 - AR NOAA 12443 horizontal magnetic flux.

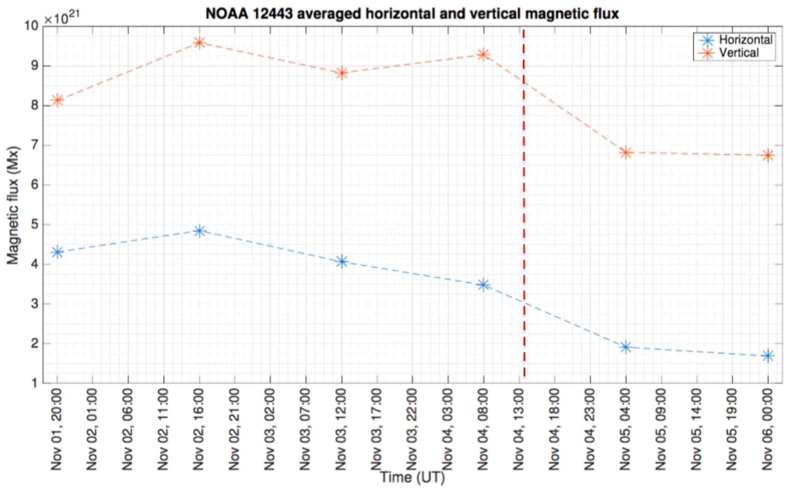

AR NOAA 12443 averaged absolute horizontal and vertical magnetic flux. The averages were taken every 1200 minutes (20 hours) which corresponds to 100 measurements of HMI. It can be noticed that the AR suffered a significant change on the horizontal flux close to the flare time.

SOURCE: Author own work.

$$P = \frac{B^2}{8\pi} \tag{6.2}$$

Then, the magnetic pressure was calculated using the values obtained with a potential field extrapolation as an entry for Equation 6.2 for different heights ($R_\odot = 1.00, 1.10, 1.20, 1.39, 1.65, 2.15, 2.50$) using the model presented in RODRÍGUEZ GÓMEZ (2017) in order to see if there were significant changes along the day. The magnetic pressure values were averaged over the layers with a temporal resolution of six hours on 2015/11/04 at 00:04, 06:04, 12:04 and 18:04 UT. Despite of the small temporal resolution, Figure 6.10 shows that the surroundings of NOAA 12445 suffered a pressure drop around the flare time. Therefore, it is possible that a coronal wave could have propagated outwards NOAA 12445.

6.6 Waves

Violent processes resultant from magnetic reconnection can create waves, such as shocks and magnetohydrodynamic (MHD) waves, that can travel along the solar atmosphere and are capable to disturb different regions of the atmosphere, e.g.

Figure 6.6 - Inner loops magnetic field reconnection.

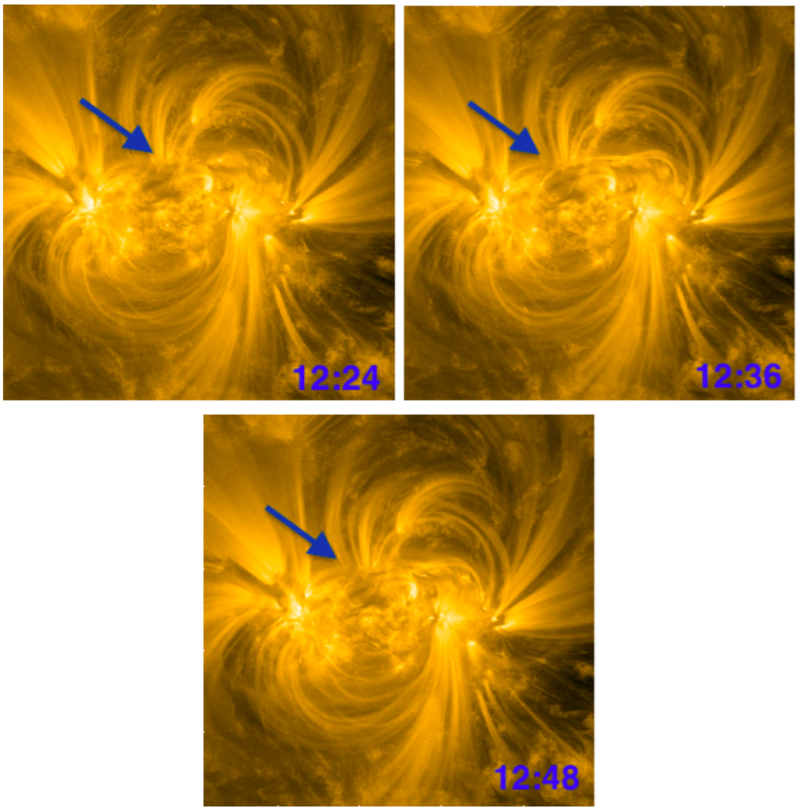

Cutouts with a 12-minute cadence of AIA on the wavelength 193Å. Close to the center of the AR, it can be noticed that some of the inner loops are reconnecting.

SOURCE: Author's own work.

Warmuth (2015), Khomenko e Collados (2015) and Ofman e Thompson (2002). Biesecker e Thompson (2000) identifies coronal waves as a possible external trigger mechanism and also that such waves are able to alter the energy balance of the field lines.

The time lag between the two M-class flares are approximately one and a half hour which is enough time, e.g. Schrijver et al. (2011), for a wave created by NOAA 12445 to propagate towards NOAA 12443 creating a perturbation capable of destabilizing the system.

The results obtained using AIA 211Å and 193Å reveal dimming and vibrating loops that can be observed using a image subtraction technique resulting from the flaring activities of NOAA 12443 and 12445.

Figure 6.7 - AIA images subtraction.

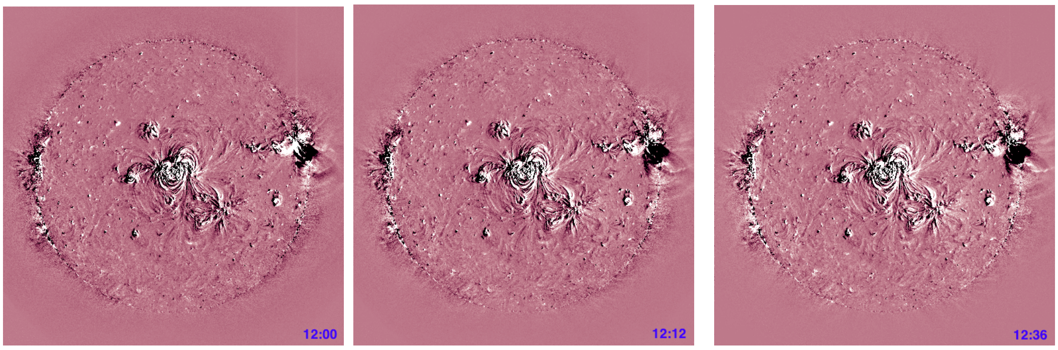

This set of images show a subtraction of images from AIA at the 193Å wavelength. The same base image was subtracted from each subsequent fit.

SOURCE: Author's own work.

Figure 6.8 - AIA images subtraction 2.

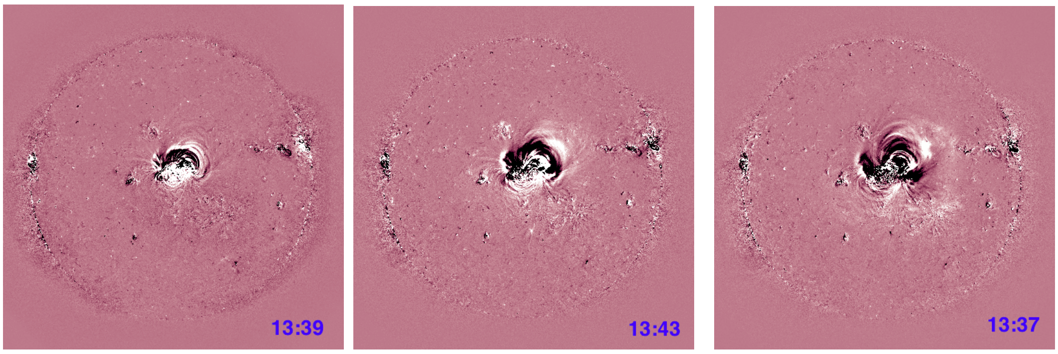

Images of the filament eruption and subsequent dimming on NOAA 12443. This set of images show a subtraction of images from AIA at the 193Å wavelength. The same base image was subtracted from each subsequent fit.

SOURCE: Author's own work.

However, as can be seen in Figure 5.3, there are structures that could prevent the wave created by NOAA 12445 to reach NOAA 12443. Those structures are the ARs NOAA 12446 and 12441 and the CH highlighted by the boxes 2 and 4.

It is possible that the recurrent activity in AR 12445 may influence the filament eruption and halo CME in AR 12443. However, it is difficult to state the extent of the waves influence on the events unless large Moreton or EIT waves are involved.

Figure 6.9 - NOAA 12443 filament evolution.

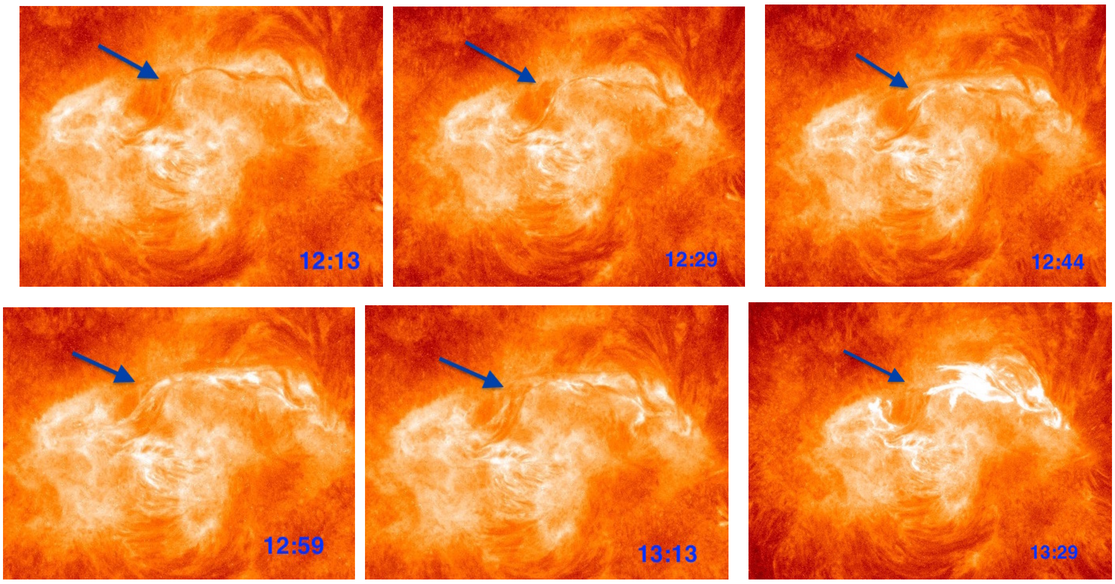

Images of the NOAA 12443 filament evolution. This set of images was taken from AIA at the 304Å wavelength.

SOURCE: Author's own work.

In order to unveil more properties of NOAA 12443 evolution the research group employed a wavelet analysis on some cutouts of AIA data series. The analysis is based on a previous work presented by Silva e Satyamurty (2013) and consists on analyzing the response of the signal for different wavelengths.

The vibration pattern associated to the signal of AIA over 2 hours prior to NOAA 12443 flare indicates that the region is oscillating in localized regions prior to the flare (Figure 6.11).

Studying how the wavelengths responds to different periods, Figures 6.12 and 6.13, it is possible to see that the regions NOAA 12443 and 12445 show a strong response to waves with a large period and a rather poor response to waves with a small period.

Tracking the changes in intensity along the path that separate NOAA 12443 and 12445 the results, Figures 6.14 and 6.15, it can be observed a strong fluctuation which is taking place in an already unstable region.

Figure 6.10 - NOAA 12445 magnetic pressure.

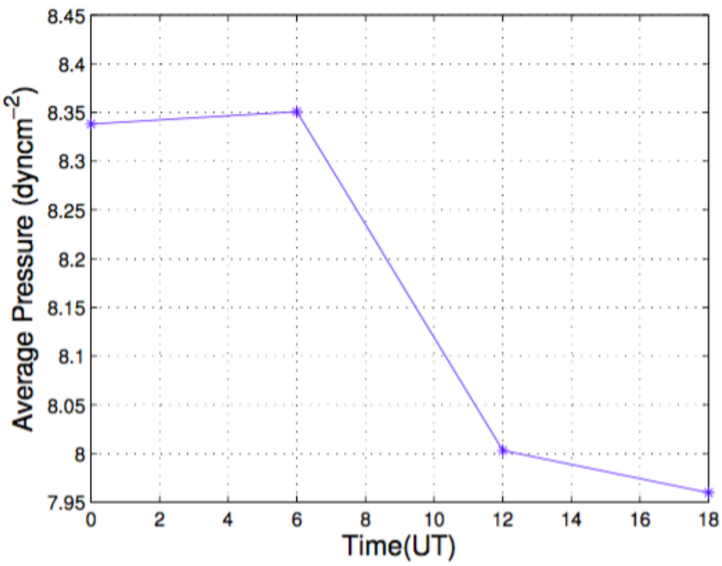

This analysis was led by Dr. Rodriguez Gómez. Average value of the magnetic pressure around NOAA 12445 calculated with a potential field.

SOURCE: Courtesy of Dr. Rodriguez Gómez.

6.7 AR connections

Using a potential magnetic field extrapolation on the full disk before the flare, represented in Figure 6.16, it can be seen that the AR NOAA 12443 was connected to other ARs and, therefore, perturbations that occurred in those ARs could have propagated using those field lines to the AR NOAA 12443 which is a condition for the occurrence of sympathetic flares (WANG et al., 2001). One of those connections was with the AR NOAA 12446 which was in the zone perturbed by the wave created by the flaring activity of the AR NOAA 12445.

Heat conduction has also been reported as responsible for triggering sympathetic flares (CHANGXI et al., 2000) and the connections between those ARs offer the environment for heat to conduct to NOAA 12443.

Therefore, assuming that the perturbation used those field lines as paths to propagate to the AR NOAA 12443, it is likely that the flaring activity of NOAA 12445 could be seen as a trigger.

Figure 6.11 - Wavelet analysis of NOAA 12443 - 1.

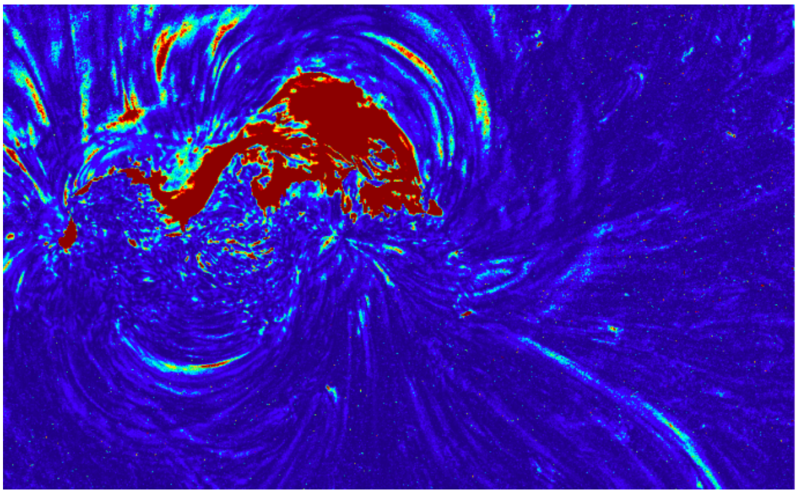

This wavelet analysis is an ongoing work by the research team led by Dr. Vieira. The results exhibited in this figure were calculated some minutes before the flare and show that NOAA 12443 was vibrating locally.

SOURCE: Courtesy: Dr. Vieira.

6.8 Discussion

This work studied the evolution of the AR NOAA 12443 using a series of different tools in order to try to understand what could have been the trigger mechanism for the solar flare that occurred at 13:30 UT and to what extent the flaring activity displayed by NOAA 12445 contributed to it. Using data provided by HMI, AIA and GOES it was possible to track the evolution of NOAA 12443 and the context in which the events of this region took place. By itself, the temporal and spatial distances between the flares and ARs that gave rise to them suggests that the activities of NOAA 12445 might have contributed to trigger NOAA 12443 flare.

The information stored at the HMI SHARPS also provided to reach some agreement with the energy curves providing support for the claim that one M-class flare and the Halo CME are connected to the evolution of this region even considering that, using the linear force free approach, the energy budget displays rather modest values for energy change around the flaring time. The changes in energy recovered through the data extrapolations where capable of matching in time the flux data provided by GOES. The amount in which such changes occurred, however, are uncertain using a linear-force free approach and should be seen as the gross picture of AR NOAA

Figure 6.12 - Wavelet analysis of NOAA 12443 - 2.

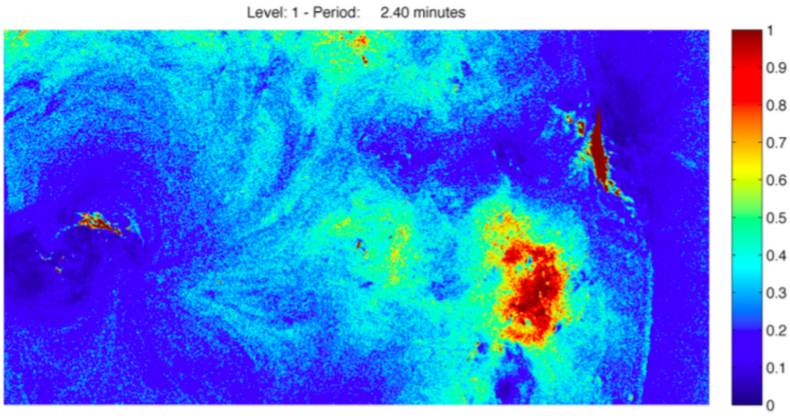

This wavelet analysis is an ongoing work by the research team led by Dr. Vieira. The results exhibited in this figure were calculated from 11:30 to 13:30 UT covering 150 images.

SOURCE: Courtesy: Dr. Vieira.

12443 energy evolution.

The shape of the curves from the Absolute Value of the Net Vertical Current Helicity and Force-free parameter, Figures 5.5 and 5.8, shows agreement with the flaring activity time and a rather poor agreement with the halo CME. It is, however, important to remember that the CME time is the time which it was first seen on LASCO-C2.

Comparing the results we could notice that the change in vertical helicity and vertical current, Figures 5.5 and 5.6, are more pronounced that the changes in energy. The total unsigned vertical current helicity also seems to show a trend alike the energy evolution curve. The sharp changes in the vertical current are evidenced by the results displayed in Figure 5.7 which indicate that the sharp drop on those currents might be an indicative that the flare was going to happen at some point.

The wavelet analysis can be seen as an extra of this work since they were not among the initial objectives. During the development of the activities the time interval separating the events led the group to investigate the possible interference of the flare created by NOAA 12445 on the evolution of NOAA 12443 and, in this sense, the wavelet analysis appeared as a possible tool to study the signal response registered by the AIA instruments. These results are yet, however, on their early stages and should be seen with care.

Figure 6.13 - Wavelet analysis of NOAA 12443 - 3.

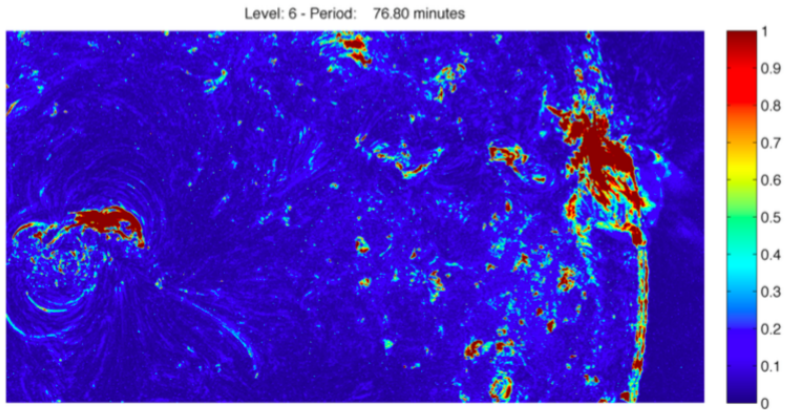

This wavelet analysis is an ongoing work by the research team led by Dr. Vieira. The results exhibited in this figure were calculated from 11:30 to 13:30 UT covering 150 images.

SOURCE: Courtesy: Dr. Vieira.

The results found cast light into different possibilities for what could have been the trigger for NOAA 12443 flare. The next paragraph will present what, in the eyes of the research team, is the best possible explanation.

The magnetic flux drop on November 4th evolution made NOAA 12443 unable to sustain its magnetic structure. The presence of magnetic reconnection on the lower loops of the region and the sigmoid shape of the loop indicate that the region was, indeed, prone to reconnect. Thus, a perturbation that reaching NOAA 12443 could obligate it to reconfigure itself and reach a stable state which would result in the energy release with a flare and a CME. It is complicated for a Alfvèn wave originated from NOAA 12445 could reach NOAA 12443 due to the presence of the magnetic structures on the way (ARs and CHs) however, some evidences such as the wavelet analysis are indicating that this could have happened. As a result of its own evolution and a probable interference from NOAA 12445 flare then, the reconfiguration the NOAA 12443 energy build-up/release, and changes into the vertical current and helicity took place.

Even considering that the given description is essentially qualitative, numerical simulations can be used to verify the proposed scenario. This is, however, out of the scope of this work.

Figure 6.14 - Wavelet analysis of NOAA 12443 - 4.

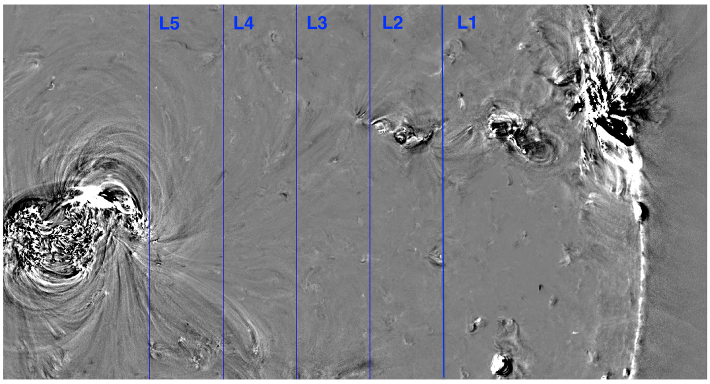

This wavelet analysis is an ongoing work by the research team led by Dr. Vieira. This figure shows the points where a separated wavelet analysis was performed to verify the signal along the path from NOAA 12445 to NOAA 12443.

SOURCE: Courtesy: Dr. Vieira.

6.9 Conclusion

The objective of this chapter was to study the mechanisms that could have played a major role on triggering NOAA 12443 M-class flare studying some of the various changes that occurred on the solar atmosphere prior to NOAA 12443 flare and if it is possible to see a direct influence of NOAA 12445 on it.

The distribution of the structures in the solar disk presented an close to ideal situation to verify if, in this case, the evolution of an AR interfered in the evolution of another AR. This topic is yet source of debates within the scientific community.

The magnetic flux results shown that NOAA 12443 was already decaying before its flare took place. It is possible to notice that the changes on the vertical magnetic flux were more pronounced than the its horizontal counterpart indicating that the magnetic field suffered some changes on its direction.

Some hours before NOAA 12443 flare the region was already seeing some energetic activities and the loop which eventually came to reconnect were twisted in a sigmoid shape indicating that the region was unstable

Figure 6.15 - Wavelet analysis of NOAA 12443 - 5.

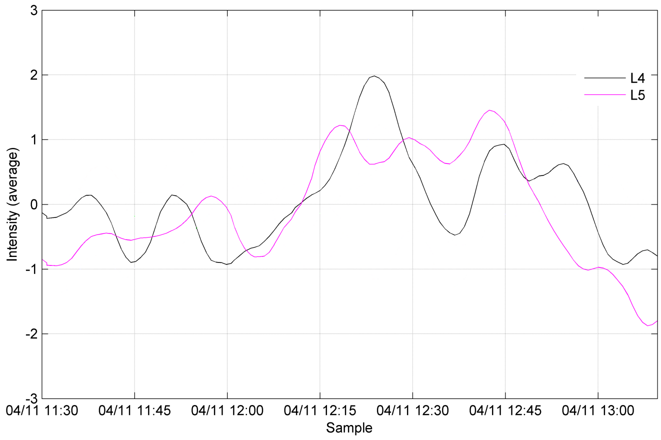

This wavelet analysis is an ongoing work by the research team led by Dr. Vieira. The results exhibited in this figure were calculated from 11:30 to 13:30 UT covering 150 images and take the results of the two lines L5 and L4, exhibited in Figure 6.14, which are already in the vicinity of NOAA 12443.

SOURCE: Courtesy: Dr. Vieira.

Calculating the average magnetic pressure for the coronal layers using a potential field it was possible to see that a significant pressure drop took place around NOAA 12445 after its flare. It is not possible to see, however, using an image subtraction from AIA large moreton waves propagating from NOAA 12445 towards NOAA 12443.

The results of the wavelet analysis are still under discussion and development but the results that achieved so far indicated that the flare was a rather localized event within NOAA 12443 boundaries and that it is possible that a perturbation could have propagated from NOAA 12445 eventually hitting NOAA 12443. It is also remarkable to notice how both regions shown a rather strong response to long period waves while the remaining structures of the solar surface shown a stronger response to short period waves.

In this chapter the results discussed represents an extra part of this work, going beyond our initial objectives, and together with the results from chapter 5 provided an insight in some of the probable triggers for NOAA 12443 flare that allowed to study a possible sympaty between the flares of NOAA 12443 and 12445.

Figure 6.16 - Potential field map.

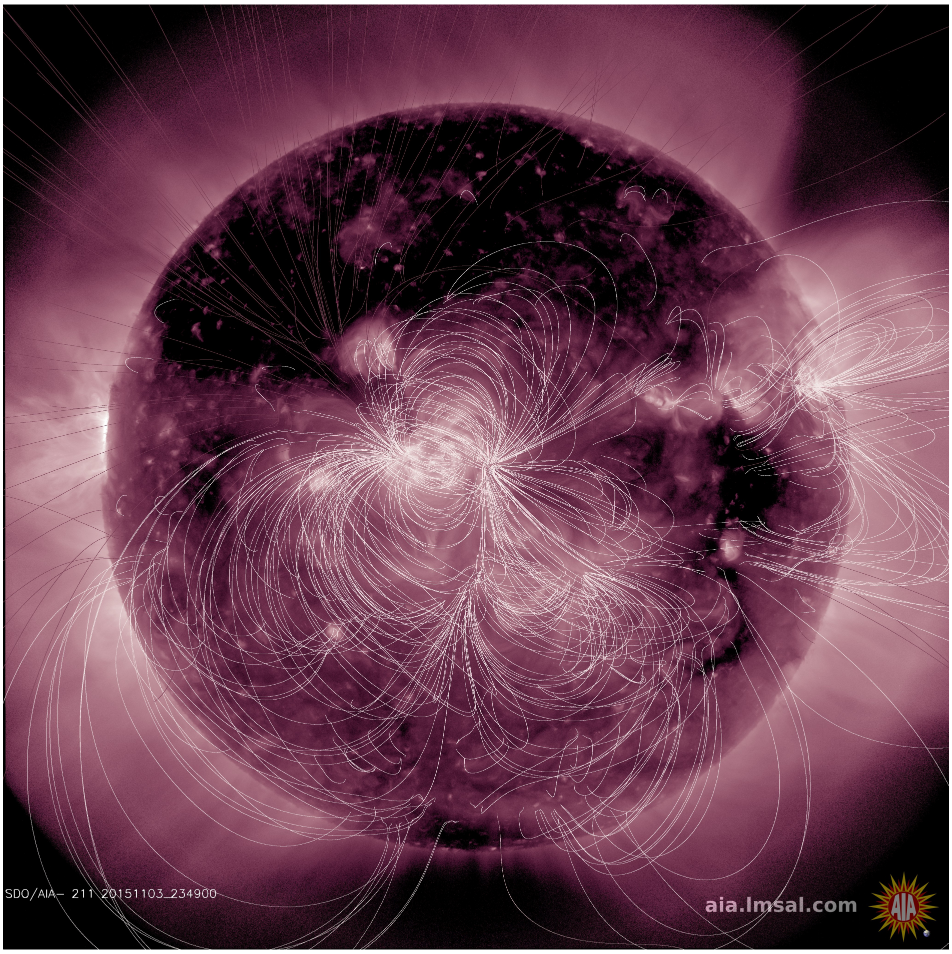

Potential field map provided by AIA LMSAL. As it can be seen the ARs on the solar disk are connected by their magnetic fields.

SOURCE: AIA LMSAL aia.lmsal.com

Despite the fact that discussing the possible triggers of NOAA 12443 M-class flare was not within the initial propose this study led the group to interesting results that enriched this work. It is worthwhile to remember that uncovering what trigger a solar flare is still an open problem and, therefore, this work shows this group attempt to strive over a better understanding of this phenomena.

7 CONCLUDING REMARKS

The objective of this work was to Study the evolution of the AR NOAA 12443 during the time that it was observed in the solar disk with a special attention to November 4th of 2015 which is the time that it triggered a M-class flare.

In order to do so a series of activities were proposed to present a case-study of NOAA 12443 evolution. First it were produced maps of the solar surface (chapter 4) and then the energy evolution of the AR was studied (chapter 5). As an extra, the mechanisms that could have triggered NOAA 12443 flare were also discussed (chapter 6).

The results displayed over chapter 4 and 5 were complementary between themselves since they allowed the study of NOAA 12443 in different levels of the atmosphere. While the solar surface maps of chapter 4 focused on the photospheric structure of the region, the magnetic field extrapolations displayed in chapter 5 study the energy changes that took place on the above layers.

Results from both mapping and extrapolations shows that the AR NOAA 12443 has, indeed, a remarkable structure if compared to the other ARs that appeared on the nearby months. The NOAA 12443 dynamics, seen in the maps, and the magnetic field extrapolated show that the AR had enough energy to trigger an energetic event as indeed it did. However, with the presented analysis, it is still difficult to evaluate with a higher degree of certainty the influence that other ARs and surrounding solar structures had in the triggering of the explosive activity within NOAA 12443.

Changes in helicity, current and force free parameter measured by HMI seems to be aligned with what was observed with the maps produced using Hinode data since it was possible to see that the solar surface was also passing through changes that would eventually propagate to the layers above. It is notable, among the maps displayed, that the fine structure of the AR NOAA 12443 was changing over time. Furthermore, due to the observed motion, it is reasonable to assume that the footpoints of the magnetic field lines were also moving which could eventually trigger a flare however, a specific test was not performed to identify and measure the movement of those regions.

The changing values obtained for the magnetic field and, thus, energy are coherent with the presence of magnetic field or velocity gradients indicated by the asymmetries of Stokes V.

Since the dopplergrams measure only the velocity along the LOS it is not possible with the used approach to investigate the presence of waves that might disturb NOAA 12443. They do, however, show that the most intense flux is located in between the poles of NOAA 12443. The magnetic field reconnection observed in the inner rings of NOAA 12443 seems to be occurring close to the some of the regions where the marks for intense downflows are located. Therefore, the presence of those downflows may also be an indicative of the AR's activity.

The analysis presented in chapter 6 show based on its results this group interpretation for what triggered NOAA 12443. This interpretation is based on the results displayed in chapters 4 and 5 and also of observations of magnetic flux, atmospheric waves, structural changes on NOAA 12443 and a wavelet analysis. Furthermore, those results were compared multiple times with videos and images of the solar atmosphere and NOAA 12443.

The wavelet analysis presented in chapter 6 are still being worked on and those results should be treated with care. However, they give some meaningful insights on NOAA 12443 M-class flare. First, it can be seen that, in comparison to the size of NOAA 12443, the flare was a rather localized event since only a set of its loops reconnected to produce the flare. Also there is some suggestions that a perturbation could have propagated from NOAA 12445 to NOAA 12443 after the 12:00 UT flare.

The usage of data from HMI, AIA, HINODE and GOES proved to be necessary to draw a coherent scenario to describe the evolution of the AR NOAA 12443 using results obtained with images and polarimetry. In this sense, this work provides not only a case-study but also prepared the ground for the author's future PhD work.

For future works it is scheduled to finish the wavelet analysis and try to state if there is a sympathy between the flares of NOAA 12443 and 12445. Also, this study could be further extended with a non-linear force free extrapolation which would enrich our comprehension of NOAA 12443 magnetic field.

REFERENCES

ASCHWANDEN, M. J. **Physics of the solar corona**: an introduction with problems and solutions. 2nd. ed. Berlin: Springer Berlin Heidelberg, 2005. 29, 30

BIESECKER, D. A.; THOMPSON, B. J. Sympathetic flaring with BATSE, GOES, and EIT data. **Journal of Atmospheric and Solar-Terrestrial Physics**, v. 62, p. 1449–1455, nov. 2000. 71

BORNMANN, P. L.; SPEICH, D.; HIRMAN, J.; MATHESON, L.; GRUBB, R.; GARCIA, H. A.; VIERECK, R. **GOES x-ray sensor and its use in predicting solar-terrestrial disturbances**. 1996. 2812 - 2812 - 8 p. Disponível em: <http://dx.doi.org/10.1117/12.254076>. 35

BRUECKNER, G. E.; HOWARD, R. A.; KOOMEN, M. J.; KORENDYKE, C. M.; MICHELS, D. J.; MOSES, J. D.; SOCKER, D. G.; DERE, K. P.; LAMY, P. L.; LLEBARIA, A.; BOUT, M. V.; SCHWENN, R.; SIMNETT, G. M.; BEDFORD, D. K.; EYLES, C. J. The Large Angle Spectroscopic Coronagraph (LASCO). **Solar Physics**, v. 162, p. 357–402, dez. 1995. 67

CHANGXI, Z.; HUANING, W.; JINGXIU, W.; YIHUA, Y. Sympathetic flares in two adjacent active regions. **Solar Physics**, v. 195, n. 1, p. 135–148, 2000. ISSN 1573-093X. Disponível em: <http://dx.doi.org/10.1023/A:1005237531865>. 74

CHEUNG, M. C. M.; ISOBE, H. Flux emergence (theory). **Living Reviews in Solar Physics**, v. 11, n. 1, p. 3, 2014. ISSN 1614-4961. Disponível em: <http://dx.doi.org/10.12942/lrsp-2014-3>. 65

DEGL'INNOCENTI, E. L. Magnetic field measurements. In: Sanchez, F.; Collados, M.; Vazquez, M. (Ed.). **Solar observations: techniques and interpretation**. [S.l.: s.n.], 1992. p. 71. 18

DRIEL-GESZTELYI, L. van; GREEN, L. M. Evolution of active regions. **Living Reviews in Solar Physics**, v. 12, n. 1, p. 1, 2015. ISSN 1614-4961. Disponível em: <http://dx.doi.org/10.1007/lrsp-2015-1>. 4, 5, 65

FRANZ, M. **Spectropolarimetry of sunspot penumbrae**: a comprehensive study of the evershed effect using high resolution data from the space-borne solar observatory HINODE. 176 p. Tese (PhD Thesis) — Kiepenheuer Institut fur Sonnenphysik, 2011. 45

GARY, G. A. Plasma beta above a solar active region: Rethinking the paradigm. **Solar Physics**, v. 203, n. 1, p. 71–86, 2001. ISSN 1573-093X. Disponível em: <http://dx.doi.org/10.1023/A:1012722021820>. 29

GARY, G. A.; HU, Q.; LEE, J. K. A rapid, manual method to map coronal-loop structures of an active region using cubic bézier curves and its applications to misalignment angle analysis. **Solar Physics**, v. 289, n. 3, p. 847–865, 2014. ISSN 1573-093X. Disponível em:
<http://dx.doi.org/10.1007/s11207-013-0359-8>. 50

GIBSON, S. E.; FLETCHER, L.; ZANNA, G. D.; PIKE, C. D.; MASON, H. E.; MANDRINI, C. H.; DéMOULIN, P.; GILBERT, H.; BURKEPILE, J.; HOLZER, T.; ALEXANDER, D.; LIU, Y.; NITTA, N.; QIU, J.; SCHMIEDER, B.; THOMPSON, B. J. The structure and evolution of a sigmoidal active region. **The Astrophysical Journal**, v. 574, n. 2, p. 1021, 2002. Disponível em:
<http://stacks.iop.org/0004-637X/574/i=2/a=1021>. 68

GONZÁLEZ, N. B. **Spectropolarimetry of sunspot penumbrae**. 123 p. Tese (PhD Thesis) — Max Planck Institute for Solar System Research, Göttingen, 2006. 15, 37, 39

GONZALEZ, W. D.; TSURUTANI, B. T.; MCINTOSH, P. S.; GONZALEZ, A. L. Clúa de. Coronal hole-active region-current sheet (charcs) association with intense interplanetary and geomagnetic activity. **Geophysical Research Letters**, v. 23, n. 19, p. 2577–2580, 1996. ISSN 1944-8007. Disponível em:
<http://dx.doi.org/10.1029/96GL02393>. 68

HARRA, L. K. The Role of Coronal Hole and Active Region Boundaries in Solar Wind Formation. In: Bellot Rubio, L.; Reale, F.; Carlsson, M. (Ed.). **4th Hinode Science Meeting: Unsolved Problems and Recent Insights**. [S.l.: s.n.], 2012. (Astronomical Society of the Pacific Conference Series, v. 455), p. 315. 68

HE, H.; WANG, H.; YAN, Y.; CHEN, P. F.; FANG, C. Variations of the 3-d coronal magnetic field associated with the x3.4-class solar flare event of ar 10930. **Journal of Geophysical Research: Space Physics**, v. 119, n. 5, p. 3286–3315, 2014. ISSN 2169-9402. Disponível em:
<http://dx.doi.org/10.1002/2013JA019157>. 61

HIGGINS, P. A.; SCHRIJVER, C. J.; TITLE, A. M.; BLOOMFIELD, D. S.; GALLAGHER, P. T. A study of sympathetic eruptions using the Heliophysics Events Knowledgebase. In: **American Astronomical Society Meeting**

Abstracts #224. [S.l.: s.n.], 2014. (American Astronomical Society Meeting Abstracts, v. 224), p. 123.16. 67

HOOD, A. W.; HUGHES, D. W. Solar magnetic fields. **Physics of the Earth and Planetary Interiors**, v. 187, n. 3, p. 78 – 91, 2011. ISSN 0031-9201. Special Issue: Planetary Magnetism, Dynamo and Dynamics. Disponível em: <http://www.sciencedirect.com/science/article/pii/S0031920111000744>. 28

INIESTA, J. C. d. J. C. T. Book; Book/Illustrated. **Introduction to spectropolarimetry**. [S.l.]: Cambridge ; New York : Cambridge University Press, 2003. Includes bibliographical references and index. ISBN 0521818273 (hbk.). 15, 19, 21, 22, 23

JIANG, C.; WU, S. T.; FENG, X.; HU, Q. Formation and eruption of an active region sigmoid. i. a study by nonlinear force-free field modeling. **The Astrophysical Journal**, v. 780, n. 1, p. 55, 2014. Disponível em: <http://stacks.iop.org/0004-637X/780/i=1/a=55>. 68

JING, J.; CHEN, P. F.; WIEGELMANN, T.; XU, Y.; PARK, S.-H.; WANG, H. Temporal evolution of free magnetic energy associated with four x-class flares. **The Astrophysical Journal**, v. 696, n. 1, p. 84, 2009. Disponível em: <http://stacks.iop.org/0004-637X/696/i=1/a=84>. 61

JOSHI, B.; KUSHWAHA, U.; VERONIG, A. M.; DHARA, S. K.; SHANMUGARAJU, A.; MOON, Y.-J. Formation and eruption of a flux rope from the sigmoid active region noaa 11719 and associated m6.5 flare: A multi-wavelength study. **The Astrophysical Journal**, v. 834, n. 1, p. 42, 2017. Disponível em: <http://stacks.iop.org/0004-637X/834/i=1/a=42>. 68

KHOMENKO, E.; COLLADOS, M. Oscillations and waves in sunspots. **Living Reviews in Solar Physics**, v. 12, n. 1, p. 6, 2015. ISSN 1614-4961. Disponível em: <http://dx.doi.org/10.1007/lrsp-2015-6>. 71

KOSOVICHEV, A. Subsurface structure of sunspots. **Astronomische Nachrichten**, WILEY-VCH Verlag, v. 323, n. 3-4, p. 186–191, 2002. ISSN 1521-3994. Disponível em: <http://dx.doi.org/10.1002/1521-3994(200208)323:3/4<186::AID-ASNA186>3.0.CO;2-I>. 4

KOSUGI, T.; MATSUZAKI, K.; SAKAO, T.; SHIMIZU, T.; SONE, Y.; TACHIKAWA, S.; HASHIMOTO, T.; MINESUGI, K.; OHNISHI, A.; YAMADA,

T.; TSUNETA, S.; HARA, H.; ICHIMOTO, K.; SUEMATSU, Y.; SHIMOJO, M.; WATANABE, T.; SHIMADA, S.; DAVIS, J. M.; HILL, L. D.; OWENS, J. K.; TITLE, A. M.; CULHANE, J. L.; HARRA, L. K.; DOSCHEK, G. A.; GOLUB, L. The Hinode (Solar-B) mission: an overview. , v. 243, p. 3–17, jun. 2007. 37

LEMEN, J. R.; TITLE, A. M.; AKIN, D. J.; BOERNER, P. F.; CHOU, C.; DRAKE, J. F.; DUNCAN, D. W.; EDWARDS, C. G.; FRIEDLAENDER, F. M.; HEYMAN, G. F.; HURLBURT, N. E.; KATZ, N. L.; KUSHNER, G. D.; LEVAY, M.; LINDGREN, R. W.; MATHUR, D. P.; MCFEATERS, E. L.; MITCHELL, S.; REHSE, R. A.; SCHRIJVER, C. J.; SPRINGER, L. A.; STERN, R. A.; TARBELL, T. D.; WUELSER, J.-P.; WOLFSON, C. J.; YANARI, C.; BOOKBINDER, J. A.; CHEIMETS, P. N.; CALDWELL, D.; DELUCA, E. E.; GATES, R.; GOLUB, L.; PARK, S.; PODGORSKI, W. A.; BUSH, R. I.; SCHERRER, P. H.; GUMMIN, M. A.; SMITH, P.; AUKER, G.; JERRAM, P.; POOL, P.; SOUFLI, R.; WINDT, D. L.; BEARDSLEY, S.; CLAPP, M.; LANG, J.; WALTHAM, N. The Atmospheric Imaging Assembly (AIA) on the Solar Dynamics Observatory (SDO). **Solar Physics**, v. 275, p. 17–40, jan. 2012. 49

LONGCOPE, D. W. Topological methods for the analysis of solar magnetic fields. **Living Reviews in Solar Physics**, v. 2, n. 1, p. 7, 2005. ISSN 1614-4961. Disponível em: <http://dx.doi.org/10.12942/lrsp-2005-7>. 44

METCALF, T. R.; ROSA, M. L. D.; SCHRIJVER, C. J.; BARNES, G.; BALLEGOOIJEN, A. A. van; WIEGELMANN, T.; WHEATLAND, M. S.; VALORI, G.; MCTTIERNAN, J. M. Nonlinear Force-Free Modeling of Coronal Magnetic Fields. II. Modeling a Filament Arcade and Simulated Chromospheric and Photospheric Vector Fields. **Solar Physics**, v. 247, p. 269–299, fev. 2008. 34

MILIĆ, I.; FAUROBERT, M.; ATANACKOVIĆ, O. Inference of magnetic fields in inhomogeneous prominences. , v. 597, p. A31, jan. 2017. 39

MORINAGA, S.; NAGATA, S.; ICHIMOTO, K.; SUEMATSU, Y.; TSUNETA, S.; KATSUKAWA, Y.; SHIMIZU, T.; SHINE, R. A.; TARBELL, T. D.; TITLE, A. M.; LITES, B.; KUBO, M.; SAKURAI, T. Center-to-Limb Variation of Stokes V Asymmetries in Solar Pores Observed with the Hinode Spectro-Polarimeter. **Publ. Astron. Soc. Japan**, v. 59, p. 613–+, nov. 2007. 42

MURRAY, S. A.; BLOOMFIELD, D. S.; GALLAGHER, P. T. The evolution of sunspot magnetic fields associated with a solar flare. **Solar Physics**, v. 277, p. 45–57, mar. 2012. 65

NAKAGAWA, Y.; RAADU, M. A. On practical representation of magnetic field. **Solar Physics**, v. 25, p. 127–135, jul. 1972. 25

OFMAN, L.; THOMPSON, B. J. Interaction of eit waves with coronal active regions. **The Astrophysical Journal**, v. 574, n. 1, p. 440, 2002. Disponível em: <http://stacks.iop.org/0004-637X/574/i=1/a=440>. 71

PARENTI, S. Solar prominences: observations. **Living Reviews in Solar Physics**, v. 11, n. 1, p. 1, 2014. ISSN 1614-4961. Disponível em: <http://dx.doi.org/10.12942/lrsp-2014-1>. 66

PESNELL, W. D.; THOMPSON, B. J.; CHAMBERLIN, P. C. The solar dynamics observatory (sdo). **Solar Physics**, v. 275, n. 1, p. 3–15, 2012. ISSN 1573-093X. Disponível em: <http://dx.doi.org/10.1007/s11207-011-9841-3>. 37, 49

RÉGNIER, S.; AMARI, T.; KERSALÉ, E. 3D Coronal magnetic field from vector magnetograms: non-constant-alpha force-free configuration of the active region NOAA 8151. **Astronomy & Astrophysics**, v. 392, p. 1119–1127, set. 2002. 34

RÉGNIER, S.; FLECK, B.; ABRAMENKO, V.; ZHANG, H.-Q. Evolution of the Magnetic Energy Budget in AR 10486 from Potential and Nonlinear Force-Free Models. In: Innes, D. E.; Lagg, A.; Solanki, S. A. (Ed.). **Chromospheric and Coronal Magnetic Fields**. [S.l.: s.n.], 2005. (ESA Special Publication, v. 596), p. 61.1. 34

RIETMULLER, T. **Investigations of small-scale magnetic features on the solar surface**. 211 p. Tese (PhD Thesis) — Max Planck Institute for Solar System Research, Göttingen, 2013. 6

RODRÍGUEZ GÓMEZ, J. M. **Evolution of the electron density, temperature distribution in the solar corona during solar cycles 23 and 24**. 188 p. Tese (Doutorado) — Instituto Nacional de Pesquisas Espaciais (INPE), São José dos Campos, 2017-03-16 2017. Disponível em: <http://urlib.net/sid.inpe.br/mtc-m21b/2017/02.16.21.15>. Acesso em: 13 set. 2017. 70

ROSA, M. L. D.; SCHRIJVER, C. J.; BARNES, G.; LEKA, K. D.; LITES, B. W.; ASCHWANDEN, M. J.; AMARI, T.; CANOU, A.; MCTIERNAN, J. M.; RÉGNIER, S.; THALMANN, J. K.; VALORI, G.; WHEATLAND, M. S.; WIEGELMANN, T.; CHEUNG, M. C. M.; CONLON, P. A.; FUHRMANN, M.; INHESTER, B.; TADESSE, T. A Critical Assessment of Nonlinear Force-Free

Field Modeling of the Solar Corona for Active Region 10953. **The Astrophysical Journal**, v. 696, p. 1780–1791, maio 2009. 35, 50

SANTIAGO, J. M. B. **The fine structure of the sunspot penumbra**. 153 p. Tese (PhD Thesis) — Max Planck Institute for Solar System Research, Göttingen, 2004. 17

SCHERRER, P. H.; SCHOU, J.; BUSH, R. I.; KOSOVICHEV, A. G.; BOGART, R. S.; HOEKSEMA, J. T.; LIU, Y.; DUVALL, T. L.; ZHAO, J.; TITLE, A. M.; SCHRIJVER, C. J.; TARBELL, T. D.; TOMCZYK, S. The Helioseismic and Magnetic Imager (HMI) Investigation for the Solar Dynamics Observatory (SDO). **Solar Physics**, v. 275, p. 207–227, jan. 2012. 37

SCHRIJVER, C. J.; DEROSA, M. L.; METCALF, T.; BARNES, G.; LITES, B.; TARBELL, T.; MCTIERNAN, J.; VALORI, G.; WIEGELMANN, T.; WHEATLAND, M. S.; AMARI, T.; AULANIER, G.; DÉMOULIN, P.; FUHRMANN, M.; KUSANO, K.; RÉGNIER, S.; THALMANN, J. K. Nonlinear force-free field modeling of a solar active region around the time of a major flare and coronal mass ejection. **The Astrophysical Journal**, v. 675, p. 1637–1644, mar. 2008. 34

SCHRIJVER, C. J.; SISCOE, G. L.; BOGDAN, T. J.; REMPEL, M.; LONGCOPE, D. W.; FORBES, T. G.; MOLDWIN, M. B.; SMITH, C. W.; HANSTEEN, V. H.; VASYLIUNAS, V. M.; TOFFOLETTO, F. R.; FULLER-ROWELL, T.; BAGENAL, F. **Heliophysics: plasma physics of the local cosmos**. Cambridge, UK: Cambridge University Press, 2011. 43–44 p. Disponível em: <http://www.cambridge.org/us/academic/subjects/earth-and-environmental-science/atmospheric-science-and-meteorology/heliophysics-plasma-physics-local-cosmos>. 25, 27, 71

SCHRIJVER, C. J.; ZWAAN, C. **Solar and stellar magnetic activity**. [S.l.]: Cambridge University Press, 2000. (Cambridge Astrophysics). 2, 3

SILVA, L. A. D.; SATYAMURTY, P. Evolution of the lorenz energy cycle in the intertropical convergence zone in the south american sector of the atlantic ocean. **Journal of Climate**, v. 26, n. 10, p. 3466–3481, 2013. Disponível em: <https://doi.org/10.1175/JCLI-D-11-00426.1>. 73

SOLANKI, S. The magnetic structure of sunspots and starspots. **Astronomische Nachrichten**, WILEY-VCH Verlag, v. 323, n. 3-4, p. 165–177, 2002. ISSN 1521-3994. Disponível em:

<http://dx.doi.org/10.1002/1521-3994(200208)323:3/4<165::AID-ASNA165>3.0.CO;2-U>. 7

______. Sunspots: An overview. **The Astronomy and Astrophysics Review**, v. 11, n. 2, p. 153–286, 2003. ISSN 1432-0754. Disponível em: <http://dx.doi.org/10.1007/s00159-003-0018-4>. 7

______. Quantitative explanation of stokes v asymmetry in solar magnetic flux tubes. In: **Physics of magnetic flux ropes**. American Geophysical Union, 2013. p. 185–188. ISBN 9781118663868. Disponível em: <http://dx.doi.org/10.1029/GM058p0185>. 42

THALMANN, J. K.; WIEGELMANN, T. Evolution of the flaring active region NOAA 10540 as a sequence of nonlinear force-free field extrapolations. **Astronomy & Astrophysics**, v. 484, p. 495–502, jun. 2008. 34

TSUNETA, S.; ICHIMOTO, K.; KATSUKAWA, Y.; NAGATA, S.; OTSUBO, M.; SHIMIZU, T.; SUEMATSU, Y.; NAKAGIRI, M.; NOGUCHI, M.; TARBELL, T.; TITLE, A.; SHINE, R.; ROSENBERG, W.; HOFFMANN, C.; JURCEVICH, B.; KUSHNER, G.; LEVAY, M.; LITES, B.; ELMORE, D.; MATSUSHITA, T.; KAWAGUCHI, N.; SAITO, H.; MIKAMI, I.; HILL, L. D.; OWENS, J. K. The Solar Optical Telescope for the Hinode Mission: An Overview. **Solar Physics**, v. 249, p. 167–196, jun. 2008. 37

UITENBROEK, H. The accuracy of the center-of-gravity method for measuring velocity and magnetic field strength in the solar photosphere. **The Astrophysical Journal**, v. 592, n. 2, p. 1225, 2003. Disponível em: <http://stacks.iop.org/0004-637X/592/i=2/a=1225>. 41

WANG, H.; CHAE, V. Y. J.; YANG, G.; STEINEGGER, M.; GOODE, P. Inter-active region connection of sympathetic flaring on 2000 february 17. **The Astrophysical Journal**, v. 559, n. 2, p. 1171, 2001. Disponível em: <http://stacks.iop.org/0004-637X/559/i=2/a=1171>. 74

WARMUTH, A. Large-scale globally propagating coronal waves. **Living Reviews in Solar Physics**, v. 12, n. 1, p. 3, 2015. ISSN 1614-4961. Disponível em: <http://dx.doi.org/10.1007/lrsp-2015-3>. 71

WHEATLAND, M. S.; STURROCK, P. A.; ROUMELIOTIS, G. An optimization approach to reconstructing force-free fields. **The Astrophysical Journal**, v. 540, n. 2, p. 1150, 2000. Disponível em: <http://stacks.iop.org/0004-637X/540/i=2/a=1150>. 51, 91

WIEGELMANN, T.; SAKURAI, T. Solar Force-free Magnetic Fields. **Living Reviews in Solar Physics**, v. 9, p. 5, set. 2012. 25, 33

WIEGELMANN, T.; THALMANN, J. K.; SOLANKI, S. K. The magnetic field in the solar atmosphere. **The Astronomy & Astrophysics Review**, v. 22, p. 78, nov. 2014. 7, 9, 35, 49, 60

ZHAO, J.; KOSOVICHEV, A. G.; DUVALL JR., T. L. Investigation of Mass Flows beneath a Sunspot by Time-Distance Helioseismology. **The Astrophysical Journal**, v. 557, p. 384–388, ago. 2001. 4

APENDIX A - Computational tools

A.1 Tools for solar data analysis

This chapter will discuss what solar data analysis tools were directly relevant to produce the results featured in this work. The results were obtained using custom routines which, in some cases, had existing packages as building blocks.

A.1.1 Solarsoft (SSW-IDL)

The Solarsoft comprises a set of packages with relevant routines for solar data analysis. While Solarsoft is free for install and use, it requires an installation of Interactive Data Language (IDL).

Data obtained from the solar telescopes such as HMI and Hinode are usually processed using a solarsoft installation within IDL where existing routines can calibrate and plot results from the fits files depending on the data level.

Difficulties may arise since the routines are mostly made to operate with a higher level data and the methods used to process data by the observatories which provide the data are subject to changes. Lower level data are not available in the Joint Science Operations Center, which provide HMI data, and must be requested by email.

Some of the SSW/IDL packages that were used are the following: ONTOLOGY, SOT, AIA, HMI, PFSS, NLFFF and SDO. Subroutines were then developed to work along with those packages and process the data.

A.1.2 Magnetic field extrapolation

The magnetic field extrapolations were performed using the optimization_fff routine which is part of the Solarsoft NLFFF package. The code is based on an optimization approach proposed in Wheatland et al. (2000) where the functional L, Equation A.1, is minimized using an evolutionary process to ensure that the studied volume is considered to be free of forces.

$$L = \int_V B^{-2} \mid (\nabla \times B) \times B \mid^2 + \mid \nabla \cdot B \mid^2 dV \tag{A.1}$$

The optimization_fff algorithm can use as a initial condition a potential or LFF extrapolation that are calculated using HMI observables as input. An image of the HMI magnetogram of the AR NOAA 12443 is displayed in figure A.1. The HMI observables that were used have a temporal resolution of 12 minutes. NLFF approach was not used since the hardware capabilities and time available to produce the dissertation are not enough to produce such results.

Figure A.1 - AR NOAA 12443 magnetogram.

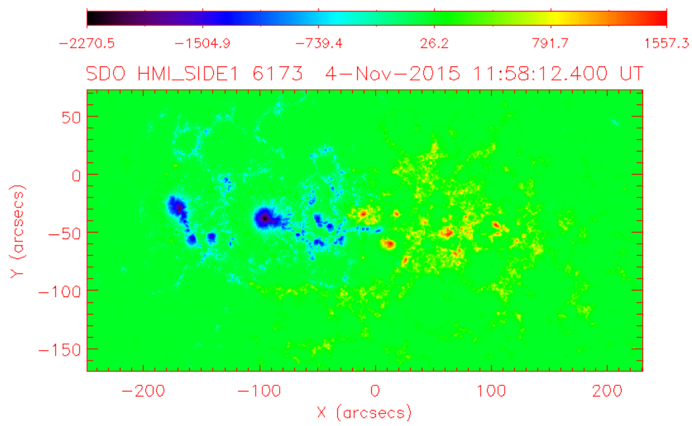

Colourised magnetogram of the AR NOAA 12443 produced with HMI data. This image was taken when the AR was close to the disk center (2015-11-04).

SOURCE: Author's own work.

The extrapolations were performed using the HMI Spaceweather HMI Active Region Patch (SHARP), that consists on cutouts of HMI magnetic products of an AR.

The used routine allows the user to set a value for alpha which is going to be used to calculate the initial conditions of the problem. The values for alpha represents the cosine of the torsion angle of the lines respective to the potential magnetic field. Therefore having zero as a value would result in a potential field extrapolation. Note that the value inserted will be treated as a constant over the space since a force-free approximation was used to extrapolate data.

PUBLICAÇÕES TÉCNICO-CIENTÍFICAS EDITADAS PELO INPE

Teses e Dissertações (TDI)

Teses e Dissertações apresentadas nos Cursos de Pós-Graduação do INPE.

Notas Técnico-Científicas (NTC)

Incluem resultados preliminares de pesquisa, descrição de equipamentos, descrição e ou documentação de programas de computador, descrição de sistemas e experimentos, apresentação de testes, dados, atlas, e documentação de projetos de engenharia.

Propostas e Relatórios de Projetos (PRP)

São propostas de projetos técnico-científicos e relatórios de acompanhamento de projetos, atividades e convênios.

Publicações Seriadas

São os seriados técnico-científicos: boletins, periódicos, anuários e anais de eventos (simpósios e congressos). Constam destas publicações o Internacional Standard Serial Number (ISSN), que é um código único e definitivo para identificação de títulos de seriados.

Pré-publicações (PRE)

Todos os artigos publicados em periódicos, anais e como capítulos de livros.

Manuais Técnicos (MAN)

São publicações de caráter técnico que incluem normas, procedimentos, instruções e orientações.

Relatórios de Pesquisa (RPQ)

Reportam resultados ou progressos de pesquisas tanto de natureza técnica quanto científica, cujo nível seja compatível com o de uma publicação em periódico nacional ou internacional.

Publicações Didáticas (PUD)

Incluem apostilas, notas de aula e manuais didáticos.

Programas de Computador (PDC)

São a seqüência de instruções ou códigos, expressos em uma linguagem de programação compilada ou interpretada, a ser executada por um computador para alcançar um determinado objetivo. Aceitam-se tanto programas fonte quanto os executáveis.